SEMICONDUCTOR-TO-METAL PHASE TRANSITIONS OF VANADIUM DIOXIDE (VO_2) THIN FILMS

A Dissertation

by

JIE JIAN

Submitted to the Office of Graduate and Professional Studies of
Texas A&M University
in partial fulfillment of the requirements for the degree of

DOCTOR OF PHILOSOPHY

Chair of Committee,	Haiyan Wang
Co-chair of Committee,	Jun Kameoka
Committee Members,	Pen Li
	Xinghang Zhang
Head of Department,	Miroslav M. Begovic

December 2016

Major Subject: Electrical Engineering

ABSTRACT

Among all the metal-oxide phase transition materials, vanadium dioxide (VO_2) has attracted extensive research interest benefiting to its outstanding semiconductor-to metal phase transition (SMT) properties with a transition temperature (T_c) close to room temperature. VO_2 is known to exhibit an ultrafast (within 0.1 ℃) and reversible phase transition from a semiconductor phase to a metallic phase at ~68 ℃. Because of this fascinating characteristic, VO_2 shows great potential in various devices including sensors, switches, thermo/electrochromics, thermal actuators, and memory devices. The semiconductor phase VO_2 has a monoclinic crystal structure. By the first-order SMT process, VO_2 transits to tetragonal crystal structure, which results in dramatic changes in its electrical and optical properties.

Compared with single crystalline VO_2, the properties of VO_2 thin films can be largely affected by many factors including defects density, strain, and the existence of the multivalent vanadium ions (V^{2+}, V^{3+}, V^{4+}, V^{5+}). It's quite challenging to synthesize high quality VO_2 thin films with sharp transition width, narrow thermal hysteresis, and large electrical and optical property change. In order to address these issues, the work in this thesis is focused on optimizing the SMT properties of VO_2 thin films and studying the defect effects in the SMT processes.

Firstly, highly textured VO_2 thin films have been achieved on amorphous glass substrates and compared with the ones grown on *c*-cut sapphire and Si (111) substrates, all by pulsed laser deposition. Excellent phase transition properties were observed for the

films on glass substrates and were correlated with the large grain size and low defects density of the films.

Based on the first work, VO_2 thin films with controlled grain sizes were deposited on amorphous glass substrates by pulsed laser deposition. The VO_2 films were found to exhibit a sharper SMT and larger transition amplitude with lower grain boundary (GB) density. The GBs were revealed to introduce disordered atomic structures and distorted crystal lattices in the films, which results in the drop of the film SMT properties.

To enable VO_2 thin films in practical devices, a tunable T_c of VO_2 is necessary to satisfy the working environments of different devices. To achieve the tunable T_c, VO_2 thin films with controlled thicknesses have been deposited on *c*-cut sapphire substrates with Al-doped ZnO (AZO) buffer layers by pulsed laser deposition. The T_c of the films was continuously tuned by the VO_2 thickness and the VO_2/AZO interface roughness, accompanied with no significant drop of other SMT properties. It shows that the T_c is correlated with the film strain, which increases with the decrease of film thickness or VO_2/AZO interface roughness.

Finally, the stability of the VO_2 thin film phase transition was characterized. The VO_2 film deposited on *c*-cut sapphire substrate has been founded to exhibit a T_c shifting and transition width broadening after tens of cycles of phase transition. *In situ* transmission electron microscopy (TEM) heating experiments revealed that the strain was accumulated around the domain boundaries during phase transitions, possibly because of the dimension changes of the crystals.

DEDICATION

This dissertation is dedicated to my wife, my parents, and my friends

ACKNOWLEDGMENTS

I would like to express my deepest appreciation to my advisor, Prof. Haiyan Wang. In the four years of Ph.D. study, she provides me a precious opportunity to study at Texas A&M University where group atmosphere is like a family. She guides me into the world of scientific research and helped me to build a strong ethic of working. Without her continuous guide and ongoing motivation, my research can never come this far. I was so lucky that I could study for my Ph.D. under her supervision for five years.

I would like to send my special appreciation to all my committee members, Dr. Jun Kameoka, Dr. Pen Li, and Dr. Xinghang Zhang for their valuable suggestions and guidance on my research. I really appreciate their time and effort in helping me on my research projects.

I also want to thank all my colleagues in the Functional Thin Film Group: Dr. Joon Hwan Lee, Dr. Chen-Fong Tsai, Dr. Aiping Chen, Dr. Li Chen, Dr. Yuanyuan Zhu, Dr. Michelle Myers, Dr. Qing Su, Dr. Fauzia Khatkatay, Dr. Liang Jiao, Dr. Wenrui Zhang, Dr. Clement Jacob, Jijie Huang, Leigang Li, Meng Fan, Han Wang, Zhimin Qi, Xingyao Gao, Bruce Zhang, Xing Sun and Xuejing Wang for making my life at Texas A&M University a great experience. Special appreciation goes to my friends and coworkers: Dr. Yue Liu, Dr. Kaiyuan Yu, Dr. Youxing Chen, Jin Li, Zhe Fan, Sichuang Xue and Qiang Li, for their companionship through my graduate school journey.

My research is supported by the National Science Foundation and the Office of Naval Research. I also want to thank Texas A&M University for providing wonderful

research environment and resources for me.

Last but not least, I would like to thank my beloved wife, Yue Min, and parents and parents-in-law for their constant support and encouragement throughout the past years.

TABLE OF CONTENTS

Page

LIST OF FIGURES

Page

LIST OF TABLEs

Page

CHAPTER I

INTRODUCTION

1.1 Overview

Over the past several decades, metal-oxide phase transition materials have attracted extensive research efforts owing to their dramatic physical property changes during phase transition processes [1-3]. Among all, vanadium dioxide (VO_2) is in particular interest because of its transition temperature (T_c) close to room temperature [4]. VO_2 single crystals exhibit an ultrafast (within 0.1 ℃) and reversible phase transition from a semiconductor phase to a metallic phase (SMT) at ~68 ℃ during heating process [5]. Through such a first-order phase transition [6], VO_2 transit from a tetragonal rutile phase to a monoclinic phase [7], accompanied with significant changes in the electrical [8-10] and optical properties [11-13]. Owing to the fascinating characteristics, VO_2 shows great potential in various devices including gas sensors [14], electrical switches [15], thermochromic smart windows [16], thermal actuators [17] and memory devices [18], etc.

The VO_2 single crystals were reported to exhibit an electrical resistivity transition of 4-5 orders of magnitude during SMT process [19], accompanied with the optical transmission change of 40-50% in the near infrared and terahertz wavelength region [20]. However, bulk single crystal VO_2 has poor ductility which could lead to failure during multi-cycle phase transitions [21]. Besides, the bulk VO_2 can’t fit the size requirements of many devices. Therefore, during the past two decades, great efforts have been focused on improving the quality and performance of nanostructured VO_2. Especially, VO_2 thin

films have attracted particular interest because of the 2-dimentional geometry, the compatibility with current device manufacture and the capability to stand distortions. Compared with single crystalline VO_2, the properties of VO_2 thin films can be largely affected by many factors including defects density [22], strain [23], and the existence of the multivalent vanadium ions (V^{2+}, V^{3+}, V^{4+}, V^{5+}) [24].

In order to enhance the film quality and performance, VO_2 thin films have been synthesized by various growth methods. The commonly used methods include chemical vapor deposition (CVD) [25], sol-gel process [4], pulsed laser deposition (PLD) [26], reactive sputtering [10], electron beam evaporation [27], etc. Various substrates have been applied for VO_2 growth with different purposes. For instance, *c*-cut sapphire substrates were commonly used to grow epitaxial VO_2 thin films [28]. Si substrates were applied to achieve the compatibility with current electrical devices [29]. Glass substrates were usually used for optical applications owing to the high transparency [30]. Furthermore, in order to tune the T_c of VO_2 thin films, different doping elements have been introduced to shift the fermi level of the semiconductor VO_2. VO_2 thin films with different doping elements, including Mg, Mo, W, Ti and Cr, have been achieved and the T_c of the films has been tuned from less than 200 K to more than 350 K [31-36]. In addition, the defects in the VO_2 thin films have been studied and correlated with the SMT properties. A model has been previously proposed for the microstructure-property correlations of VO_2 based on defect density and interfacial energies [37]. In general, it suggested the better SMT properties with the higher epitaxial quality of the film, which agreed well with some of the experimental results [22].

Recently, the *in situ* transmission electron microscopy (TEM) techniques, which conduct physical or chemical property measurements of the sample with real time monitoring in the TEM column, provide great opportunities to study the mechanisms of VO_2 phase transition. In particular, the *in situ* TEM heating technique has been applied to study the defect effects and microstructure evolution during SMT process of VO_2 [38, 39]. *In situ* TEM mechanical testing has been conducted on VO_2 nanowires and revealed the strain induced phase transition as well as the different mechanical properties of different VO_2 phases [40, 41]. Therefore, the *in situ* TEM techniques have great potential on future VO_2 fundamental studies.

This chapter reviews the background of the VO_2 studies, and summarizes the previous works for VO_2 property enhancements and applications. It starts with a brief introduction of the VO_2 crystal and energy band structures. Then the VO_2 SMT properties and the correlated fundamental mechanisms are described in section 1.2.3 and 1.2.4. The synthesis methods of nanostructured VO_2 and the representative applications are introduced in section 1.2.5 and 1.2.6. The critical issues and previous works on VO_2 thin film growth and characterizations are summarized in section 1.3. Section 1.4 reviews the recent *in situ* TEM studies on VO_2. Finally, the challenges in current studies on VO_2 are proposed in section 1.5.

1.2 A review of vanadium dioxide (VO_2)

1.2.1 Vanadium oxide compounds

Vanadium has various oxidation states (+2, +3, +4, and +5) and thus produces

more than ten different stable vanadium oxide phases, including single valent oxides such as VO, V_2O_3, VO_2, V_2O_5,and mixed valent oxides such as V_6O_{13}, V_8O_{15} [42]. Figure 1.1 shows the vanadium-oxygen system phase diagram [43, 44]. Most of the vanadium oxide compounds show reversible semiconductor-to-metal phase transition (SMT) accompanied with significant changes of the electrical and optical properties [4, 45-47]. Because of these fascinating characteristics, they have been receiving significant research attentions and show great potential in various devices. For example, VO_2 can be used in various devices including gas sensors [14], switches [15], thermo/electrochromics [16], Mott transistors [48], and thermal actuators [17], while the V_2O_3 films of appropriate thickness have potential application as solar control products [49].

The thermally driven SMT occurs at a critical temperature (T_c) based on the electrical resistivity (ρ) measurement. The T_c for different vanadium oxides varies from as low as -200 ℃ (~70 K) to as high as 177 ℃ (450 K) as listed in table 1.1 [4, 45, 50]. Among all, the VO_2 is one of the particular interests owing to its reversible, first-order SMT at a T_c close to room temperature (RT).

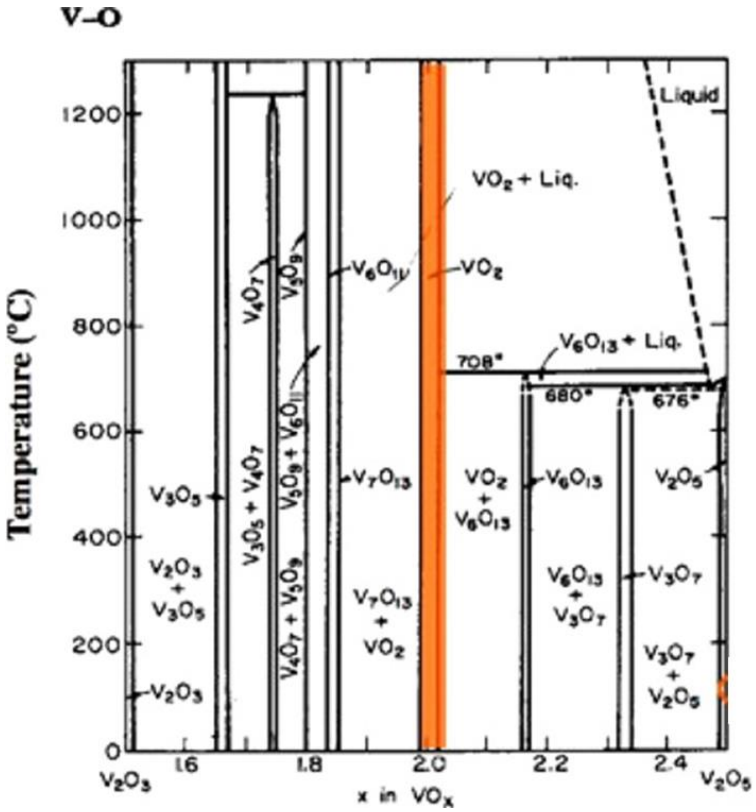

Figure 1.1 Phase diagram of the vanadium-oxygen system. Reprinted with permission from Institute of Physics [43, 44].

Table 1.1 The metal-insulator transition of vanadium oxides [4, 45, 50]

Oxides	T_c (℃/K)	Transition amplitude (orders of conductivity jump)
VO	Metal	-
V_2O_3	-123/150	10
V_3O_5	177/450	2
V_4O_7	-33/240	3
V_5O_9	-143/130	6

Table 1.1 continued

Oxides	T_c (℃/K)	Transition amplitude (orders of conductivity jump)
V_6O_{11}	-103/170	4
V_7O_{13}	Metal	-
V_8O_{15}	-203/70	1
VO_2	67/340	5
V_6O_{13}	-123/150	6
V_2O_5	Insulator	-

1.2.2 VO_2 crystal and band structures

Crystal structures

Vanadium dioxide (VO_2) is known to have several polymorphs, which include VO_2(A), VO_2(B), VO_2(M1) and VO_2(R) [51]. With the same chemical stoichiometry, their crystalline and electronic structures are completely different and highly complex, exhibiting many interesting electrical, optical and chemical properties. At the temperature higher than T_c, VO_2 forms as a stable metallic tetragonal phase (rutile phase). This structure is based on a simple tetragonal lattice with space group P42/mnm [5, 52]. The lattice constants of rutile VO_2 are a=4.554 Å and c=2.8557 Å [8]. The vanadium atoms occupy the Wyckoff positions (2a): (0, 0, 0), ($\frac{1}{2}$, $\frac{1}{2}$, $\frac{1}{2}$), while the oxygen atoms are located at the positions (4f): $\pm(u, u, 0)$, $\pm(\frac{1}{2}+u, \frac{1}{2}-u, \frac{1}{2})$. Figure 1.2(a)

displays the rutile VO_2 structure [7].

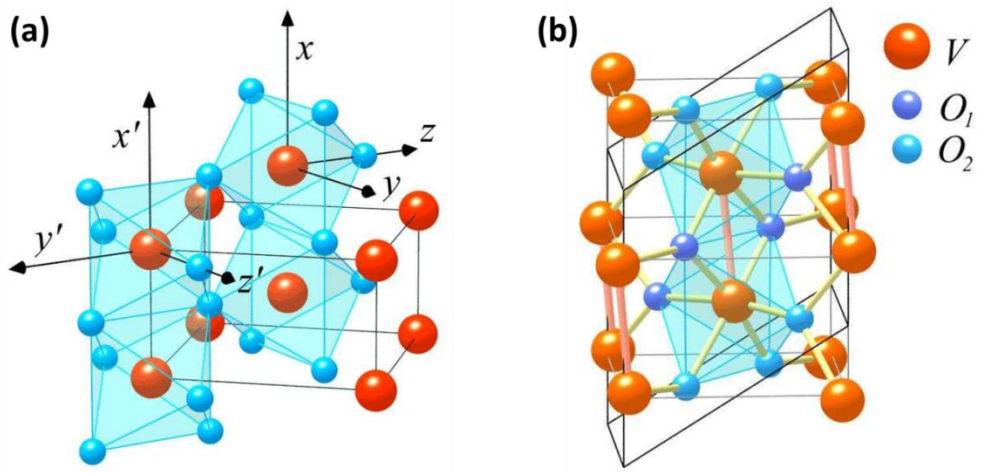

Figure 1.2 Atomic structures of (a) R phase and (b) M1 phase VO_2. Reprinted with permission from Annalen der Physik [7].

While the temperature drops below T_c, the regular V-V separation (*c*-axis) of 0.286 nm in the tetragonal structure transforms to alternate V-V separations of 0.266 and 0.313 nm, leading to a doubling up of the unit cell [7]. A remarkable feature of the VO_2 M1 monoclinic structure is the presence of V-V pairs along its *a*-axis. The VO_2 monoclinic structure belongs to the space group $P2_1/c$ [37]. The lattice constants of VO_2 monoclinic unit cell were reported as a=5.7517 Å, b=4.5378 Å, c=5.3825 Å, and β=122.646° [53]. The monoclinic VO_2 crystal structure is shown in Figure 1.2 (b). The

metal atoms and the two different types of oxygen atoms occupy the Wyckoff position (4e): $\pm(x, y, z)$, $\pm(x, \frac{1}{2}-y, \frac{1}{2}+z,)$ [54, 55]. The crystallographic relationship between the R and M1 phases is approximately $a_{M1} = 2c_r$ and $b_{M1} = a_r$ [5, 8, 56].

The A and B phases of VO_2 are metastable tetragonal and monoclinic phases. They can be achieved by introducing certain internal stresses in the VO_2 lattice and will transit back to stable tetragonal (R) and monoclinic (M1) phases when the stresses are released [55]. The atomic structures of VO_2 in A and B phases are shown in Figure 1.3. Table 1.2 summarizes the crystal structures and lattice constants of different VO_2 polymorphs [51].

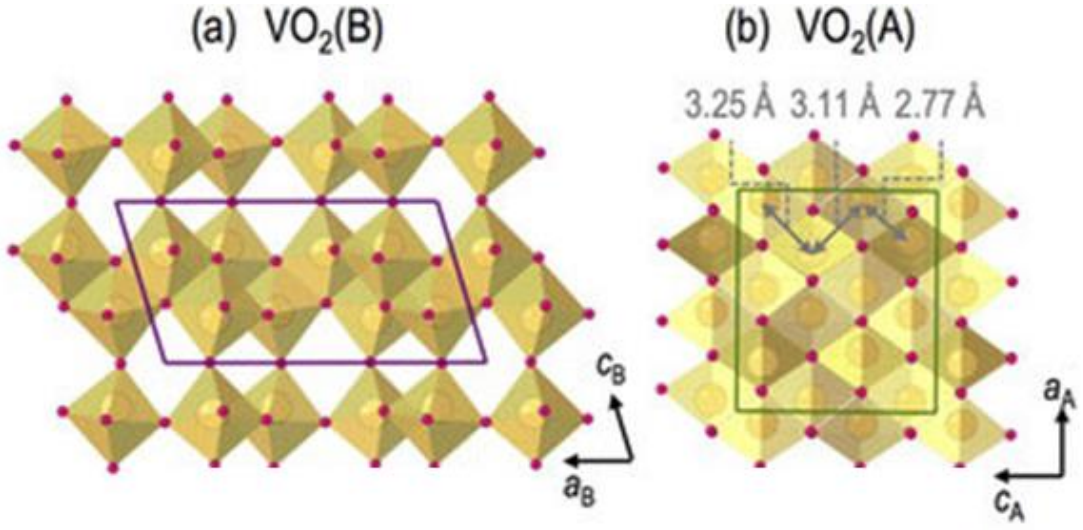

Figure 1.3 Atomic structures of (a) B phase and (b) A phase VO_2. Reprinted with permission from Scientific Reports [51].

Table 1.2 Crystal structures and lattice constants of VO_2 in different phases [51]

VO_2 polymorphs	Crystal structure (space group)	Lattice constants in bulk			
		a (Å)	*b* (Å)	*c* (Å)	*β* (Å)
VO_2 (M1)	Monoclinic ($P2_1/c(14)$)	5.38	4.52	5.74	122.6
VO_2 (R)	Tetragonal ($P4_2/mnm(136)$)	4.55	4.55	2.86	
VO_2 (A)	Tetragonal ($P4_2/ncm(138)$)	8.43	8.43	7.68	
VO_2 (B)	Monoclinic (C2/m(12))	12.03	3.69	6.42	106.6

Band structures

The Goodenough model is used to describe the band structure of the M1 and R phase VO_2 [57]. The vanadium atoms in VO_2 have $3d^3s^2$ electron orbits. Each vanadium atom has 4 electrons in the valence band, leaving one electron in the conduction band. Based on the $3d^14s^04p^0$ energy levels for cation V^{4+} and the $2s^22p^6$ energy levels for anion O^{2-}, the energy band structure of tetragonal VO_2 is derived in Figure 1.4(a) [5]. The electrostatic Madelung energy (E_M) for the effective ionic charges is able to stabilize the O^{2-} :2p orbitals relative to the V^{4+} :3d orbitals. If considering the ionization energy of cations and electron affinity of the anions, the stabilization energy is reduced to E_M-E_I. Thus the oxygen 2p levels are far below the vanadium 3d states. The V^{4+} ion octahedral crystal field splits the $3d^1$ state into a high energy twofold-degenerate state of e_g ($d_{3z^2-r^2}$, d_{xy}), and a low energy threefold-degenerate state of t_{2g} ($d_{x^2-y^2}$, d_{xz}, d_{yz}) [7]. The two e_g orbitals are further split into two d_σ orbitals. The three t_{2g} orbitals are split into a $d_\parallel$

orbital formed by the σ bonding along c_r direction, and two d_π orbitals formed by the V_d—O_p bonding. The antibonding doublets of V-V and V_d-O_p lead to the bands of σ^* and π^*. The separation between σ^* and π^* bands is described by itinerant-electron model. For the case of tetragonal VO_2, the c_r/a_r ratio is about 0.627, suggesting an overlap of $3d_\sigma$ σ^* bands and $3d_\pi$ π^* bands, leading to the isotropic resistivity of the material [58, 59].

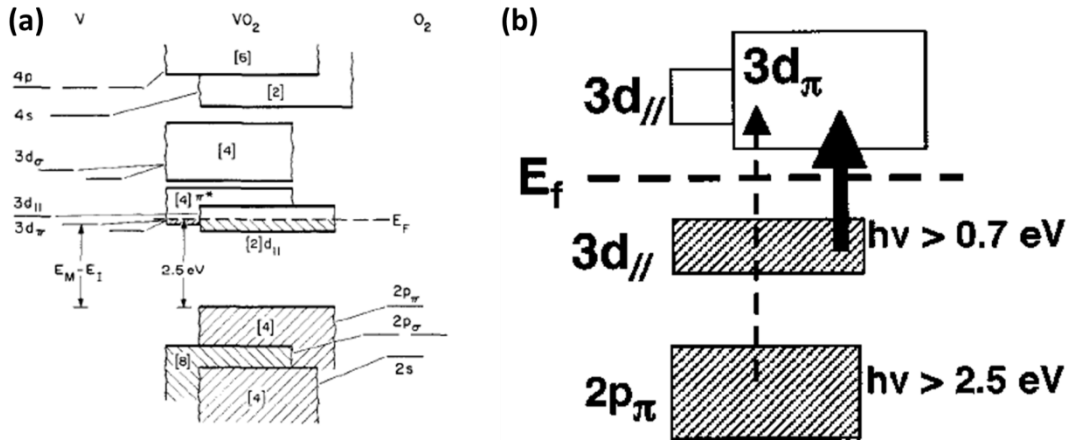

Figure 1.4 The electron band structures of VO_2. (a) R phase [5] and (b) M1 phase. Reprinted with permission from Elsevier and American Physical Society [5, 62].

The phase transition of VO_2 from R phase to M1 phase leads to the distortion along the c_r direction. The deformation of the octahedral oxygen crystal field results in the destabilization of the hybridized d_π band and thus raises it above the Fermi level [60]. Besides, the crystallographic distortion is accompanied with a doubling of the c_r-axis to form the a_{M1}-axis, which split the half filled $d_\parallel$ band into two separated bands [61]. The lower $d_\parallel$ band is completely filled while the upper $d_\parallel$ band is empty. As shown in Figure 1.4(b) [62], the energy gap between the lower $d_\parallel$ band and the d_π band is about 0.7 eV, leading to the semiconductor properties of M1 phase VO_2. As the d_π band is partially filled with electrons at RT, the M1 phase VO_2 is an n-type semiconductor [63].

1.2.3 VO_2 Phase transition mechanisms: Mott model vs. Peierls model

Peierls model

It has been decades to study the origin of VO_2 phase transition. However, it is still a big challenge to identify the true mechanisms. Several models have been applied to explain the SMT of VO_2. An earlier attempt was approached by using a non-interacting electron model to understand the origin of band gaps in semiconductors.

In 1930s, Rudolf Peierls stated that a one-dimensional equally spaced chain with one electron per ion is unstable [6, 64]. In order to lower the energy, the ions would prefer to rearrange and make a distorted lattice, as shown in Figure 1.5. The distortion will introduce a smaller band gap of the material. When the energy saved from the band gap is larger than the elastic energy generated by lattice distortion, the rearrangement

will be initiated.

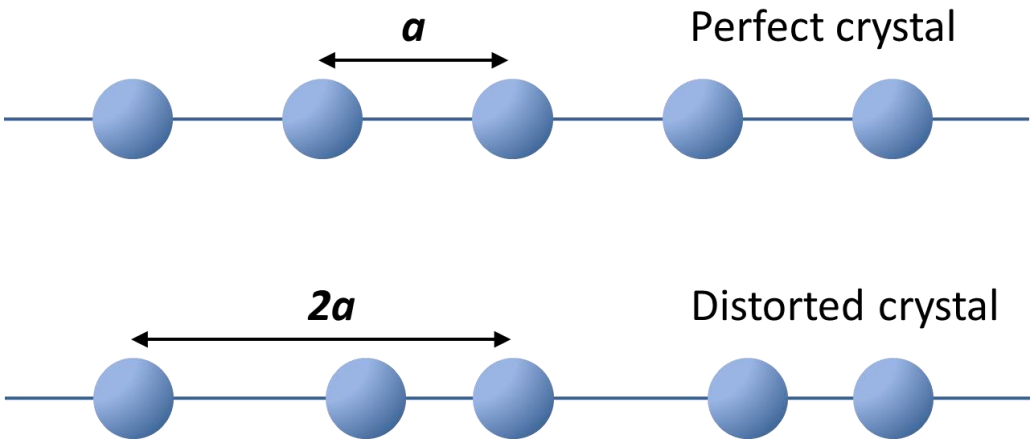

Figure 1.5 Peierls model: Distortion of the periodic lattice in 1-D crystal

A model of the potential for an electron in a 1-D chain can be used to describe the energy states of the distorted lattice,

$$H = H^0 + V = \frac{p^2}{2m} + V(x) \tag{1.1}$$

where H^0 is the Hamiltonian of non-interacting electrons in the 1-D chain, V is a periodic potential [65], i.e. $V(x + a) = V(x)$. Based on this theory, the periodic potential in the non-distorted lattice leads to band gaps at $k = \pm\frac{\pi}{a}$. For atoms with single valent electron, such as the vanadium atom in VO_2 with $3d^1$ electron, the bands are half filled

and therefore the crystal would be metallic. Through the Peierls transition, the potential period changes from a to 2a, resulting in the band gaps at$k = \pm\frac{\pi}{2a}$. The electrons could fill all the states and make the material semiconductor.

However, when the Peierls model was applied on VO_2, it failed to explain many behaviors of VO_2 phase transition. Therefore new models have been introduced to further understand the SMT behavior of VO_2.

Mott model

The Mott model is the most commonly accepted model for the mechanisms of VO_2 phase transition. It is widely used to describe the materials which should conduct electricity under conventional band theories, but are insulators when measured [66]. These materials, such as the M1 phase VO_2 [9], are called Mott insulating materials (or Mott insulators). The electron-electron interaction, which is ignored in the Bloch theory, plays an important role in the Mott model. It suggests that the low conductivity of the Mott insulators is caused by the strong interactions between electrons, where the Coulomb repulsion in between prevents them from conducting [67].

In 1937, Jan Hendrik de Boer and Evert Johannes Willem Verwey first demonstrated that a class of semiconductors with incompletely filled 3*d* bands has a relatively narrow energy bandgap but is lack of conductivity [68]. Nevill Mott and Rudolf Peierls then predicted that this phenomenon can be explained by the interactions between electrons [69]. At a low temperature, the electrostatic interaction between the electrons prevents them from moving, and therefore the majority of the electrons are in

their proper places in the ions. The minorities which overcame the potential barrier find that all the other atoms were occupied. Thus in order to get through the lattice, they have to spend a long time in ions already occupied by other electrons.

A physical model of Mott insulators was firstly proposed for NiO in 1949 [70]. Then the Hubbard model, named after John Hubbard, was proposed to describe the interacting particles in a lattice [71]. The Hubbard model was successfully used to explain and predict Mott insulators. It is based on the tight-binding approximation from solid state physics. In the tight-binding approximation, electrons are considered to occupy the standard orbitals of their constituent atoms, and then tunneling between atoms during conduction. Based on this theory, the movement of an excited electron in a lattice is a competition between the Coulomb potential (U) of electrons and the tight-binding (t) between electrons and each neighboring atom. Therefore, the total energy barrier of the electron conduction in a Mott insulating material can be presented as:

$$E = U - 2zt \tag{1.2}$$

where z is the number of nearest-neighbor atoms. In general, Mott insulating property occurs when the repulsive Coulomb potential U is large enough to create an obvious energy barrier in the lattice [72].

The Mott insulators can experience a Mott transition process with the increase of electron energy. By certain excitations, the induced energy will be high enough to overcome the electrostatic interaction between electrons and therefore allow a significant fraction of electrons to escape their sites [73].

Based on the Mott model, the electrons in the M1 phase VO_2 are localized on the V-V pairs by Coulomb repulsion. This will lift up the upper $d_{\parallel}$ band and leave a ~2.0 eV gap from the lower $d_{\parallel}$ band [74]. When the temperature increases to higher than T_c, the thermal energy allows electrons to overcome the 2.0 eV band gap and fill in the upper $d_{\parallel}$ band, which results in the transition of VO_2 to the metallic phase.

1.2.4 Semiconductor-to-metal transition (SMT) of VO_2

VO_2 single crystals exhibit an ultrafast (within 0.1 ℃) and reversible phase transition from the semiconductor phase to metallic phase (SMT) at ~68 ℃ during heating process [5]. Through such a first-order phase transition [6], VO_2 gets dramatic changes in its electrical [8-10] and optical [11-13] properties. Because of these unique characteristics, VO_2 have attracted considerable interest during the past five decades [75, 76]. Figure 1.6 shows the typical electrical resistivity [19] and optical [20] transmission changes of VO_2 along with the phase transition processes. It is shown that the resistivity switching can be as large as 10^4 to 10^5 times in bulk VO_2. In addition, the R phase VO_2 shows a much higher terahertz (THz) transmission compared to the M1 phase.

The phase transition of VO_2 can be triggered in many different ways. Besides of temperature switching, stress/strain, electrical field and photoexcitation could also lead to VO_2 phase transitions. Figure 1.7 shows the strain-temperature phase diagram of VO_2 [77]. The diagram indicates that the T_c of VO_2 is strongly dependent on the strain/stress. The T_c gradually decreases with the increase of compressive strain/stress along c_r-axis (a_m-axis). The compressive strain could even lead to a direct phase transition from M1

phase into R phase. On the other hand, the tensile strain along c_r-axis causes an increase of the T_c. Besides, it introduces an intermediate M2 phase of VO_2. The formation temperature of M2 phase decreases by increasing tensile strain. Therefore, the tensile strain leads to the broadening of the transition from M1 phase to R phase.

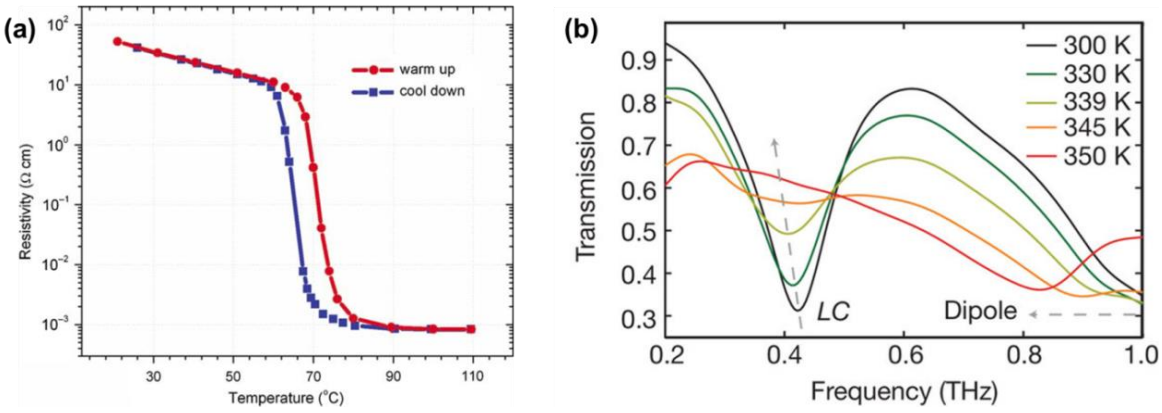

Figure 1.6 Electrical resistivity [19] and optical transmission [20] changes of VO_2 during phase transition processes. Reprinted with permission from Nature [20].

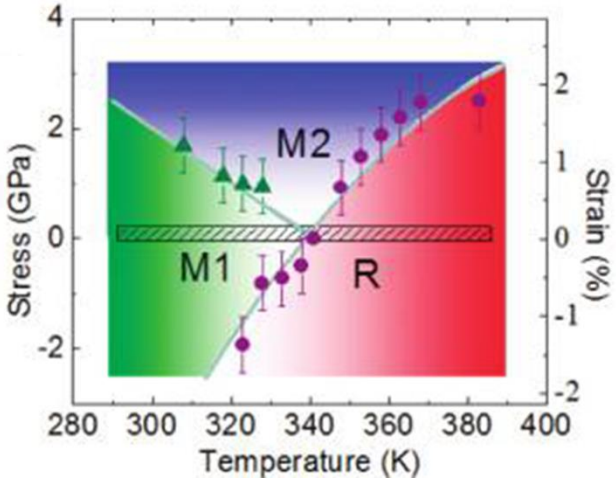

Figure 1.7 The uniaxial stress (along c_r-axis)-temperature phase diagram of VO_2. Reprinted with permission from American Chemical Society [77].

Figure 1.8(a) shows the electrical field triggering of VO_2 phase transition [78]. The jump of current density at ~22 V indicates a transition to metallic phase. Based on the band structures, the SMT of VO_2 strongly depends on the hole density of the semiconductor phase [48]. The electrical field actually results in a doping of the hole concentration in semiconductor VO_2, and therefore triggers the phase transition. The critical electrical field for VO_2 phase transition is typically ~ 10^6 V/m [79].

Figure 1.8(b) shows the VO_2 phase transition induced by photoexcitation [33]. The transition is triggered by increasing the power of incident beam. When the photon energy is higher than the band gap of VO_2, the increase of pump beam power could induce a photo-excitation of electrons from the lower $d_{\|}$ to the upper $d_{\|}$. The creation of electron-hole pairs makes the two split $d_{\|}$ bands form two overlapped and half filled

$d_{\parallel}$ bands, which leads the VO_2 to transit to the rutile phase [57, 62]. The photoexcitation response of VO_2 is ultrafast, usually less than 1 ns [80].

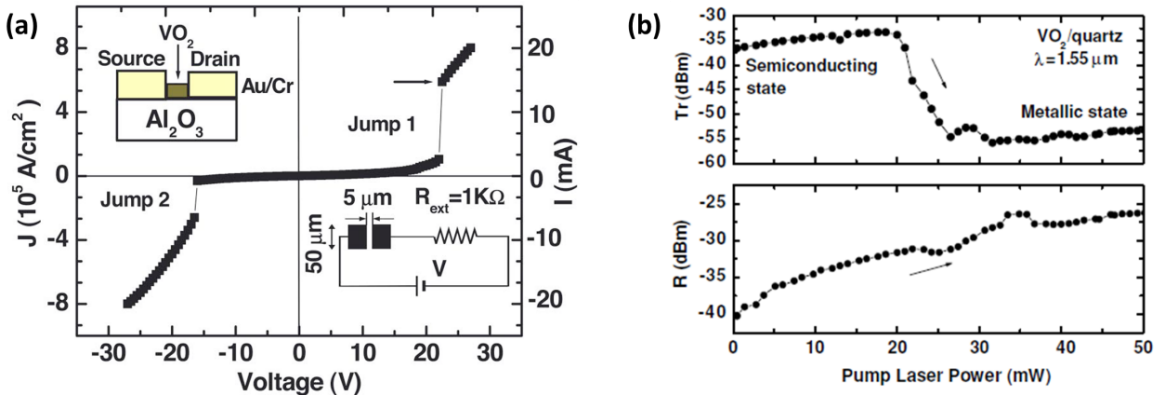

Figure 1.8 (a) Electrical field and (b) photoexcitation triggering of VO_2 phase transition. Reprinted with permission from American Institute of Physics and Institute of Physics [33, 78].

Benefit to the fascinating properties, VO_2 has great potential in various device applications. In order to match the requirements of different devices, nanostructured VO_2 with different geometries is desired. Despite of the excellent SMT properties of single crystalline bulk VO_2, it is quite challenging to synthesize high quality nanostructured VO_2 with outstanding performance. The existence of multivalent vanadium ions (V^{2+}, V^{3+}, V^{4+}, V^{5+}) could lead to the formation of other VO_x phases in the nanostructured VO_2 and result in the drop of overall properties [24]. Besides, the strains and defects in VO_2

could also influence its properties [22, 23, 81]. Therefore, great efforts have been focused on synthesizing high quality VO_2 thin films, nanowires, nanoparticles and other designed nanostructures and enhancing their properties.

Synthesis of VO_2 thin films

Many of the current technological devices, such as gas sensors [82], optical switches [83], smart window [84] and microbolometer [85], are based on thin films because of the 2-dimentional geometry, the compatibility and the capability to stand distortions. However, because of the lack of advanced synthesis techniques, there was a big delay of the study of VO_2 thin films since it was first explored [45]. One of the earliest VO_2 thin film growth was achieved by metal-organic chemical vapor deposition (MOCVD) [86]. Ryabova *et al.* used N_2 gas to carry the vapors of vanadium oxychrolide ($VOCl_3$) and then hydrolyzed on the inner surface of the crucible. Since 1990s, with the development of new techniques, the growth and SMT properties of VO_2 thin films have been explored by various deposition methods including chemical vapor deposition (CVD) [25], sol-gel process [4], pulsed laser deposition (PLD) [26, 87], reactive sputtering [10, 88-90], electron beam evaporation [27, 91, 92], etc.

Various vanadium-based precursors have been used for CVD growth of VO_2. Kim *et al.* achieved epitaxial VO_2 thin films on TiO_2 buffered sapphire substrates using vanadium triethoxide oxide [$VO(OC_2H_5)_3$] as precursor [93]. Sahana *et al.* used the vanadyl acetylacetonate [$VO(acac)_2$] to synthesize polycrystalline VO_2 on glass substrates [94]. Solution-based methods are more commonly used to synthesize VO_2

films for optical applications [36]. This kind of methods usually consists of a spin coating and a subsequent annealing process under low pressure. The vanadyl triisopropoxide [$VO(OC_3H_7)_3$] is commonly used as the starting material for both epitaxial and polycrystalline VO_2 growth [95]. Then the post annealing at oxygen deficient environment will evaporate the carbon and hydrogen, and leave the VO_2 thin films on the substrates. The chemical vapor or solution based deposition methods are low cost and highly efficient. However, it is quite challenging to control the defects density and get high quality VO_2 thin films. Besides, the adhesion between VO_2 and the substrates are usually not strong.

In contrast, many of the physical vapor deposition (PVD) techniques undergo non-equilibrium processes, which provide more kinetic energies to the ad-atoms. These methods are more commonly used to synthesize high quality epitaxial VO_2 thin films. Reactive sputtering growth of VO_2 thin films was firstly reported by Fuls *et al.* in 1967 [96]. Some novel sputtering methods, such as plasma-assisted sputtering [97] and magnetron sputter-ion plating physical vapor deposition [98], could achieve better quality VO_2 films. Recently, PLD is one of the most popular techniques for VO_2 thin film synthesis. The first PLD growth of VO_2 thin films was reported by Singh *et al.* in 1993 [26]. A KrF pulsed excimer laser (248 nm) was used to ablate a metallic vanadium target in vacuum chamber with Ar and O_2 (10:1) atmosphere of 100-200 mTorr, and a substrate temperature of about ~500 ℃. PLD technique has been used to deposit VO_2 thin films on different substrates, including sapphire [28], silicon [99], quartz [100], glass [101], etc.

Synthesis of VO_2 nanowires

The one-dimensional VO_2 nanowires show great potential in the applications of thermal actuators [17] and memory devices [18] and thus attract extensive research interests. However, the synthesis of high quality VO_2 nanowires is achieved in the recent decade. In 2004, Wu *et al.* reported the synthesis of VO_2 nanowires by the reaction of ammonium metavanadate (NH_4VO_3) and distilled water on stainless still and a subsequent drying process [102]. The fabricated VO_2 nanowires showed a (001) growth orientation. However, they didn't exhibit good SMT performances.

In recent, the vapor transport method is one of the most commonly used techniques to fabricate VO_2 nanowires. In this method, the bulk VO_2 powders were usually placed in a quartz boat in the center of a tube furnace. With thermal evaporation, the VO_2 was either directly deposited on the substrates above the quartz boat or carried by Ar gas to deposit on the substrates downstream from the boat [14, 103, 104]. The cross-section the VO_2 nanowires are usually in rectangular shape. The width of nanowires can be controlled from tens of nanometers to micron range by varying the temperature.

Because of the 1D geometry of VO_2 nanowires, they are convenient to be bent and distorted. Therefore, many mechanical tests have been conducted on VO_2 nanowires to study the strain effects on VO_2 phase transition. Wu *et al.* reported that the semiconductor and metallic phase domains could be simultaneously formed in a single VO_2 nanowire because of the internal strain distribution [105]. The VO_2 nanowires fabricated by Cao *et al.* showed a core-shell structure, i.e. inside semiconductor phase

covered by outside metallic phase, resulting from large surface stress [106]. Furthermore, the bending experiments showed the formation of alternate semiconductor-metallic phases in the curved area of VO_2 nanowires [77]. Besides, Guo et al. reported a tensile test induced M1-M2 phase transition of VO_2 nanowires [40].

Synthesis of VO_2 nanoparticles

The nanoparticle is a 0-D nanostructure. VO_2 nanoparticles are widely used to study the size effects on VO_2 phase transition [107]. Because of the 0-D geometry, VO_2 nanoparticles can be fabricated into periodic array structures, which show potential applications as photonic crystals [108], biochemical sensors [109], near-field electromagnetic waveguides [110], etc.

The VO_2 nanoparticles could be fabricated either on the surface of a substrate [23] or embedded in the substrate (matrix) [111]. The VO_2 nanoparticles can be directly synthesized on the substrate surface through the Volmer-Weber mode (island growth mode) growth, which isolated VO_2 nucleus will be formed at the early stage of depositions. Suh et al. reported the growth VO_2 nanoparticles on n-type Si substrates by PLD and a following thermal oxidation process [23]. The VO_2 particle size can be controlled by the deposition time. VO_2 nanoparticles in the matrix can be synthesized by direct implantations of vanadium and oxygen ions in the substrates. Lopez *et al.* reported that the V and O ions implanted in SiO_2 could form (011) oriented VO_2 nanoparticles by post-annealing [112]. The particle size can be controlled by annealing time and temperature. The periodic VO_2 nanoparticle arrays were usually fabricated on

lithography treated substrates, where the ion/electron beam lithography can precisely control the sizes and positions of the subsequently deposited VO_2 [113].

The VO_2 nanoparticles were reported to have strong size effects on the SMT properties [114]. With the decrease of particle size, VO_2 requires less phase transition energy (lower T_c) [113] but shows an increase of thermal hysteresis [112]. More point defects will be induced in the VO_2 nanoparticles with smaller size, which leads to a broadening of the VO_2 phase transition [115]. Besides, it was reported that the VO_2 nanoparticle arrays showed resonance effects in optical scattering spectrum [111]. The resonant peak position was reported to be dependent on particle sizes and positions, and shifted during phase transition.

1.2.6 Applications of VO_2

VO_2 is defined as one of the smart materials, which show intrinsic property responses to temperature changes, electric field and/or pressure variations, photoexcitation, etc. This class of materials generally has capabilities including sensing, switching, thermo/electrochromics and actuating. The SMT process for VO_2 occurs closer to room temperature than any of the commonly-known compounds and is accompanied with large changes in electrical resistivity and optical transmittance. Moreover, nanostructured VO_2 including thin films, nanowires and nanoparticles have more spatial ratio compared to bulk VO_2 and tend to survive the stress generated during repeated cycles of phase transition. Therefore they are suitable for many device applications.

Gas sensors

For the gas sensors, there are two major factors which define their performances: the receptor and transduction functions. The receptor function defines the interaction between the analyte molecules and the surface of the sensing material and therefore determines the sensor rate, selectivity, and reversibility. The transduction function defines the conversion of the interaction into the output signal [14]. In 1962, Seiyama *et al.* revealed that the electrical resistivity of ZnO could be dramatically changed by the presence of reactive gases in the environment [116]. Since then, tremendous works have been reported on the applications of metal-oxides semiconductors as gas sensors benefit to their small dimensions, low costs, and high compatibility with processing techniques [117]. In general, these gas sensors are in the size of nanometers and are based on the charge transfer mechanism between a nano-surface and an analyte molecule [118-120]. The charge transfer is followed by the formation of charge-induced depletion/accumulation layer in the nanostructures. However, the sensitivity of these kinds of nano-sensors is generally low beyond the class of strong redox molecules and usually requires elevated temperatures to have reasonable reaction rate [14, 121-123].

In 2009, Strelcov et al demonstrated a novel transduction principle in gas sensors based on the sharp temperature driven phase transition in VO_2 single crystal nanowires [14]. The concept is to fabricate single VO_2 nanowire with the T_c close to the environmental temperature. As the system pressure is influenced by the gas elements in the environments, the change of gas contents will lead to a change of external stress on the VO_2 nanowire, leading to a variation of the transition temperature. When the T_c of

the nanowire changes through the environmental temperature, the nanowire will experience a phase transition process, resulting in dramatic changes of the electrical resistivity. And thus the object of gas sensing is realized.

Baik *et al.* then reported exceptionally sensitive hydrogen sensors produced using Pd-nanoparticle-decorated single VO_2 nanowires [124]. The VO_2 nanowires were fabricated through the vapor transport method. After putting between two Au contacts, the VO_2 nanowire was further coated with a ~0.6 nm layer of Pd by electron beam evaporation. The Pd layer was then self-aggregated into nanoparticles, as shown in Figure 1.9 (a) and (b). The sensing process is realized by the absorption of H_2 in Pd particles, which changes the surface strain status of the VO_2 nanowires and leads to the lower down of T_c by over 10 ℃. As shown in Figure 1.9 (c), the sensor is operational at 50 ℃ and is reasonably sensitive to the H_2 gas flow as low as 5 sccm. More VO_2 based gas sensors are expected in the future researches with high sensitivity of different kinds of elements.

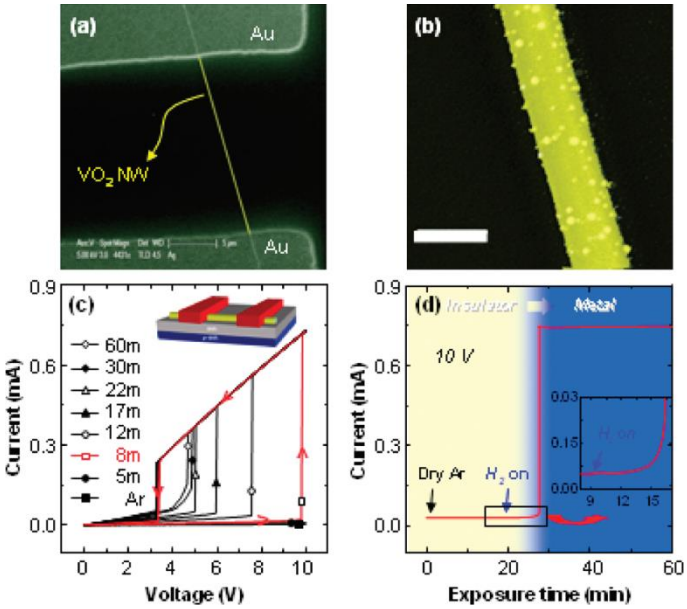

Figure 1.9 (a) Scanning electron microscopy (SEM) image of an individual VO_2 nanowire with appropriate Au contacts. (b) SEM image of a Pd-decorated VO_2 nanowire (scale bar, 200 nm). (c) I-V curves obtained at 50 ℃ for the nanowire after various exposure times to hydrogen gas (5 sccm). (d) The change in current for the nanowire biased at 10 V as a function of time of exposure to hydrogen gas. Reprinted with permission from Americal Chemical Society [124].

Electrical switches

The electrical switch is a direct use of the electrical property transition of VO_2 during SMT process. In practical applications, electrical field or optical driven resistance switching is more favorable owing to the short activation time and ultra-fast dynamic response compared to the thermal switching.

The electrical switching of VO_2 was firstly reported by Ovshinsky in 1969 [125]. Then several authors reported electric-field induced switching in two-terminal VO_2 thin

films [126-128]. Lee *et al.* argued that the current flow into a narrow filament generates Joule heat, resulting in the transition of VO_2 films [129]. However, Okimura *et al.* reported an electrical switching response within 200 ns of the VO_2 film on *c*-cut sapphire substrates, suggesting an electrical potential energy induced Mott transition without the contribution of Joule heating [130]. Stefanovich *et al.* discovered that the delay time of VO_2 electrical switch response decreased with the increase of electrical field [9]. It was also reported that the VO_2 showed an S type negative differential resistance in the I-V characteristics, providing potentials in memory elements applications [131]. VO_2 also showed good performance for high frequency devices. Ha *et al.* reported that the VO_2 response to a radio frequency signal showed a rise time of the order of 10 ns followed by an oscillatory damping to steady state on the order of several μs [132]. Furthermore, the VO_2 switch exhibited a long lifetime (more than 260 million cycles without failure) under the 10 GHz microwave signal [133].

Thermochromic smart windows

The smart window is a system that can sense and respond to external stimulus such as heat, electricity, or light. It controls the solar radiation transmission rate through the window, resulting in the reversible control of indoor luminous and temperature. Therefore the smart window is promising in applications of next-generation household or industrial windows for energy saving [134, 135].

VO_2 has attracted a large amount of research interest as a thermochromic smart window material, benefiting to its phase transition at a T_c close to room temperature and

the accompanied abrupt change of optical transmittance [136, 137]. When the environmental temperature is higher than the T_c of VO_2 coating, the transmission of VO_2 film, especially the infrared (IR) light, decreases abruptly. It leads to the effective block of the IR light to make the indoor temperature stay at a lower value. While the environmental temperature is below T_c, the VO_2 transits to semiconductor phase, which results in the improvement of IR transmission to make the indoor temperature increase [84, 138].

The recent research efforts have been primarily focused on enhancing the transmittance, especially the visible light transmittance of VO_2. Multilayered structures were designed by coupling VO_2 with high-reflective-index dielectric top or bottom layers. Jin *et al.* reported a strong enhancement in luminous transmittance of the $TiO_2/VO_2/TiO_2$ anti-reflection structure [139]. The $ITO/VO_2/ITO$ structure reported by Heinilehto *et al.* showed an optical transmittance switch of 34.2% at 1550 nm wavelength [140]. Doping elements were usually introduced to shift the transmission wavelength of VO_2 to visible region [141, 142]. Hu et al. *reported* the Mg-doped VO_2 thin film with a wide band gap of 2.32 eV, which significantly lowered the luminous absorption at visible wavelength [142]. Furthermore, Zhou et al. have reported that VO_2 coating had a strong scattering of the light energy, which could scatter partial light to a solar cell for electricity generation [143]. As shown in Figure 1.10, the solar cells are designed to be assembled around the VO_2 coated smart window. The VO_2 coating was discontinuous to enhance the scattering of light. This design combined energy saving and generation together, which supported an important new insight into resolving the

energy consumption.

Thermal actuators

Thermally activated actuators are widely used in microelectromechanical systems for modern technologies. The traditional design of such devices is a bilayer structure coupling two materials with different thermal expansion coefficients. The bilayer structure bends in response to a temperature change because of the differential thermal expansion (DTE) [144]. The DTE can be as large as 10^{-4}/K for conventional designs [145].

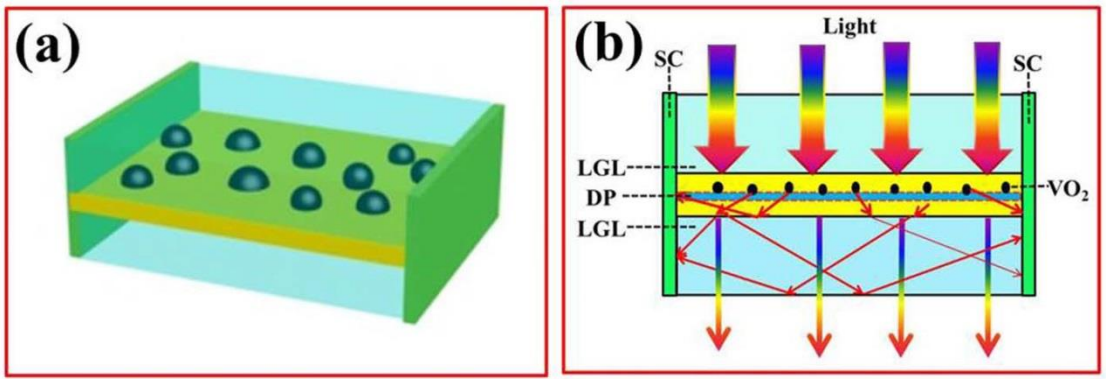

Figure 1.10 (a) Three-dimensional structure of the VO_2-based smart window. The solar cells are assembled in a manner that surrounds the module. (b) The cross-section view of VO_2 film on quartz that served as a scattering medium. SC, LGL and DP represent the solar cell, light guider layer and low reflective index medium, respectively. Reprinted with permission from Scientific Reports [143].

In 2010, a new mechanism for micrometer-sized actuation based on VO_2 phase transition was introduced by Rua *et al* [17]. This design consisted on the use of the crystallographic changes of VO_2 thin films across its structural phase transition. The highly oriented VO_2 thin film deposited on SiO_2 micro-bridge showed a strain of -0.32% during phase transition, leading to the tuning of the micro-bridge resonant frequency up to -23%. The DTE was reported to be an order of magnitude higher than the traditional designs. Based on the novel design, Cabrera *et al.* then fabricated VO_2-Pt MEMS actuators, as shown in Figure 1.11 [146]. The cantilever structures were fabricated through a bottom-up process. Total deflections of 68.7 and 28.5 μm were observed for 300 and 200 μm MEMS cantilevers, respectively. The cut-off frequency (f_{3dB}) of the 300 μm MEMS actuator is 29 Hz in vacuum mostly because of the heat conductivity limitation, whereas the f_{3dB} in atmosphere is as high as 541 Hz.

Single VO_2 nanowires were also reported to have the potential as thermal actuators through inhomogeneity phase transition [147, 148]. J. Cao et al. have reported that VO2 nanowire cantilevers formed discontinuous M1 and R phase domains during phase transition, leading to the curvature of the nanowire [148].

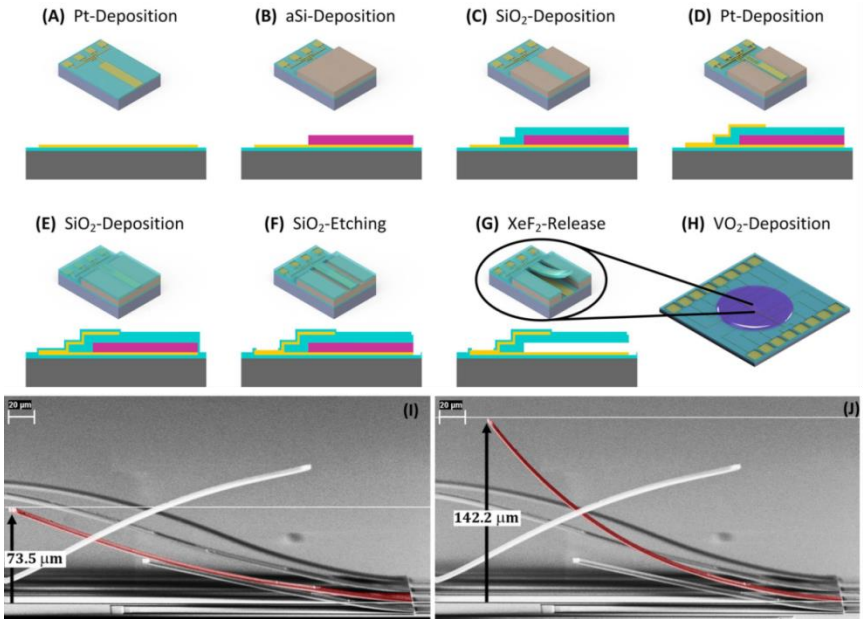

Figure 1.11 Fabrication process of VO_2-Pt cantilever. (a) Bottom electrode deposition and patterning by lift-off, (b) sacrificial layer (amorphous silicon) deposition and patterning, (c) first SiO_2 deposition and patterning, (d) top electrode deposition, (e) second SiO_2 deposition, (f) Patterning of the second SiO_2 layer, (g) release of the MEMS actuator, and (h) VO_2-deposition by pulsed-lased deposition using in-situ shadow mask. (I) The SEM image of the as-fabricated 300 µm cantilever (highlighted in red). (J) The 300 µm cantilever after actuation. Reprinted with permission from IEEE [146].

Memristors

Circuit elements that store information without the need of a power source represent an important change in electronics, allowing for low-power computation and storage. Furthermore, if the information could span into a continuous range of values, analog computation may replace the present digital one [149]. Memory-resistor (memristor) was postulated as such a missing circuit element by Chua in 1971. It was based on an observed symmetry in integral-variations of ohm's law [150]. The most

important characteristic of a memristor is that the resistance of a two-terminal device depends not on the instantaneous value of the applied voltage, but on the entire dynamical history of the charge flowing in the system [151].

The memristor behavior of VO_2 was firstly demonstrated by Driscoll *et al.* in 2009 [18]. As shown in Figure 1.12, the VO_2 thin film exhibited nonlinear hysteretic behaviors through three current-voltage cycles, indicating a memristive system. The operation temperature of this system is close to T_c, where the resistivity is a highly hysteretic function of temperature. Furthermore, the VO_2-based memristor was placed into an LC contour as an adaptive filter. This filter was reported to respond preferentially to signals of a specific design frequency by sharpening the quality factor of its bandpass [152]. In 2013, Bae *et al.* reported a two-terminal memristor device based on a single VO_2 nanowire [153]. The phase transition of the single VO_2 nanowire was driven by the bias voltage of 0.34 V without using any heat source. The device not just provided switchable resistances in a large range of magnitude, but also maintained the resistances by a low bias voltage.

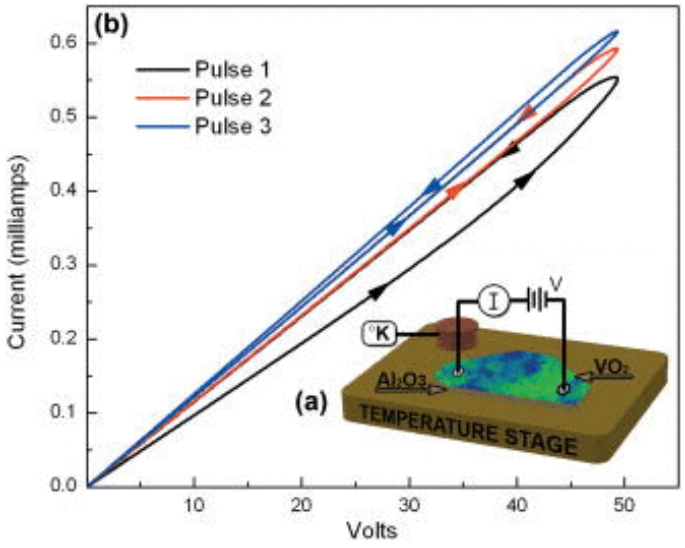

Figure 1.12 (a) Schematic of the VO_2 memristor device. (b) Three cycles of the current-voltage (I-V) curves for the device. The nonlinear hysteretic behavior indicates a memristive system. Reprinted with permission from American Institute of Physics [18].

Several mechanisms have been proposed to describe the memristor behavior of VO_2. The memristor phenomena are commonly explained by way of drifting oxygen vacancies and physical crystal expansion [154]. However, the memristor properties of VO_2 could be related with the nanoscale process of the phase transition, during which nano-size metallic regions emerge from the semiconductor host, increasing in number and size to form a percolating transition [155]. People have also argued the mechanism correlated to the electronic phase separation phenomena in the vicinity of the phase transition, which have been observed in a variety of complex oxides [156, 157]. Currently, the mechanism of the historic memory of VO_2 phase transition is still under debate.

1.3 VO_2 thin films

VO_2 thin films have attracted extensive research interest benefiting to the 2-dimentional geometry, the compatibility with current device fabrications and the capability to stand distortions. The synthesis process of VO_2 thin films could lead to dramatic difference of microstructures, and therefore the SMT properties could vary a lot. This section reviewed some critical questions of VO_2 thin film epitaxial growth and the impact factors on the film SMT properties.

1.3.1 Thin film epitaxy

Epitaxy is an important concept for thin film growth. It refers to the method of growing an oriented crystal layer on the crystal surface of another material. The deposited film is so called epitaxial film or epitaxial layer. The strict definition of epitaxy specifically refers to the growth of a single crystalline film on a single crystal substrate. However, as the substrate and film materials usually have different crystal symmetries and lattice parameters, it is quite difficult to have single crystalline epitaxial growth of the film. Thus generally the epitaxy means the highly orientated growth with fewer defects.

Epitaxy contains two categories: homoepitaxy and heteroepitaxy. Homoepitaxy refers to the case where the film and substrate are the same material. This technique is usually used to grow the film with less defects and higher purity than the substrate, or to fabricate additional layers with different doping levels. A representative example of homoepitaxy is the growth of epitaxial Si on Si substrates by CVD vapor-phase epitaxy

for the first step in IC transistors [158, 159]. The homoepitaxy Si thin film can be easily doped with different doping elements and various concentrations. Heteroepitaxy refers to the case where the film and substrate are different materials, which is a more common case in thin film growth. In heteroepitaxy, the microstructures and properties of the epitaxial films are strongly dependent on the crystal structures, interfacial chemistry, and thermal expansion coefficients of film and substrate. A representative example of heteroepitaxy is the AlGaAs/GaAs superlattice structure for light emission diode (LED) application [160]. The lattice parameter of AlGaAs can be tuned by the Al and Ga concentrations to achieve different film epitaxial qualities.

The homoepitaxy usually has no strained interfacial bonds because of the identical lattice parameters. However, for the heteroepitaxy growth, residual strain will be introduced in the film-substrate interface. The residual strain in the epitaxial film is generated from the lattice mismatch, and it determines the growth characteristics, morphology, chemical and physical properties of films. Therefore it is very imported to understand the lattice mismatch for film quality and property controlling [161].

Lattice matching epitaxy

The lattice matching epitaxy forms a coherent interface with one-on-one lattice matching between film and substrate. Thus the lattice constant of the thin film in the plane of the interface is equal to the substrate. The in-plane lattice misfit of this scenario is defined as:

$$f = 2 \times \frac{a_{film} - a_{substrate}}{a_{film} + a_{substrate}} \quad (1.3)$$

Due to the constraint on the in-plane lattice constant, the unit cell will be distorted as allowed by Poisson's ratio. As shown in Figure 1.13, a cubic unit cell is distorted into a tetragonal cell. As $a_{film} > a_{sub}$, the cell of the film is confined in the in-plane direction and its height is increased.

The coherent epitaxy with a strained layer can only accommodate the lattice mismatch strain of less than 2%. For the case of $f > 2\%$, pseudomorphic growth will be initiated from a critical thickness. The strain energy beyond the critical thickness is large enough to trigger the formation of dislocations, leading to the strain relaxation of the film, as shown in Figure 1.13 (c). Through such a Pseudomorphic growth, the lattice matching epitaxy could accommodate the lattice mismatch strain up to 7-8% [162].

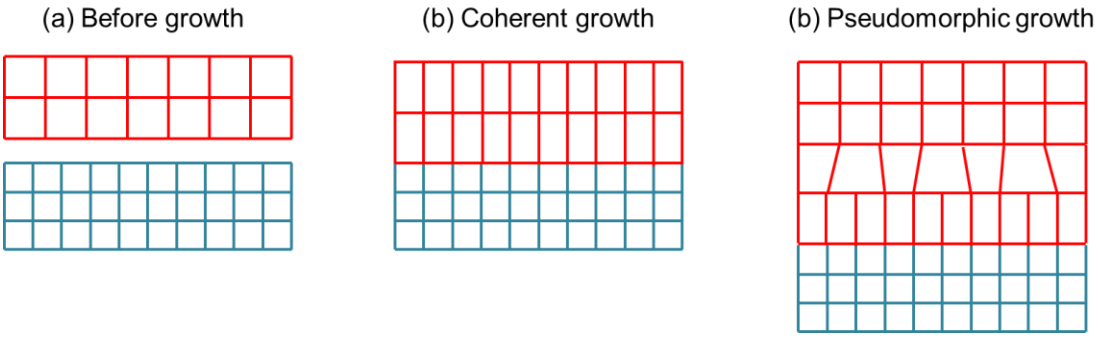

Figure 1.13 Schematic illustration of lattice matching epitaxy: (a) before growth, (b) coherent growth and (c) pseudomorphic growth.

Domain matching epitaxy

When the system has a lattice mismatch larger than 8%, the conventional lattice matching epitaxy is unable to accommodate the strain to establish an epitaxial growth of the thin film. However, epitaxial growth was also observed in this kind of systems, such as sapphire ZnO(0001)/Al_2O_3(0001) [163] and TiN(100)/Si(100) [164]. These epitaxial growths are understood as domain matching epitaxy, which was proposed in 2003 [162]. Based on the domain matching epitaxy theory, an epitaxial film can be deposited on the substrate with different lattice matching orientations. For example, the film lattice can match in the diagonals of the substrate lattice, such as the cube-on-hexagonal epitaxy. Besides, the lattice misfit can be accommodated by matching of integral multiples of lattice planes, where one extra half plane (dislocation) corresponding to each domain. Therefore for the domain matching, the large residual strain can be relaxed within a couple of monolayers, so that the misfit strain and dislocations can be engineered and confined close to the interface, as shown in Figure 1.14. As the residual strain is minimized by matching of m planes of films with n planes of substrate (|m-n|=1), the lattice mismatch of this scenario is defined as:

$$f = 2 \times \frac{ma_{film} - na_{substrate}}{ma_{film} + na_{substrate}} \quad (1.4)$$

If the lattice mismatch corresponds to the perfect matching ratios of planes ($ma_{film} = na_{substrate}$), the residual strain will be eliminated. When the lattice mismatch is away from perfect matching, the residual strain can be released by two domains alternating with a certain frequency (α) to provide for a zero residual strain, i.e. $(m+\alpha)a_{film} = (n+\alpha)a_{substrate}$.

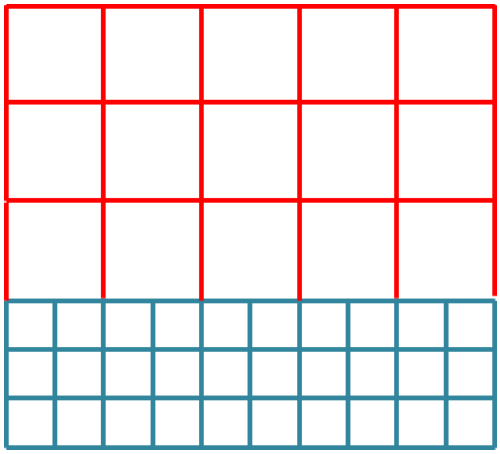

Figure 1.14 Schematic illustration of domain matching epitaxy.

1.3.2 SMT modelling of VO_2 thin films

The SMT properties of VO_2 can be characterized by the electrical resistivity switching with four parameters: the transition temperature (T_c), the amplitude of resistivity change (ΔA), the transition sharpness (ΔT), and the width of thermal hysteresis (ΔH). It is desired to have a tunable transition temperature, large amplitude of resistivity change with a sharp transition and a small width of thermal hysteresis. However, despite of the excellent SMT properties of single crystalline bulk VO_2, the SMT properties of VO_2 thin films can be influenced by a lot of factors.

In 2006, a thermal dynamic model has been proposed by Narayan *et al.* for the

microstructure-property correlations of VO_2 thin films based on defect density and interfacial energies [37]. The model argued that the structural phase transition from monoclinic to tetragonal phase is accompanied with a Gibbs free energy change, which can be derived as $\Delta G_r = \Delta T_r \Delta S_0$. Here the ΔT_r is the deviation from the equilibrium transition temperature and the ΔS_0 is the change in entropy between two phases. As the monoclinic to tetragonal and the reverse structural phase transitions can both be accomplished by a single coordinated atomic jump, the propagation rate of velocity of phase transition is then derived as:

$$V = \lambda v_D exp^{-\Phi/kT} \tag{1.5}$$

where λ is the jump distance of the coordinated atom (~1 Å for VO_2), v_D is frequency of atomic jump, and Φ is the activation barrier. The value of Φ approximately equals to kT_r, where k is the Boltzmann constant and T_r is the transition temperature [165]. If assuming $v_D = 10^{12}$ s^{-1}, the transition velocity can then be estimated to be ~40 m/s. This estimation agrees well with the experimental report by *Cavalleri et al.*, which conducted time resolved, near-edge X-ray absorption measurements for VO_2 phase transition velocity [166].

It was reported that the VO_2 phase transition started with the nucleation of nano-sized metallic phases in the semiconductor host. These regions increased in numbers and sizes and finally formed a percolating transition [155]. Thus the behavior of this VO_2 phase transition can be described by the nucleation model, from which the critical size (r_c) of stable nuclei can be derived as [37]:

$$r_c = 2\gamma/(\Delta T_r \Delta S_0) \tag{1.6}$$

where γ is the interfacial energy. Based on the above thermal dynamic model, it is able to predict the influence of VO_2 thin film microstructures on the SMT parameters, i.e. ΔA, ΔT, ΔH and T_c.

The transition sharpness (ΔT) is proportional to the overall defects density, i.e. $\Delta T = C_t\rho_d$. Here C_t is a constant and ρ_d is the overall defect density, including point defects, dislocations, and grain boundaries, impurities, etc. Therefore the ΔT is determined by the overall defect content per unit volume. The transition amplitude (ΔA) also depends on the defect content. It has an inverse proportional relationship to the defect density, i.e. higher-quality VO_2 thin films with fewer defects could lead to a larger ΔA. The thermal hysteresis ΔH is directly related with the transition temperature derivation ΔT_r. As the Gibbs free energy for VO_2 phase transition requires a finite ΔT_r, the ΔH is inevitable for both single crystalline bulk and thin film VO_2. From the model, it can be derived that $\Delta T_r = 2\gamma/(r_c\Delta S_0)$. Therefore, the ΔH increases with the decrease of nuclei size. Besides, the interfacial energy γ is related with the nature and orientation of grain boundaries. Large angle, randomly oriented grain boundaries could lead to large interfacial energy, resulting in the increase of ΔH. T_c is directly related with the stress/strain status of the VO_2 film, which has been discussed in the VO_2 stress-temperature phase diagram (Figure 1.7).

1.3.3 Substrate and buffer layer effects

The microstructures of VO_2 thin films can be influenced by a lot of parameters. The choice of substrates and buffer layers will directly impact the growth orientation,

crystallinity, strain status and defects density, and thus the SMT properties of the VO_2 thin films. Various substrates have been used for VO_2 thin film growth with different purposes. Among all, *c*-cut sapphire substrate is commonly used to grow epitaxial VO_2 thin films [28, 167]. The films are highly textured along (001) or (010) on sapphire (0001) substrate [168]. Si substrates are used to achieve the compatibility with current electrical devices. They are cheaper compared to sapphire ones. However the VO_2 thin films deposited on Si were usually reported to be polycrystalline because of large lattice mismatch and the native oxide layer [169]. Glass substrates were usually used for optical applications owing to the low cost and high transparency. VO_2 films directly grown on glass substrates were reported to be monoclinic phase with preferred (011) out-of-plane orientation, however with random in-plane orientations [30]. MgO (111) and STO (111) substrates were used to achieve *b*-axis growth of VO_2 [51].

Besides the substrate exploration, different buffer layer materials were also applied to achieve better epitaxial quality of the VO_2 films. TiO_2 has a good lattice matching relationship with VO_2. Muraoka *et al.* reported that VO_2 preferred to grow along (001) on TiO_2 (001) while tended to grow along (011) on TiO_2 (011) [170]. It indicated that the lattice orientation of TiO_2 buffer layer could determine the growth orientation of VO_2. ZnO has a domain matching relationship with the VO_2 lattice. Many researchers have reported high quality VO_2 thin films on ZnO or doped-ZnO buffer layers [136, 171, 172]. As ZnO could also grow epitaxial on Si substrates [173], it provides a transition between VO_2 and Si. In addition, SnO_2 and CeO_2 were reported as an antireflection layer for thermaochromic applications of VO_2 [174, 175].

Because of the different lattice mismatch relationships, the substrates and buffer layers not only influence the microstructures, but also impact the strain states of the VO_2 thin films. In fact, the strain has been controlled by using various substrates and buffer layers for the growth of VO_2, which results in successful T_c tuning of the films. VO_2 thin films on STO (111) [51] and *r*-cut sapphire [176] substrates were usually reported to have a lower shift of T_c, while the VO_2 on MgO (111) [177] and *c*-cut sapphire substrates [28] commonly showed an upper shift of T_c. In addition, different buffer layers, such as TiO_2, CeO_2, ZnO, SnO_2, etc., have been applied between VO_2 and substrates to provide more possibility of strain tuning [136, 170, 175, 178, 179].

This section is focused on reviewing the lattice structures and the corresponding VO_2 growth impacts of sapphire, Si, glass and ZnO, which have been used in the works of this thesis.

Sapphire

Sapphire belongs to the inorganic compounds with the chemical formula Al_2O_3. It is also called aluminum oxide, alumina, corundum, as well as many other names, depending on the applications. Al_2O_3 has a rhombohedral/hexagonal crystal structure ($R\bar{3}c$) with ionic bonds. Figure 1.15 shows the hexagonal unit cell with 12 Al^{3+} ions and 18 O^{2-} ions. The lattice of the hexagonal unit cell consists of close packed oxygen planes, alternating with a hexagonal array of aluminum planes [180, 181]. The lattice parameters of Al_2O_3 are a=4.7587 Å and c=12.9929 Å. Sapphire is an insulator with a band gap of 9 eV at room temperature [182]. The thermal expansion coefficients of sapphire are

6.2×10^{-6} and 7.07×10^{-6} cm/k along *a*- and *c*-axes, respectively [183].

There are four commonly used face terminations of sapphire as substrates: (0006) (*c*-plane), $(10\bar{1}2)$ (*r*-plane), $(1\bar{1}00)$ (*m*-plane), and $(11\bar{2}0)$ (*a*-plane), among which *c*- *r*- and *m*-cut sapphires have been used for VO_2 growth. The VO_2 on *c*-cut sapphire shows the best epitaxial quality with (002) growth orientation. However, many researchers still reported relatively low SMT properties of VO2 on *c*-cut sapphire. Yang *et al.* demonstrated that it could be caused by the formation of $120°$ domain boundaries of the VO_2 on *c*-cut sapphire due to the three-fold symmetry of the sapphire *c*-plane [28]. VO_2 on *r*-cut sapphire was reported to have a tetragonal phase (011) growth orientation at elevated temperature during depositions. When cooling down, the monoclinic phase formed $(\bar{2}11)$ and (200) twin structures [26, 176, 184]. VO_2 has a large lattice mismatch with the sapphire *m*-plane, which results in several growth orientations [184].

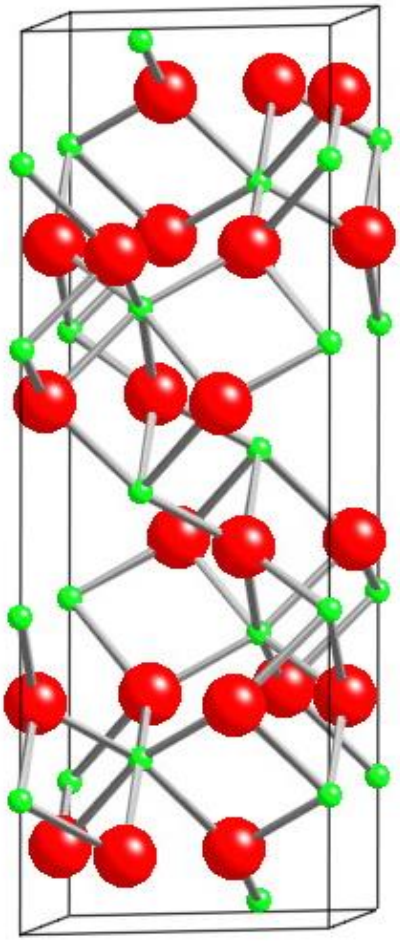

Figure 1.15 Atomic structure of hexagonal sapphire unit cell. Red balls represent O^{2-} and green balls represent Al^{3+}.

Silicon

Silicon (Si) is one of the most abundant elements in earth and serves as the most commonly used material in the current integrated devices. Si has a face-centered diamond cubic crystal structure with a lattice constant of ~5.431 Å, as shown in Figure 1.16. Si has an indirect band gap of 1.12 eV at room temperature. The n-type and p-type

Si can be fabricated by doping of phosphor (P) and boron (B). The pure Si wafer forms a native oxide layer, SiO_2, of about 3 nm on top [185]. As the SiO_2 layer has an amorphous structure, it strongly limited the epitaxial growth of thin films on Si substrates.

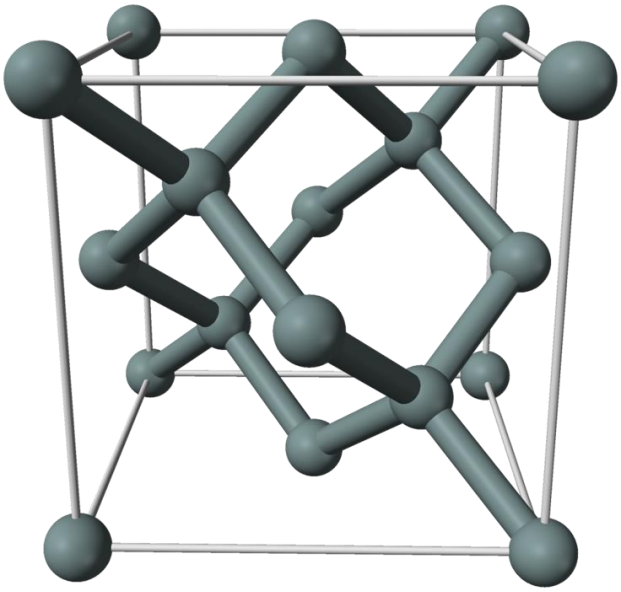

Figure 1.16 Atomic structure of the face-centered diamond cubic Si unit cell.

As Si is widely used in the current integrated devices, it attracted extensive research interest to achieve high performance VO_2 thin films on Si substrates. However,

the VO_2 directly grown on Si was usually reported to be polycrystalline [186, 187], and sometimes even with the existence of other phases [188]. Therefore, transition buffer layers were usually used in between of VO_2 and Si to enhance the epitaxial quality of the VO_2 film. The buffer layers are required to have good lattice matching relationship with both Si and VO_2 to provide intermediate lattice structures to accommodate the large lattice mismatch between Si and VO_2. Buffer layers including ZnO [29], Al_2O_3 [189], yttria-stabilized zirconia (YSZ) [190], etc. have been reported to have a good enhancement of the quality and therefore the performance of VO_2 on Si.

Soda-lime glass

Soda-lime glass is the most prevalent type of glass, and commonly used for windowpanes and glass containers. It is prepared by melting the raw materials, such as sodium carbonate (soda), lime, dolomite, silicon dioxide (silica), aluminium oxide, in a glass furnace at temperatures locally up to 1675 ℃. The soda-lime glass has an amorphous structure with a melting temperature of ~570 ℃. Soda-lime glass as substrate is cheap, relatively chemically stable, reasonably hard, and extremely workable. It has a large optical transparency window from the wavelength of 400 nm to 2700 nm with larger than 90% transmission, as shown in Figure 1.17. Therefore, it is widely used as the substrate for optical applications.

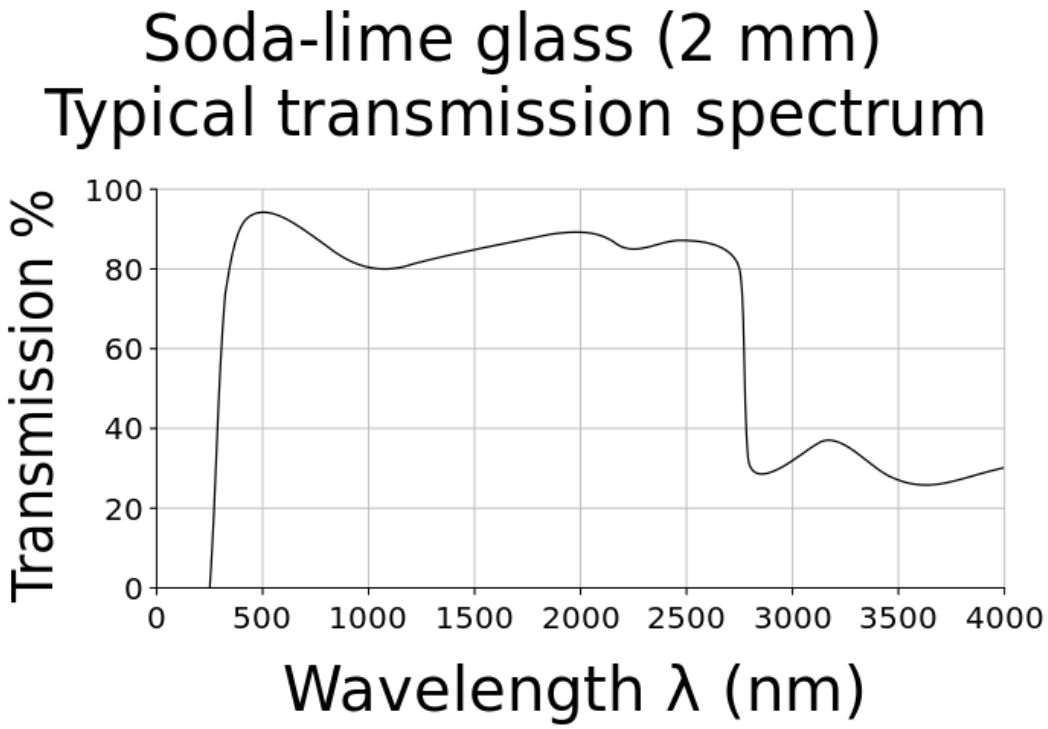

Figure 1.17 Transmission spectrum of the soda-lime glass.

The VO_2 thin film grown on soda-lime glass substrate has the advantages of low cost, small substrate effects, and high optical performance for smart windows [16]. However, compared to the research works of VO_2 thin films on sapphire and Si substrates, the effort on the growth of high quality VO_2 thin films on glass substrates is much less. In general, VO_2 thin films on glass substrates have been reported to have relatively poor SMT performances [30, 178, 191, 192]. For example, Hanlon et al. reported that a sputtering deposited VO_2 film on glass substrate exhibiting a phase transition width as large as 10 ℃ [191]. The VO_2 film on glass substrate reported by

Chiu et al. showed an 11 ℃ width of thermal hysteresis [178]. Further research works on the VO_2 growth on glass is desired for future optical device applications.

Zinc oxide

ZnO is a II-VI group semiconductor. It crystallizes in two main forms, hexagonal wurtzite and cubic zincblende [193]. The wurtzite structure is a more stable phase and thus more commonly used for both research and industry applications. It belongs to P63mc with the lattice parameters of a=3.2498 Å and c=5.2066 Å. As shown in Figure 1.18, the wrutzite ZnO lattice is composed of two hexagonal close packed (HCP) sublattices of Zn and O atoms. ZnO has a wide direct bandgap of Eg = 3.37 eV at room temperature, which makes it suitable for blue and ultraviolet (UV) optoelectronics and transparent electronics [194]. The bandgap can be varied from 3.0 to 4.0 eV through Cd and Mg substitution [195, 196]. The native doping of ZnO due to oxygen vacancies or zinc interstitials is n-type [197].

ZnO has been reported as a good buffer layer for VO_2 growth [172]. Both *b*- and *c*-axes of VO_2 growth have been achieved on ZnO [171, 178]. Kato *et al.* reported a *b*-axis growth of monoclinic VO_2 on ZnO buffered glass substrates with the β angle of VO_2 lattice matches on 120° ZnO hexagonal lattice. The heteroepitaxial relationships were determined as VO_2 (010)[100]||ZnO (001)[100],[010],$[\bar{1}\bar{1}0]$ [136]. This result was supported by the research works from Srivastava *et al.* and Chiu *et al.* [192, 198] However, Yang *et al.* and Koo *et al.* reported the *c*-axis growth of VO_2 on ZnO (0006) [171, 199]. The lattice matching relationships were determined as VO_2 (002)||ZnO (0002)

and VO_2 $(0\bar{1}0)||ZnO$ $(10\bar{1}0)$. These results indicated that the epitaxial orientations of VO_2 on ZnO buffer layers could be influenced by specific synthesis processes.

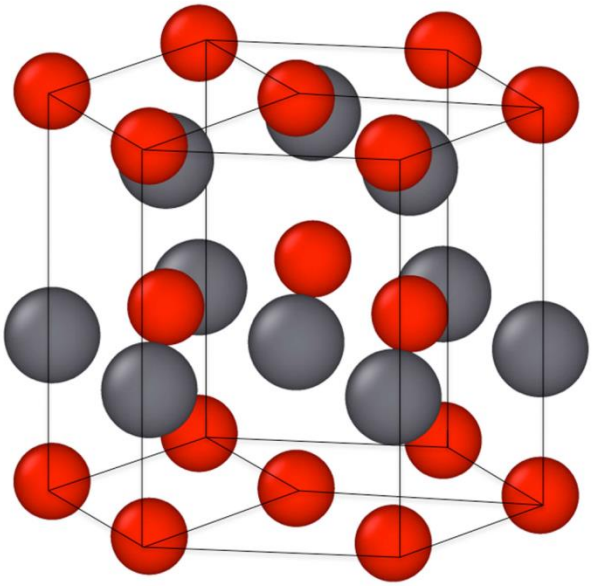

Figure 1.18 Hexagonal wurtzite crystal structure of ZnO with Zn^{2+} ions shown as red and O^{2-} shown as gray.

1.3.4 Defect effects

The defects are the imperfection of the periodic crystal structure. They widely exist in almost all kinds of crystals. The defects can be categorized by the dimensions. The 0 dimension (0-D) defects are called point defects, which includes vacancies,

interstitial atoms, etc. The 1-D defects mainly refer to dislocation related defects. The 2-D defects are in planar shape, such as grain boundaries twin interfaces, domain walls, etc. The 3-D defects are the clusters in the crystal matrix, including voids, cracks, inclusions or secondary phases. The VO_2 thin films usually contain many kinds of defects. Despite of the theoretic prediction of the thermal dynamic model introduced in section 1.3.2, the practical defect effects on the SMT properties of VO_2 thin films is still under investigation. Especially, the mechanisms of defects influence on VO_2 SMT properties are still under debate.

Point defects exist in all kinds of crystal structures including VO_2 thin films because of the thermal energy. The point defects were reported to have a negative impact on the film SMT properties. Lopez *et al.* reported that by annealing the as-deposited VO_2, the point defects could be reduced, leading to a larger phase transition amplitude and sharper transition [112]. In particular, the oxygen vacancy was reported to have a tuning effect on the T_c of VO_2 thin films [23]. Appavoo *et al.* have conducted plasmon resonance nanospectroscopy characterizations on VO_2 at nuclei stage [115]. The VO_2 with higher oxygen vacancy density showed a T_c shift to lower temperature, which was correlated with the vacancy generated strain at grain boundaries.

Dislocations in the VO_2 thin films can usually be observed at the film/substrate interface due to the lattice mismatch [200]. Kawatani *et al.* have reported the dislocation generation at the VO_2/TiO_2 interface [201]. The increase in dislocation density in thicker films caused the overly broadening of the transition sharpness. Furthermore, the local area phase transition study by Sohn *et al.* revealed that the VO_2 film near the

dislocations had a T_c shifting to the bulk transition temperature, owing to the strain relaxation by forming dislocations [202].

Grain boundary (GB) is a 2-D defect. As one of the major defects widely existing in the VO_2 thin films, it has dramatic influence on the SMT properties of VO_2 thin films. The GB is generally believed to have negative impacts on the film SMT properties. Brassard *et al.* demonstrated that when VO_2 grew thicker on Si_3N_4/Si substrates, the grains gradually grew larger in the top parts of the thin films and result in a sharper phase transition and larger transition amplitude [22]. However, Aliev *et al.* have reported a different result. It was found that the grain size increase of VO_2 thin films on Al_2O_3 and Si substrates led to the reduction the width of thermal hysteresis but broadening of the phase transition sharpness [203].

The 120 ° twin boundary is another type of 2-D defects that have widely been observed in the VO_2 films deposited on the substrates with hexagonal lattice symmetry, such as *c*-cut sapphire. A negative impact on the SMT properties was also reported. Moreover, Yang *et al.* have reported that this impact would be more significant when the electrical current went through the twin interfaces perpendicularly [171]. The SMT measurements conducted on in-plane and out-of-plane direction of the VO_2 film showed that the parallel current flow had a sharper transition with a smaller ΔH compared to the perpendicular current flow.

Secondary phases usually exist in the VO_2 thin films synthesized at un-optimized conditions. As the VO_x phases had different composition and phase transition temperature from VO_2, they were usually reported to cause a decrease of the VO_2 film

transition amplitude [204, 205]. However, the pre-existence of R phase VO_2 in the M1 phase matrix was reported to cause limit impacts on the transition amplitude and sharpness, but result in an easier transition of the M1 phase matrix to the R phase [206]. It was proposed that the R phase clusters provided nucleus which lowered down the activation energy for the surrounding M1 VO_2 phase transition.

In fact, due to the co-existence of other defects, it is very challenging to study the individual defect effects on VO_2 SMT properties. Furthermore, film thickness and the stress induced by substrates could also affect the SMT properties of VO_2 thin films. Therefore, it is desired to study the effects of defects on VO_2 films by limiting the existence of other defects and minimizing the substrate induced stress [207].

1.3.5 Doping effects

In semiconductor production, doping is to intentionally introduce impurities into an extremely pure intrinsic semiconductor for the purpose of modulating its electrical properties. In general, the doping in an intrinsic semiconductor will lead to the narrowing of the energy band gap by introducing extra energy states between the conduction and valence band, which results in higher conductivity of the semiconductor. For the case of VO_2, since it's intrinsically in n-type, any acceptor doping will compensate for undoped n-type VO_2 and thereby lower down its energy gap. Therefore the n-doped VO_2 film requires lower thermal energy to trigger the phase transition, leading to the drop of T_c [36, 208]. Furthermore, Macchesn *et al.* reported that when the dopant radius is larger than V^{4+}, it can lead to the drop of T_c, and while the dopant has a

smaller radius than V^{4+}, it will increase the T_c [32].

Doping is one of the most common ways to tune the T_c of VO_2. Various doping elements, including W, Mo, Nb, Mg, Al, Ti and Cr, have been achieved and the T_c of the films has been tuned from less than 200 K to more than 350 K. However, since doping elements could introduce extra defects in the VO_2 lattice, it is usually accompanied with a drop of other SMT properties including lowering of ΔA, broadening of ΔT, and decreasing of optical transmission switch. In 1983, Greenburg reported CVD synthesis of W, Mo and Nb doped VO_2 thin films. All the doping elements led to a drop of T_c, but caused a decrease of the transmission switch at infrared wavelength during phase transition [25]. Jorgenson *et al.* then varied the W doping concentration from 0-7% in the VO_2 thin films [32]. They reported a decrease of the T_c from 340 K to 160 K, which covered the operation temperatures (~280-310K) for normal devices. However, the electrical resistance transition amplitude was observed to drop with the W doping. The first-principles calculations by Tan *et al.* revealed that an isolated W ion in VO_2 lattice possesses an intrinsically symmetric tetragonal-like structure, which drives the de-twisting of the nearby asymmetric monoclinic VO_2 lattice towards rutile phase [209]. These W generated rutile-like VO_2 regions acts as nuclei for the "metallic puddles" which propagate through the monoclinic matrix, and thus lowering down the thermal activation energy across phase transition.

Hanlon et al. reported Mo-doped VO_2 thin films on glass substrates exhibiting a drop of T_c from 62.5 ℃ to 24 ℃ with the doping concentration increasing from 0 to 7% [210]. The films showed a dramatic drop of conductivity transition amplitude and

broadening of transition width with the increase of Mo concentration. Xu *et al.* further characterized that the transition amplitude drop could be as large as 2-3 orders with 5% of Mo concentration variation, as shown in Figure 1.19 [211]. Wu *et al.* have conducted high resolution X-ray diffraction characterizations on Mo-doped VO_2 thin films on *c*-cut sapphire substrates [208]. The results showed a comparable epitaxial quality of doped and undoped VO_2 films, indicating limited defects induced by Mo doping. Mai *et al.* argued that Mo doping resulted in the loss of V^{4+}-V^{4+} pairs. It not only destabilized the semiconductor phase, which led to the drop of T_c, but also caused the bond damage of the monoclinic lattice, which resulted in the decrease of transition amplitude.

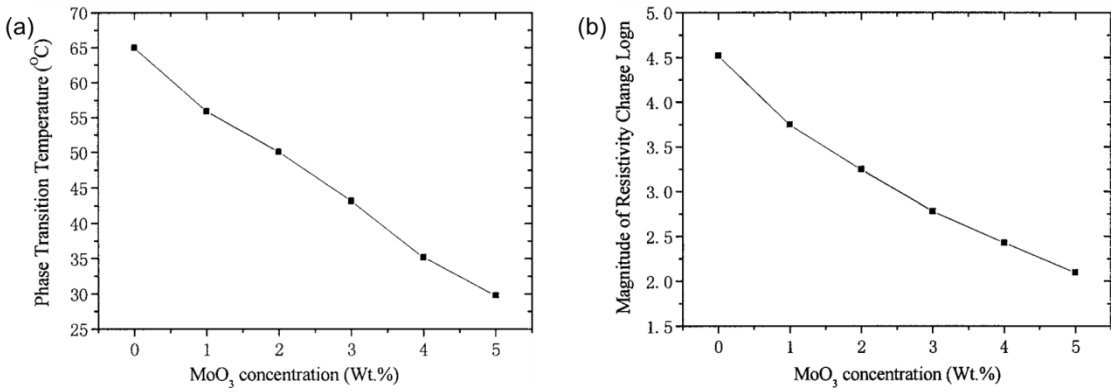

Figure 1.19 The effects of MoO_3 doping concentration on (a) the T_c and (b) the magnitude of resistivity change of the VO_2 thin films. Reprinted with permission from Journal of Materials Science [211].

In contrast to the high valent elements (W^{6+}, Mo^{6+}, Nb^{5+}, etc.), the low valent elements, including Al^{3+}, Cr^{3+}, Ti^{4+} were reported to tune the T_c of VO_2 to higher temperatures during doping. Chae *et al.* reported an increase of T_c of VO_2 thin films by 10 K with 20% Ti doping concentration [35]. Furthermore, Takahashi *et al.* found that the T_c of VO_2 was less sensitive to the doping concentration for heavily doped (>15%) samples [34]. They reported that about 15 K increase of T_c of VO_2 thin films was accomplished by 15% of Ti doping, while the T_c showed almost no change with the Ti concentration increased to 20%. Beteille *et al.* also reported less sensitivity of VO_2 transition temperature at high doping level. But they revealed that the ΔA still kept decreasing despite of the relatively stable T_c [36]. This indicated that the high level doping will keep on increasing the defects density in the VO_2 film but can't introduce much more energy states in the band structure. In addition, Beteille *et al.* have introduced Al and Cr as doping elements for VO_2 thin films [36]. These elements showed similar doping effects as Ti, but with higher T_c tuning capability, i.e. larger T_c shift at the same doping level, because of the lower valent.

As discussed above, introducing doping elements is usually accompanied with the decrease of ΔA and broadening of ΔT. However, most reports showed that the width of thermal hysteresis (ΔH) decreased with the doping level [212, 213]. This could be because the doping elements played different roles during the M1 to R and R to M1 phase transition processes. Chen *et al.* reported that for the Ti-doped VO_2 thin films, the T_c in the cooling circle increased more than that in the heating circle, leading to a decrease of ΔH [214]. Based on the first-principles computation, they argued that dopant

Ti ions break the octahedral symmetry of local structure in VO_2 (R) phase, which is a nonlocal effect because the distortion is propagated in anisotropy. On the other hand, the Ti induced structural change in VO_2 (M1) phase is only constrained in the local positions of Ti ions. The energy calculation showed that the activation barrier has more increase in Ti-doped VO_2 (R) phase than that in Ti-doped VO_2 (M) phase, resulting in more increase of T_c in cooling circle than that in heating circle. For the acceptor doping elements (W^{6+}, Mo^{6+}, Nb^{5+}, etc.), the increase of the activation barrier in VO_2 (R) phase leads to less decrease of T_c in cooling circle, which also results in the reduction of ΔH.

To limit the reduction of SMT properties of VO_2 thin films due to doping, co-doping has been applied, by which two or more elements have been simultaneously doped in the VO_2 films. Takahashi *et al.* have reported the co-doping of W-Mo and W-Ti [34], while Burkhardt *et al.* have reported the co-doping of W-F in VO_2 thin films [215]. With the remaining of T_c shift, the phase transition amplitude of the films has been enhanced compared to the single doped samples. It is suggested that the co-doped elements have some compensation between the lattice distortions they generated in the VO_2 matrix, which minimizes the defects in the films. Meanwhile, they independently introduce energy states in the VO_2 band structures, which result in the remaining of T_c tuning effects on the films.

The doping effects are mainly based on the change of VO_2 band energy structures. Thus they are at least partially independent from the strain effects. Therefore the doping and strain effects can have combined influence on the VO_2 phase transition temperature. Du et al. reported that an undoped VO_2 thin film prepared by polymer-assisted

deposition showed a T_c of 57.1 ℃ due to the large internal strain. With 5.7% of Ti doping, the T_c of the film shifted to ~80 ℃ without obvious change of the strain status [213]. The 5.7% Ti-doped film even showed a narrowing of transition width with almost no drop of the transition amplitude. The combination of doping and strain effects provides an efficient way with simultaneous T_c tuning and other SMT properties optimization of VO_2 thin films.

1.4 *In situ* transmission electron microscopy (TEM) studies on VO_2

1.4.1 *In situ* TEM characterization techniques

Transmission electron microscopy (TEM) is one of the most widely used techniques to characterize the micro/nanostructures of a material. It can provide a projection view of the microstructures in atomic level, which leads to fundamental understandings of the materials. In addition, it has the capability to identify the internal structure underneath of the surface while the electrons transmit through the TEM specimens, which distinguished this technique from other microscopies. Owing to such great potential, the TEM technique is not just limited in the field of material science researches, but also employed in other areas such as microelectronic device technology, biotechnology, etc. However, conventional TEM techniques can only characterize the microstructures but the physical or chemical properties of the materials. The property measurements were generally conducted *ex situ*, i.e. out of the TEM column. Therefore,

conventionally the microstructure and property characterizations were separated from each other, which make a big challenge to reveal the fundamental mechanisms of the material behaviors.

In the past two decades, the emergence of *in situ* TEM techniques gives the possibilities to characterize the microstructures in real time during property measurements of the materials, which provides great opportunities to correlate structure-property together for fundamental mechanism studies. In general, the *in situ* TEM refers to the techniques conducting property measurements on a TEM specimen inside the TEM column. The microstructure evolutions of the specimen can be directly observed during property measurements. The *in situ* TEM techniques can be classified by the type of property measurements conducted. The most commonly used techniques are including *in situ* TEM heating, mechanical testing, electrical measurement, electrochemical testing, etc.

In situ TEM heating

The *in situ* TEM heating technique conducts thermal measurements on the specimen in the TEM column. The two most important requirements for *in situ* TEM heating are the capability to reach high temperatures and the thermal stability of the system. The instability of the TEM holder at elevated temperatures could lead to the drift of the specimen and thus loss the possibility to characterize the microstructures. The heating source is usually provided by the Joule heat, which is generated by conducting electrical current into a metal filament. In this design, the heating source is separated

from the specimen, thus minimizes the sample instability.

The *in situ* TEM heating techniques have been widely used for the investigation of defects evolution, grain growth, solid interaction, and phase transition process, etc. Here several representative works using the *in situ* TEM heating technique are introduced. Fan *et al.* have conducted *in situ* TEM heating experiments on the FeZr nanocomposites with micron-sized Fe grains [216]. It was directly observed that the dislocations were generated inside the Fe grains at when heating up to 550 ℃. Then the dislocations were driven to the outside of the grains and absorbed by the grain boundaries. The accumulation of large amount of dislocations at the grain boundaries finally led to creation of a gap surrounding the grain. Dannenberg *et al.* have characterized the thermal response of nanocrystalline Ag thin films by *in situ* TEM heating [217]. The growth of Ag nano-grains was observed beyond 100 ℃. More interestingly, it was found that the grain growth was not uniform, but with the formation of large grains surrounded by much smaller grains. Su *et al.* have examined the thermal stability of amorphous SiOC and crystalline Fe composite by *in situ* TEM heating [218]. The diffusion of Fe into SiOC was observed at elevated temperatures. Furthermore, the diffusion was found to be more sever at the triple-point junctions where a grain boundary intersects the layer interface. Dorcet *et al.* have reported the *in situ* TEM experiments on $Na_{0.5}Bi_{0.5}TiO_3$ (NBT) [219]. It was revealed that the rhombohedral to tetragonal phase transition of NBT was a two-step process. The process began by a first order phase transition involving the reconstructive transformation of the rhombohedral phase into an orthorhombic one. Then the intermediate orthorhombic phase turned to the

tetragonal one in a short time.

In situ TEM mechanical testing

The *in situ* TEM mechanical testing technique conducts mechanical measurements on the specimen in the TEM column. Two of the major catalogs of this technique are *in situ* TEM nanoindentation and tensile testing. A typical design of the *in situ* nanoindentation TEM holder consists of a piezo controlled diamond indentation tip connected with a capacitor force sensor. The TEM specimen is required to be half ring to allow the access of the tip. During *in situ* TEM nanoindentation tests, the diamond tip propagates towards the specimen with simultaneous recording of the force. Therefore, the microstructure evolution can be monitored in real time together with the force-displacement plot. The specimen for in situ TEM tensile testing is usually free standing. The TEM holders contain different types of specially designed clamps to catch the specimen. One side of the clamps is fixed while the other side is connected with a piezo controller. The tensile testing will be initiated by retracting the movable side of the clamps.

A representative type of applications of the *in situ* TEM mechanical testing technique is for analysis of microstructural response of a material under the external stress applied with real time observation. Legros *et al.* have conducted *in situ* TEM tensile testing on the free-standing nanocrystalline Al thin films [220]. Extensive grain boundary migrations have been observed accompanied with the *in situ* loading, which resulted in the grain growth for more than 50 nm. Lee *et al.* have reported a direct

observation of strain hardening in nanocrystalline nickel by *in situ* TEM nanoindentation [221]. Abundant Lomer-Cottrell (L-C) locks were observed to form both within nano grains and against twin boundaries, which were believed to contribute to the strain hardening effect. Bufford *et al.* have conducted *in situ* TEM nanoindentations on nano-twined Al thin films [222]. Incoherent twin boundaries were observed to migrate by the assistant of dislocation nucleation and absorption, which result in the high work hardening capacity and plasticity.

The *in situ* TEM mechanical testing technique was also conducted on investigating stress induced phase transitions. Liu *et al.* have reported a reversible gradual $L2_1$-to-10M/14M phase transition of single crystalline $Ni_{54}Fe_{19}Ga_{27}$ alloy at low stress by *in situ* TEM nanoindentation [223]. Furthermore, an irreversible abrupt transition from residual $L2_1$ to $L1_0$ martensite was observed at higher stress during nanoindentation. The dynamic observation of microstructure evolution showed that the reversible phase transition at lower stress involved gradual propagation of phase front accompanied by stress plateau, while the irreversible phase transition at higher stress took place in a discrete fashion.

In situ TEM electrical measurement

In general, the *in situ* TEM electrical measurement is to apply electrical field on the specimen in the TEM column while record the current response simultaneously. The *in situ* TEM electrical measurement holder usually consists of a metal tip (made by W, Pt, etc.) serves as the electrical contact. The specimen is required to be free standing or half

ring for the tip access. The specimen is hold in a metal container which connects to the other end of the electrical power.

The *in situ* TEM electrical measurement technique has been applied on investigating the microstructure evolution of materials under electrical field. Among all, the *in situ* TEM characterizations on conducting channel formation in oxide semiconductors are of particular interest. Park *et al.* have conducted *in situ* TEM electrical measurements on the asymmetric Ta_2O_{5-x}/TaO_{2-x} bilayer structure [224]. The result showed clear mersister behavior of the structure with reversible bipolar resistive switching. The dynamic observation of atomic-scale structure evolution suggested that the switching effects occurred by the formation and annihilation of oxygen conducting channels in the TaO_{2-x} layer, which consist of nanoscale TaO_{1-x} filaments. Similar results were reported by Yang *et al.*, who have conducted *in situ* electrical measurements on $La_{0.85}Sr_{0.15}TiO_3/SrTiO_3$:Nb (LSTO/STON) thin films. The electrical resistance switching behavior of the film was correlated with the oxygen content variation. In situ dynamic observations revealed that the oxygen content was changed by the oxygen vacancies at the interface between LSTO and metal contact, which were driven inside the film to form the conductive channels during electrical biasing.

1.4.2 *In situ* TEM heating studies on VO_2

As discussed previously, *in situ* TEM heating technique provides an effective way to study the fundamentals of phase transition phenomena. However, the phase transition of VO_2 is accompanied with just a small amount of lattice change, which is

very difficult to be distinguished by TEM imaging. In contrast, the electron diffraction theory indicated that the monoclinic lattice has strong higher-order Laue zone (HOLZ) reflections of the electron beam, which results in secondary diffraction dots in the electron diffraction patterns. Therefore the M1 and R phase VO_2 could have distinguishable electron diffraction patterns. This theoretic prediction was supported by many experimental reports. As shown in Figure 1.20, the diffraction pattern taken from the M1 VO_2 [020] zone contained a lot secondary diffraction dots with weak intensity, which disappeared in the pattern taken from the same zone after phase transition [38].

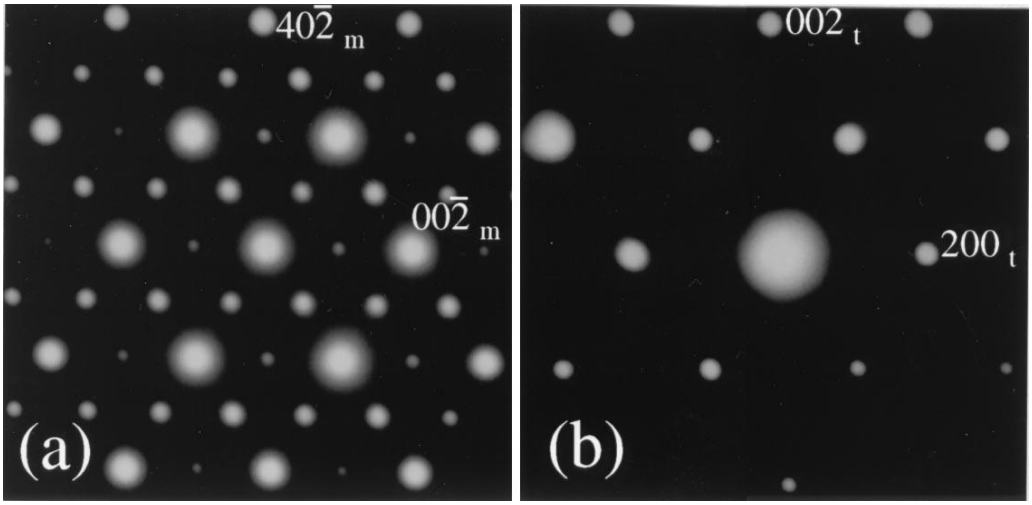

Figure 1.20 The electron diffraction patterns of (a) M1 phase and (b) R phase VO_2, taken from VO_2 [020] zone for both phases. Reprinted with permission from Elsevier [38].

Based on the electron diffraction, the SMT processes have been directly observed in both VO_2 thin films and nanowires. Yang et al. have fabricated VO_2 films with self-organized nano-pores by sol-gel methods [225]. The *in situ* TEM heating experiments then proved that the film matrix and the pore areas had simultaneous phase transition when heating to 70 ℃, which indicated the homogeneity of the films without dramatic strain or defect effects from the self-organized pores. Sohn et al. have synthesized VO_2 nanowires on *c*-cut sapphire substrates with [100] growth orientation [226]. The *in situ* TEM heating experiments showed that the nanowires experienced a direct M1 to R phase transition during heating. In comparison, they also synthesized free standing VO_2 nanowires along the same growth direction [227]. By *in situ* TEM heating, it was found that the free standing nanowires showed a M1 to M2 phase transition before tuned into R phase. These results indicated that the nanowires grown on the substrates contained less strain, while the free standing nanowires had large surface strain that led to the emergence of the intermediate M2 phase. Beteille *et al.* have fabricated free standing polycrystalline VO_2 thin films [38]. The *in situ* TEM heating study revealed that for the film with ~100 nm average grain size, each grain exhibited independent phase transition processes without any collective transformation through the film. However for the film with ~3-5 μm average grain size, the in situ experiments showed sudden and rapid modification in the large mono-oriented domains, suggesting a cooperative-like behavior during phase transition process.

More detailed *in situ* TEM heating investigations have revealed a lot of microstructural evolutions driven by VO_2 phase transitions. He *et al.* have conducted an

atomic resolution *in situ* TEM heating experiment on the VO_2 film grown on *c*-cut sapphire substrates [39]. The propagation of the M1-R phase domain wall was directly observed during phase transition. Domain walls were located in (202) and (040) planes of rutile structure. The phase transition of M1 VO_2 lattices beside the domain wall was identified with two steps: V-V pair movement followed with lattice expansion. Balakrishnan *et al.* have studied the thermal stability of the VO_2 thin film on Si_3N_4 membrane during phase transition [228]. The *in situ* TEM heating experiments showed that the VO_2 film cracked during the phase transition cycle. The cracks were found mainly along the grain boundaries, suggesting instability of the grain boundaries during VO_2 phase transition cycling. Furthermore, high density of twin structures was found to form beside the cracks, indicating a plastic deformation of the film before cracking. Viswanath *et al.* have investigated the microstructural evolution of the VO_2/Si cantilever structure during actuating process [229]. Strain was observed to propagate through the VO_2 film mainly by passing the grain boundary areas. It suggested the important effects of boundaries in the VO_2 films to accommodate the phase transition induced strain.

The previous research works of *in situ* TEM heating on VO_2 have already revealed a lot of fundamental information about the SMT process. Therefore it is believed that this technique will continue playing an important role in the future studies of VO_2.

1.4.3 *In situ* TEM mechanical and electrical measurements on VO_2

Despite of the great benefit of conducting *in situ* TEM mechanical and electrical

measurements on VO_2, not many research works have been reported yet. Especially, no works have been reported on the study of VO_2 thin films. In 2011, Guo *et al.* have conducted *in situ* TEM tensile tests on individual VO_2 nanowires [40]. The dynamic imaging and electron diffraction showed the M1–M2 structural phase transition arising from the central portion of the nanowire, as shown in Figure 1.21. A plateau was detected in the stress–strain curve at the point of M2 phase emergence. Further increase of the tensile stress led to the propagation of the one-dimensionally M2 domain with pinning and depinning of the domain walls along the nanowire. The M1 and M2 phase VO_2 were calculated with different Young's Modules. In 2013, the authors conducted combined *in situ* TEM heating and mechanical tests on VO_2 nanowires [41]. Focus electron beam was employed as the heating source while tensile loading was applied simultaneously. With a constant tensile displacement, the abrupt transition of VO_2 from M1 to M2 phase led to a drop of the tensile load, while the transition from M1 to R phase led to an increase of the load. These in situ TEM works revealed the fundamentals of VO_2 phase transition induced strain effects and provided a foundation for the VO_2 based mechanical devices.

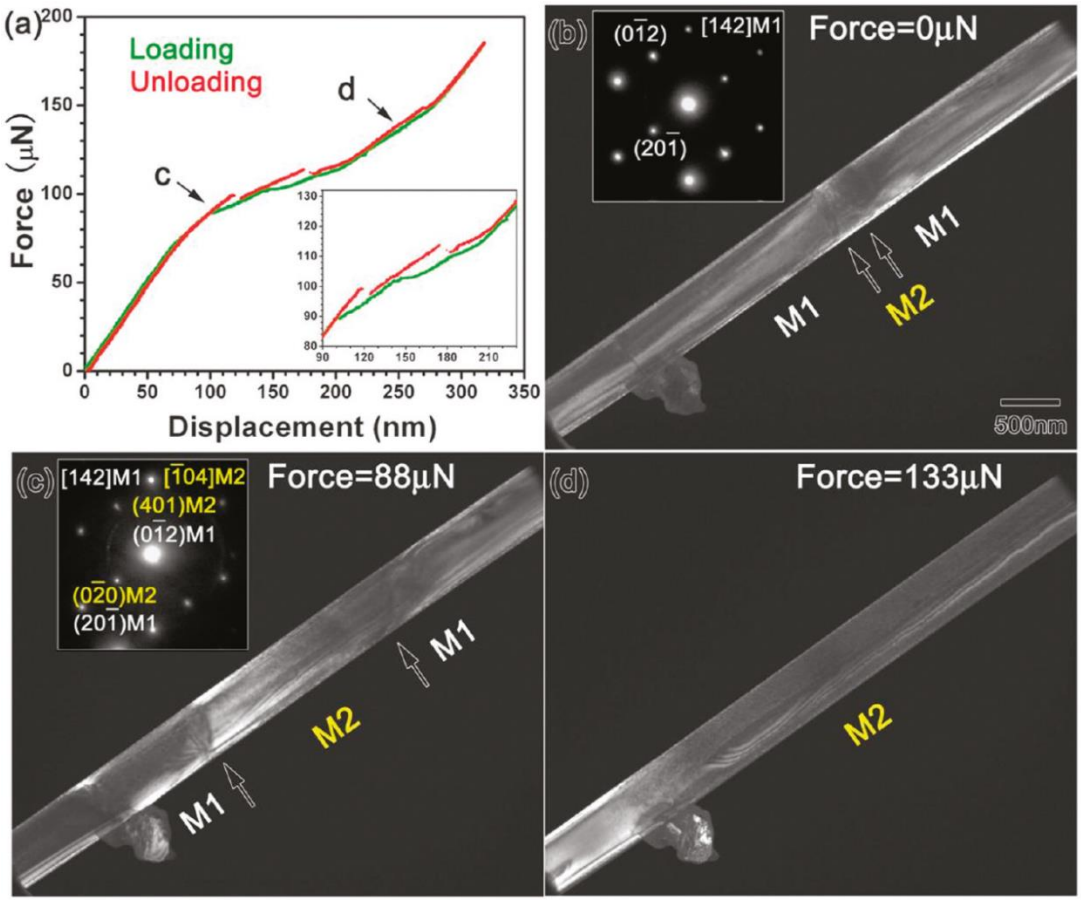

Figure 1.21 (a) Force-displacement plot of an *in situ* TEM tensile test on an individual VO_2 nanowire during loading (in green) and unloading (in red). (b) Dark field TEM images of the unstrained VO_2 nanowire. (c) Sample at loading of 88 μN and (d) sample at loading of 133 μN. Reprinted with permission from Americal Chemical Society [40].

In fact, the *in situ* TEM mechanical and electrical measurements have great potentials in VO_2 phase transition studies. With the *in situ* nanoindentations on VO_2 thin films, one can expect direct observations of VO_2 phase transitions under stress. The transition processes could be dependent on the growth orientations of the films. Furthermore, by combining the mechanical and electrical measurements together, the

resistivity of VO_2 thin films can be monitored together with the stress change, which provides the possibility to realize stress induced electrical switching of VO_2. In addition, by investigating the microstructural evolution during electrical bias, the mechanisms of field induced phase transitions and the memristor behaviors of VO_2 could be verified.

1.5 Challenges of the current research on VO_2 thin films

Despite of the great research efforts on VO_2 thin films, challenges still remain to be addressed for their future applications. For example, the VO_2 thin films are difficult to synthesize with high quality and performance on many of the low cost substrates, such as Si and glass, because of poor lattice matching relationship. In particular, the effort on the growth of high quality VO_2 thin films on glass substrates is to be explored. Chapter III of this dissertation focuses on achieving high performance VO_2 thin films on amorphous glass substrates [101]. In addition, the practical defect effects on the SMT properties of VO_2 thin films are still under investigation. Especially, the mechanisms of defects influence on VO_2 SMT properties are still under debate. As grain boundary is one of the most commonly existing defects in thin films, chapter IV of this dissertation is focused on investigating the role of grain boundaries in SMT processes [207]. Furthermore, increasing doping level in the VO_2 films was usually accompanied with a significant drop of SMT properties. Therefore it is desired to explore other methods of T_c tuning with the other SMT properties retained. Chapter V focuses on exploring continuous T_c tuning of the VO_2 thin films with the maintenance of other SMT properties. Moreover, *in situ* TEM studies of VO_2 studies could be powerful in

addressing the fundamental mechanisms that could not be addressed easily by *ex situ* property measurements. Chapter VI of this dissertation focuses on investigating the stability of the VO_2 SMT properties during multiple thermal cycles by the *in situ* TEM heating technique.

CHAPTER II

RESEARCH METHODOLOGY

2.1 Pulsed laser deposition system

In the past 30 years, the pulsed laser deposition (PLD) technique has developed significantly and became a widely used technique for thin film growth of various kinds of materials. The laser assisted thin film deposition technique was initially carried out in 1960s, and then demonstrated on the depositions of $YBa_2Cu_3O_7$ by Dijkkamp and Venkatesan in 1987 [230]. The PLD belongs to the physical vapor deposition (PVD), which refers to thin film deposition methods with the vaporized materials containing many species such as electrons, ions, atoms, molecules, clusters and particulates from the target condensing onto various substrates in a vacuum chamber. The PLD technique is relatively simpler than many other PVD techniques. It mainly consists of the pulsed laser system and the vacuum chamber. Once the pulsed laser strikes the target material, the evaporated materials from the target can fly through the vacuum chamber and deposit on the surface of the substrate.

A typical schematic of the PLD system is shown in Figure 2.1. In this chamber, multiple target holders are located face to face with the substrate holder. The targets are rotatable and oriented at an angle of 45 ^{o} to the incident direction of the excimer laser beam. The chamber vacuum is maintained at ~10^{-7} Torr by two-stage vacuum system with roughing pump and turbomolecular pump. Most of PLD systems use excimer gas to generate laser beam. The laser wavelength ranges between 200nm and 400nm (KrF: λ=248 nm, ArF: λ=193 nm, Nd:YAG: λ=355 nm). Optical components including mirrors

and lenses are placed between the laser and the vacuum chamber to change the incident beam direction and the focus point. Once a high power laser shots the target through the optical focusing lens, it can generate the heat energy to vaporize the target materials. The laser power density is usually varied from 3 J/cm^2 to 5 J/cm^2 by adjusting the laser output energy and the focusing lens. The distance between the target and substrate is usually maintained at approximately 3-5 cm for best film quality. During depositions, the substrate temperature can be changeable in the range from room temperature to 800 ℃. The precisely temperature control and sequential ramping can be achieved with computer controlled feedback loops of thermal couple and heater.

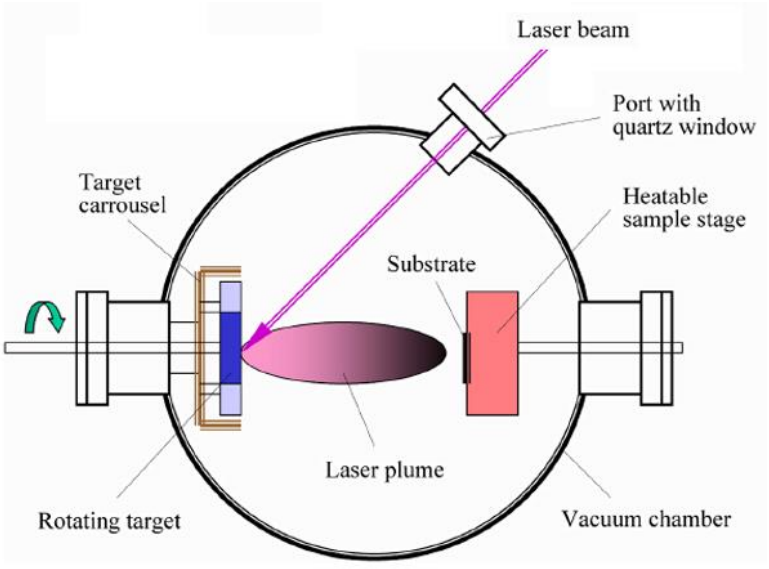

Figure 2.1 Schematic diagram of the PLD system.

The quality of the deposited thin films can be affected by several parameters including laser repetition rate, substrate temperature, laser energy density, distance between the target and substrate, and the partial gas pressure of the chamber. Especially, interaction between the laser and target plays an important role in the film deposition. With the interaction, the incidence laser creates a plume towards the substrate holder. The plume contains many different species such as atoms, molecules, electrons, ions, clusters, particulates and molten globules by means of photon interaction. During the interaction, the laser energy first converts to electronic and then into thermal excitations. After that, chemical and mechanical energies result in evaporation, ablation, plasma formation and even exfoliation. The plume then flies through a short distance across the vacuum chamber and high energy molecules ejected from the target are deposited on the substrate as adatoms. Thin films are then synthesized through the solidification process. Elevated substrate temperature is desired during the deposition process to provide enough kinetic energy for the adatoms to diffuse through the surface to preferred lattice sites.

The PLD physical principles have been described by R. K. Singh and J. Narayan in 1990 [231]. The interaction process can be explained with three different steps: laser-target interaction, interaction of laser beam with evaporated material, and adiabatic plasma expansion. The first two steps happen at the initial stage of the laser radiation and through the laser pulse duration (about 25 ns duration). The last step happens right after the laser pulse stops.

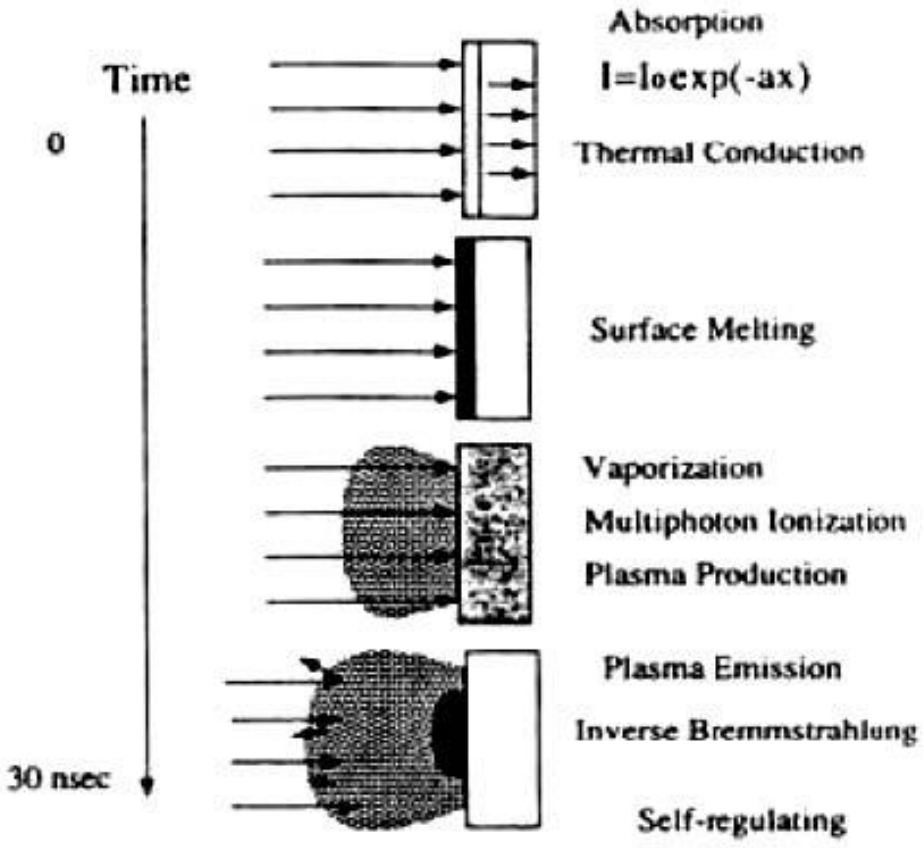

Figure 2.2 Schematic diagrams illustrating different steps of laser target interactions during laser pulse along time variation [231].

Figure 2.2 shows the laser-target interaction during the pulsed laser period. During the laser-target interaction, the laser beam with intensity of I_0*exp(-α) can be absorbed by the target within the depth of x. Then the electromagnetic energy in the laser pulse is transferred to different energy types such as the thermal energy, which can melt and evaporate the materials from the target surface. The heating, melting and evaporation rate of a laser pulse is usually dependent on the parameters of the laser beam

and properties of the target materials. The laser parameters include the laser energy density, pulse duration, laser wavelength and the shape of the laser pulse. The material properties refer to the optical reflectivity, absorption rate, heat capacity, thermal conductivity, and material density, etc. These factors eventually define the heat flow through the target. Considering a one dimensional heat flow, it can be described by the following equation:

$$\rho_i(T)c_p(T)\frac{\partial T(x,t)}{\partial t} = \frac{\partial}{\partial t}\left[K_i(T)\frac{\partial T(x,t)}{\partial x}\right] + I_0(t)[1-R(T)]e^{-a(T)x} \qquad (2.1)$$

where x is the distance normal to the surface of the target and t is the time. $\rho_i(T)$ is the target density, $c_p(T)$ is thermal heat capacity, $R(t)$ is the optical reflectivity, $a(T)$ is the absorption coefficient, $I_0(t)$ is the intensity of the incident laser, and $K_i(T)$ is the thermal conductivity. The subscript i indicates the phase, which stands for solid when $i = 1$ and for liquid when $i = 2$.

The high power of the pulsed laser beam irradiated on target surface could cause a temperature higher than 2000 K, leading to the melting of the target material. Thus the position of the target surface is changeable. Based on the energy balance approach, it is possible to calculate the amount of the evaporated material by the laser pulse which can be considered similar to the amount of the energy needed for the film deposition without any energy loss. The balance equation can be expressed as:

$$\Delta x_i = \frac{(1-R)(E-E_{th})}{(\Delta H + C_v \Delta T)} \qquad (2.2)$$

where Δx_i is the thickness change amount of the target after evaporation, R is the reflectivity, ΔH is the amount of the heat absorbed by unit mass, Cv is the heat capacity under constant volume, and ΔT is the change of the temperature. The threshold energy,

E_{th}, refers to the minimum energy required for the evaporation. This equation is suitable for the case of the absorption length shorter than the thermal diffusion length in the target material.

After the materials evaporate from the target, further interactions between these evaporated species and the laser been can be expected on the way of the laser path. As the laser-target interaction surface temperature can as high as 2000K, positive ions and electrons can be emitted from the surface. These emissions can be estimated by the Langmuir-Saha equation:

$$\frac{i_+}{i_0} = \frac{g_+}{g_0} e^{[(\phi - I)KT]} \tag{2.3}$$

where i_+ and i_0 are the fluxes of positive and neutral ions emitted from the target surface at the temperature of T. g_+ and g_0 are the weights of the ions on the ionic and neutral states. ϕ is the work function of the electron, and I is the material ionization potential. Based on the equation, when I is larger than ϕ, the flux of the neutral ions will exponentially increase with the increase of temperature.

The target surface will continually absorb energy from laser radiation since the outer edge of the plasma regime is transparent to the laser beam. Figure 2.3 shows a schematic diagram of the interaction of laser beam with the target surface. It consists of four different regions: the unaffected bulk target (A), the evaporating target surface (B), the area adjacent to the surface which absorbs laser beam energy (C), and the rapidly expanding outer edge which is transparent to the laser beam (D).

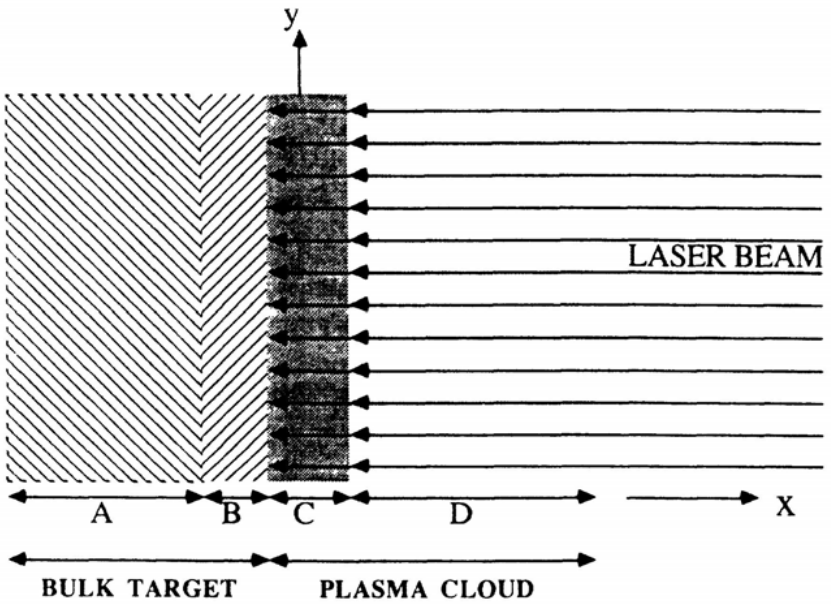

Figure 2.3 Schematic diagram shows the different phases presented during the laser target interaction [231].

After the plasma formation and expansion, the adiabatic expansion of the plasma in vacuum chamber gives rise to the laser deposition process. In this step, the thermal energy is converted to kinetic energy of the plasma. Under adiabatic condition, anisotropic expansion of the plasma plume can be enhanced, which can be described by the relation shown below:

$$T[X(t)Y(t)Z(t)]\gamma^{-1} = const \tag{2.4}$$

where γ is the ratio of the specific heat capacities at constant pressure and volume. During the adiabatic step, the conversion of the thermal energy into the kinetic energy can lead to high velocity of the plasma expansion. Thus the plasma, which initially has

larger dimension along *X* and *Y* than *Z* direction, can expand along the *Z* direction with increase of the velocity. The last stage of PLD is the deposition of the ablated materials onto substrate surface. As the ejected species by laser-target interaction have high kinetic energies, they may cause the sputtering of the substrate surface atoms, which could have collisions with the following incident flux flow. A thermal equilibrium condition can be reached for the film growth when the condensation rate is higher than that of the flux.

In the works of this dissertation, PLD was used for all the thin film syntheses. The targets were prepared by a standard solid-state reaction method. High purity commercial V_2O_5 powders were used as the target source of the VO_2 films. The mixed powders of Al_2O_3 and ZnO with the ratio of 5 wt.% were used as the material source of the Al-doped ZnO (AZO) depositions. The target powders were mixed and pressed into pellets. The pressed V_2O_5 pellets were sintered at 650 ℃ for 6 hours in a tube furnace exposed to atmosphere, while the AZO pellets were sintered at 1100 ℃ for 6 hours. The amorphous lime-soda glass, *c*-cut sapphire, and Si (001) single crystal substrates were used for the thin film depositions

Depending on the growth parameters and the intrinsic properties of the substrates and thin films, the thin films growth can be described by three major modes: Volmer-Weber island growth, Frank-Van der Merwe layer-by-layer growth, and Stranski-Krastanov layer + island growth, as illustrated in Figure 2.4 [232]. In the island growth mode, adatoms and molecules nucleate onto substrate surface to form clusters, which result in growth into 3-D islands. The driving force of the island growth is the stronger bonding between deposited atoms compared with the bonding between adatom

and the substrate. In the layer-by-layer growth mode, adatoms tend to form small nuclei to grow into 2-D planar structures because of the stronger bonding to the substrate atoms. The layer + island growth mode is a combination of both the layer-by-layer and island growth [233]. In this mode, Volmer-Weber island growth begins after formation of several atomic monolayers in a layer-by-layer growth due to the energetically instability during the film growth.

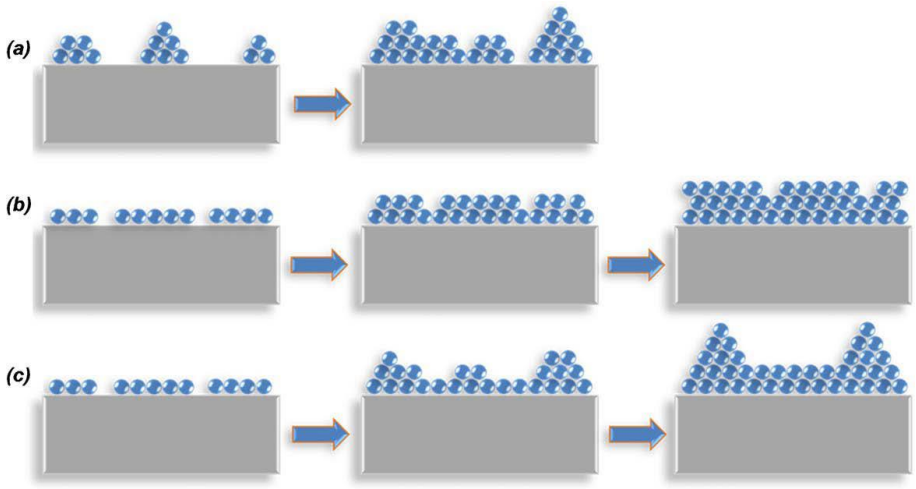

Figure 2.4 Illustrations of the heteroepitaxial growth modes: (a) Volmer-Weber Island growth, (b) Frank-Van Merwe layer-by-layer and (c) Stranski-Krastanov layer + island growth. Reprinted with permission from Elsevier [232].

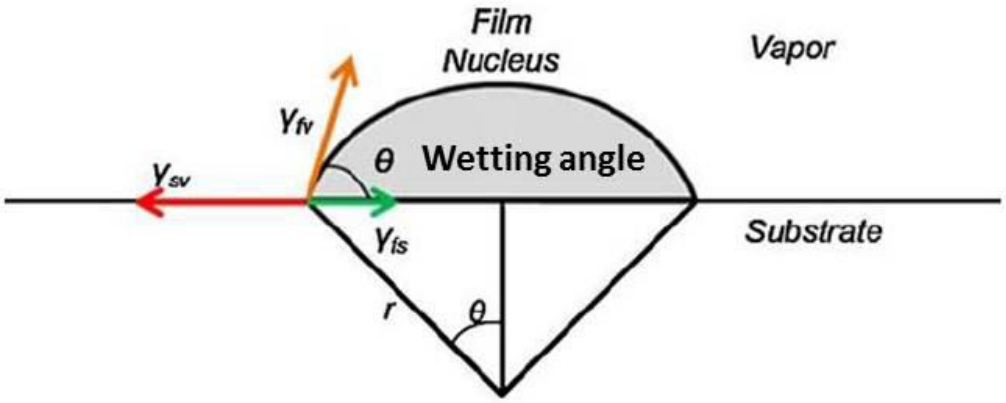

Figure 2.5 Surface energy model of the nucleation process during a thin film vapor deposition process [232].

The bonding energy difference can be illustrated by the surface energy. Thus the growth modes of the thin films can also be described by the thermodynamic models for nucleation process. Figure 2.5 illustrates the surface energy model that describes the nucleation process [232]. The equilibrium between the horizontal components of the interfacial tensions between substrate, film and vapor phases is expressed by the following equation:

$$\gamma_{sv} = \gamma_{fs} + \gamma_{fv} cos\theta \tag{2.5}$$

where γ is the interfacial energy and θ is the wetting angle. The subscripts *s*, *v*, and *f* represent the substrate, vapor and film, respectively. The three growth modes mentioned above can then be identified by this equation according to the wetting angle. In the island growth mode, the θ has a positive value while the surface energy of the film is

higher than that of the substrate. In the layer-by-layer growth, the surface energies of the film and substrate are similar and the film wets the substrate with $\theta \sim 0$. Despite of the reliability of this ideal model, a lot of other factors could influence the growth of the films in practical. There are different kinds of nucleation sites including step edges and defects during the film growth and the growth of nuclei can be disrupted beyond the critical nucleus size. Besides, the thin film growth is also affected by the growth dynamic which is influenced by the growth parameters such as the laser energy and repetition rate. Therefore in the series of works in this dissertation, many growth parameters were varied and optimized to get the films with controlled microstructures and qualities.

In order to get the monoclinic phase VO_2, the oxygen partial pressure was optimized as 10 mTorr for all the VO_2 depositions. The laser beam was focused to obtain an energy density of approximately 3 J/cm^2. The substrate temperatures, laser repetition rates and deposition durations were varied to obtain the films on different substrates, with different grain sizes and different thicknesses. The AZO depositions were conducted at the substrate temperature of 750 ℃ and laser repetition rate of 2 Hz. The oxygen partial pressures were varied to obtain the AZO layers with different surface roughness.

2.2 X-ray diffraction (XRD) characterizations

X-ray diffraction (XRD) is one of the most widely used nondestructive analysis techniques for exploring the lattice constant, orientation and internal stress of the crystal

materials. Especially, application for the thin film materials can help to identify the film crystallinity and the strain effects between the film and substrate. Figure 2.6 shows the schematic set up of an X-ray spectrometer [234]. During operations, the incident direction of the x-ray beam is orthogonal to the surface of the reflecting plane. In this set up, once the incident beam is diffracted by the plane surface, the diffracted beam can be measured by the detector D, which is rotated with a certain angle respect to sample position C. The incident X-ray beam will be diffracted into specific directions by a crystal structure. According to the angles and the intensities of the diffracted beams, the three dimensional structure of the crystal can be identified. X-ray diffraction is governed by the Bragg's Law:

$$n\lambda = 2d\ \sin\theta \tag{2.6}$$

where λ is the wavelength of the X-ray, d is the lattice plane spacing (d-spacing), and θ is the diffraction angle. The schematic of the Bragg's Law is shown in Figure 2.7 [235].

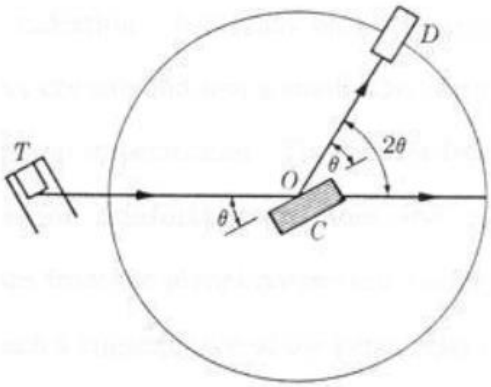

Figure 2.6 Schematic diagram of X-ray spectrometer [234].

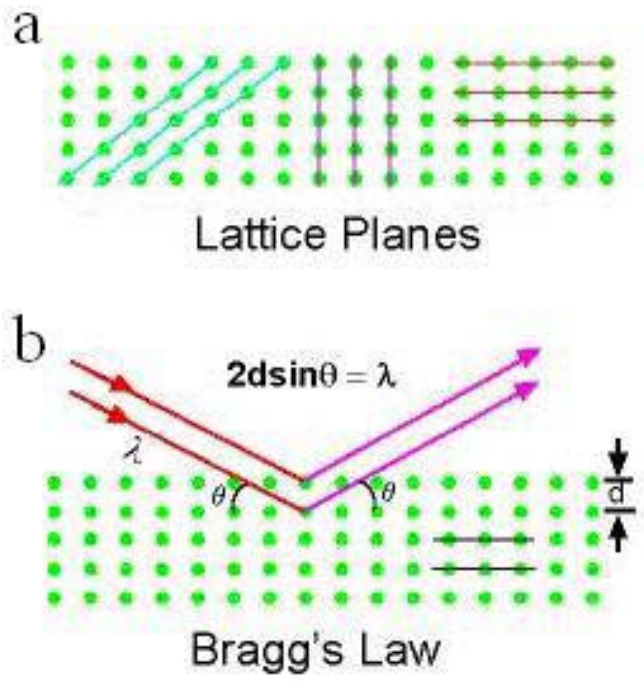

Figure 2.7 (a) A two dimensional periodic array of atoms forming different planes in the crystal, (b) Bragg diffraction of a set of planes with inter-plane spacing of *d*,which is conditioned to Bragg's Law [235].

The Bragg's Law conditions can only be satisfied by certain combinations of the θ angles and *d*-spacing. The plot of the intensities of the diffracted beams versus the angle of 2θ is called θ-2θ scan. The θ-2θ scan is the characteristic XRD pattern in which the incident beam and detectors rotate simultaneously to form an angle 2θ. Based on the peak positions of the θ-2θ scan, the crystal structure of the material can be characterized. In addition, the width of the intensity peak can be essential to determine the crystallinity of the material.

The width of the θ-2θ scan peaks is affected by several factors. First of all, due to the wave destructive interference resulted from periodicity of atomic arrangement, the width of the diffraction peak could increase with the reduction of crystal size. Figure 2.8 shows the effect of the crystal size on the width of the peak [234]. Based on this diagram, the size of the crystal can be estimated by the following formula:

$$t = \frac{k\lambda}{B\ cos\theta_B} \tag{2.7}$$

where λ is the wavelength of the X-ray beam (1.5418 Å for Cu K_α), B is the full width at half maximum (FWHM) of the peak, and θ_B is the highest intensity position of the peak. The constant k depends on the morphologies of the crystals. The value of 0.9 is usually used for thin film samples.

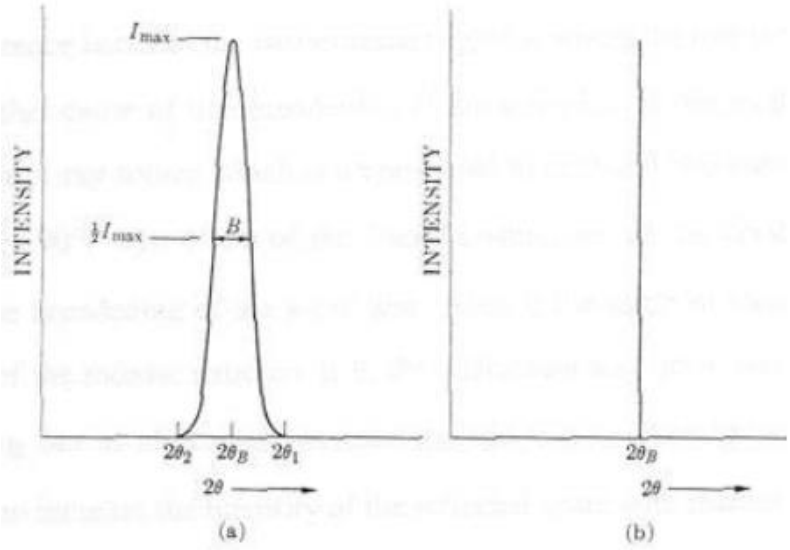

Figure 2.8 The crystal size effects on the XRD θ-2θ spectra peak width [234].

Another possible reason for the variance of the peak width is the relationship between the spectral width of the x-ray source and diffracted angle θ. The term of "spectral width" refers to the wavelength width of the output beam. Such wavelength width from the source is proportional to $\tan\theta$. Thus when the θ is close to 90°, the increase of the peak width can be caused by misorientation of the grain crystal structures of a material. For instance, for the columnar grain structures commonly observed in thin films, if the angle of the misorientation between the columns is defined as $\pm\varepsilon$, the diffracted peak at θ for the single crystal will be broadened up to $\theta \pm \varepsilon$. Besides of the peak width, the intensity of the peak will also be affected by the grain structured crystal. When the material has poor crystallinity, the atomic arrangement is irregular, and the constructive and destructive interference won't happen due to the random phase. The intensity of the X-ray beam can be estimated by the summary of all the X-ray intensities scattered. For the well-oriented crystals, the diffracted beam obeys the Bragg's Law. Thus the intensity of the beam can be formulated as N^2A^2, where N is the number of scattered rays and A is amplitude of the rays. In contrast, the intensity of the diffracted beam with scattering can be formulated as NA^2. Therefore, the material with higher crystallinity can have higher intensity of the X-ray diffraction than that with lower crystallinity.

2.3 Transmission electron microscopy (TEM) characterizations

Transmission electron microscopy (TEM) is a powerful and widely used tool for microstructure characterizations. TEM is developed to overcome the limitation of optical

microscopes depending on the wavelength of visible light. It has the capability to identify the internal structure underneath the surface while the electrons transmit through the TEM specimens, which makes this system distinguishable with other microscopes. Additionally, the TEM can provide projection of microstructures in atomic level, which give fundamental and comprehensive understandings of the material systems. For the applications on thin films, although large portion of the film quality analysis still highly relies on surface analysis tools such as atomic force microscopy (AFM) and scanning electron microscopy (SEM), the analysis ability on the internal and small size microstructures along with the cross-section and plan-view is entitled by TEM technique. The TEM investigations on thin films have already provided clear evidences of strain coupling, defects formation, interfacial reaction and surface diffusion etc. Furthermore, within such remarkable system, other analytical techniques including STEM, EELS, and EDX have been combined together, which make this system even more powerful to characterize the integrating chemical compositions of the materials within single atomic scale.

Figure 2.9 shows a typical TEM system set up [236]. It mainly contains four parts: the electron source, electromagnetic lens system, sample stage and imaging systems. They are all combined in a vacuum column backed up by the mechanical pump and turbo pump or diffusion pump [236]. There are different types of electron guns, including thermal emission guns and field emission guns, in which the cathodes emit electrons when heated and by high voltage, respectively. The electron beam is then accelerated towards the anode by the extraction voltage. The high energy electron beam

is focused and confined by the condenser lens and apertures before reaching the specimen. The objective lenses then focus the transmitted beam after passing through the specimen and project the image on the phosphorescent screen and CCD camera. In this dissertation, JEOL JEM-2010 (200 kV, LaB_6 filament) and Tecnai F20 super-twin (200 kV, ZrO2/W Schottky field emitter) were used for the TEM characterizations. They have the point-to-point resolution of 0.23 and 0.24 nm respectively.

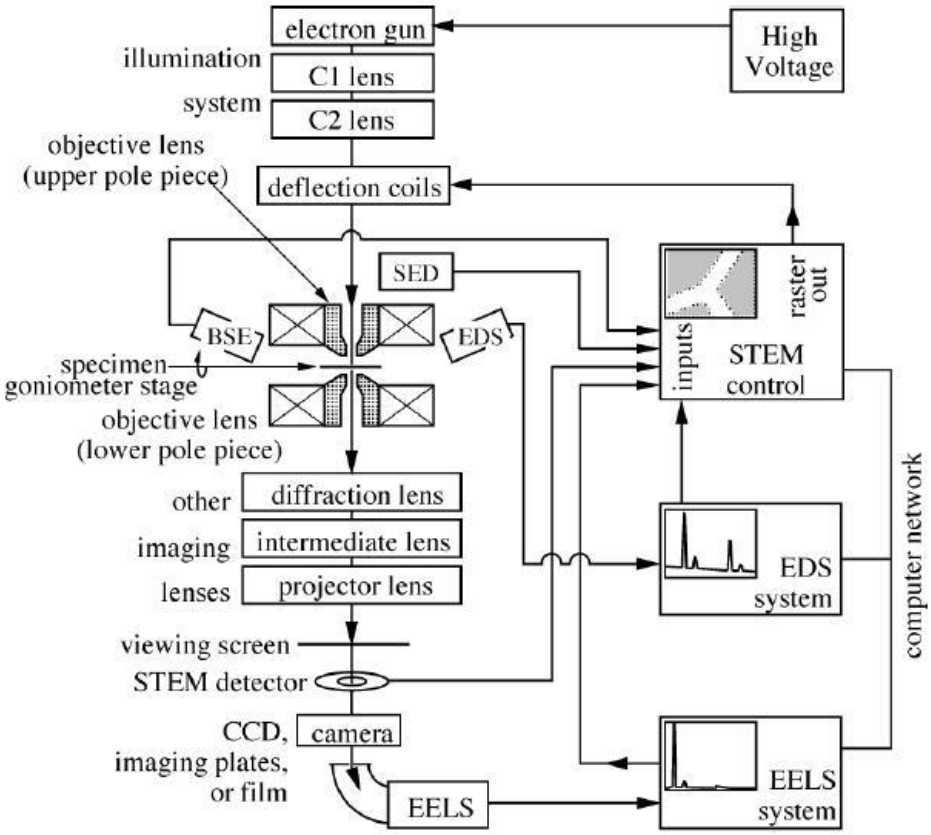

Figure 2.9 The block diagram of a typical TEM system set up with analytical capabilities [236].

2.3.1 Resolution

Resolution and magnification are two of the main parameters of TEM. The magnification can easily be adjusted by changing the acceleration voltage and the magnetic field of the lens. However, the resolution is affected by a lot of factors. Without considering the aberration effects, the resolution limit of the microscope can be theoretically estimated by the wavelength of the electrons and the aperture angle of focus lens, which can be expressed based on Rayleigh criterion:

$$r = \frac{0.612\lambda}{n\ sin\alpha} \tag{2.8}$$

where λ is the wavelength of the electrons, n is the refractive index (n = 1 for vacuum) and α is the aperture angle of the lens. Generally, in order to generate more coherent beam, the electrons are accelerated by high voltage in the TEM. Thus the wavelength of the electron beam is usually shortened in the order of 0.01 Å, which contributes to a high resolution of the microscope.

Besides of the electron wavelength limitation, the aberrations of the lens have significant influence on the resolution. The aberrations are including spherical aberrations, chromatic aberrations and astigmatisms. The spherical aberration is mainly caused by more refraction of the incident electron beam when passing through the edge portion of the lens compared to passing through the central portion, as shown in Figure 2.10(a) [237]. Because of the spherical aberration, when the electron beam through the lens center is focused on the image plane, the beam near the lens edge will be focused before the plane. As a result, the spherical aberration disk with radius r_s will be made with relation of $r_s = C_s\beta^3$, where Cs is the spherical aberration coefficient and β is the

angular aperture of the lens.

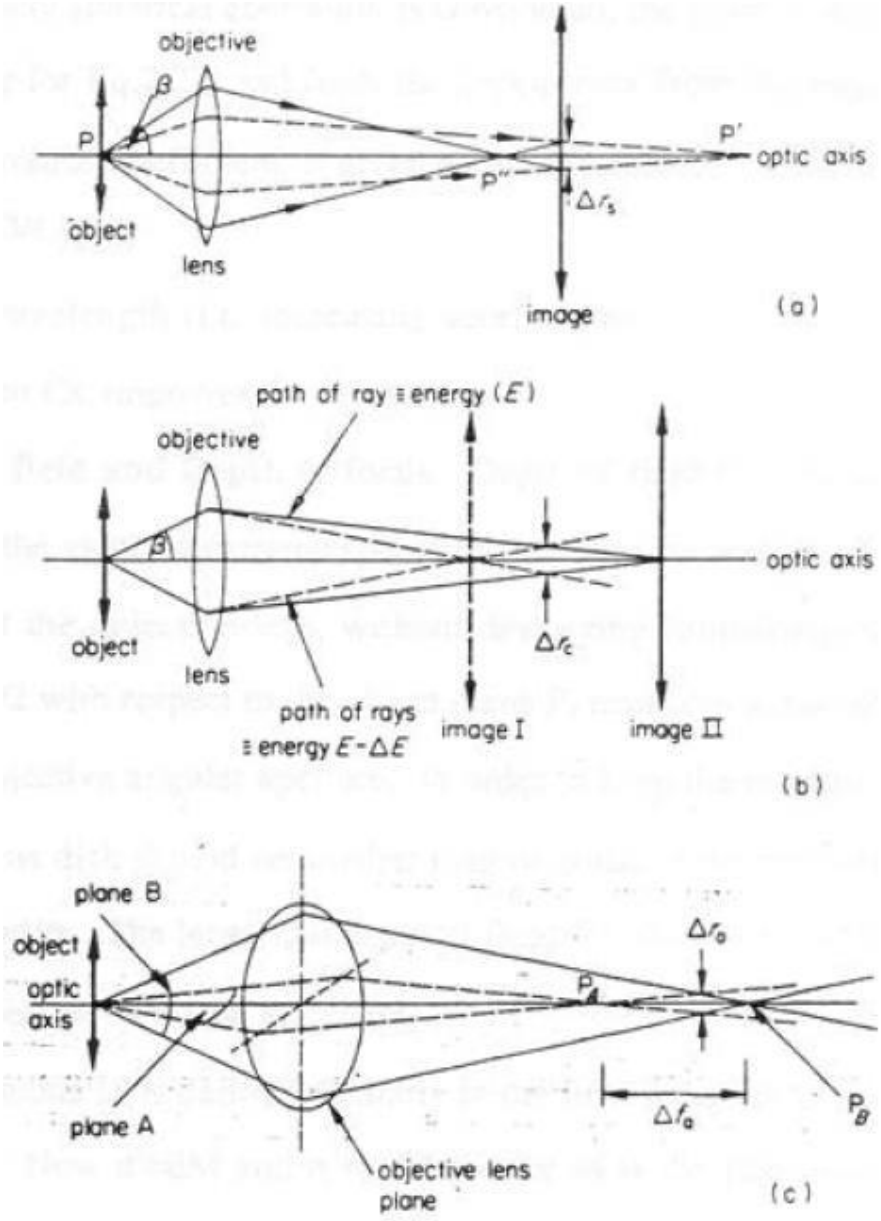

Figure 2.10 Electron beam diagrams of the objective lens aberrations: (a) spherical, (b) chromatic and (c) astigmatism [237].

Chromatic aberration is another kind of aberration which is occurred by the energy dispersion (ΔE) of the incident electrons. The focus lens using magnetic field has different refraction capabilities for the electrons with different energies. The electrons with higher energy, and thus higher velocity, are expected to have lower refraction angles through the magnetic lens. Therefore, the focal lengths between the dispersed electrons can be different, as shown in Figure 2.10(b). The chromatic aberration can be even worse with the increase of the TEM specimen thickness. Thus preparations of thin enough specimens are desired to improve the resolution.

Astigmatism is another factor to affect the resolution. The astigmatism usually comes from non-uniform magnetic field which results in different focal length in different directions, as shown in Figure 2.10(c). This can be caused by the vibration of the electromagnetic field due to non-uniform surface of cylindrical pole-pieces, and the contamination charging up the electron beam. The projected TEM image with different focus length can be deformed with radius r_{ast} as shown below:

$$r_{ast} = \beta \Delta f \tag{2.9}$$

Where β is the astigmatism coefficient and Δf is the maximum difference in focal length induced by astigmatism. The astigmatism can be corrected by changing the amplitude and orientation of the magnetic field on the lens to compensate the field vibrations.

2.3.2 Depth of field and depth of focus

When the electron beam has a spatial width, the lens will refract the beam to focus at multiple positions. The vertical distance between points at which the beam crosses over

along the central axis on objective plane is called the depth of field (D), as shown in Figure 2.11 [238]. As the angle β is small, the value of D can be calculated by the following equation:

$$\mathrm{D} = \frac{d_1}{\beta} \tag{2.10}$$

Similarly, the depth of focus (D') is defined on image plane as the vertical distance between points at which beam crosses over along the central axis. D' can be calculated by the equation:

$$\mathrm{D}' = \frac{d_1}{\beta}\left(\frac{d_1}{d_2}\right)^2 = \frac{d_1}{\beta}\left(\frac{\beta}{\alpha}\right)^2 \tag{1}$$

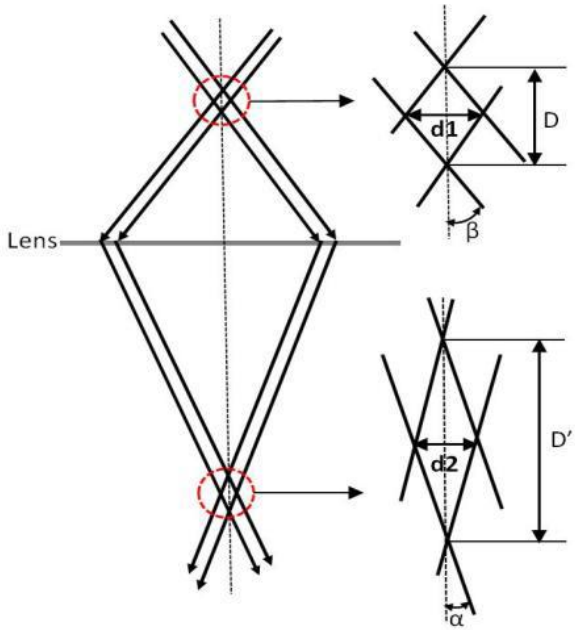

Figure 2.11 Schematic diagrams of the depth of field and depth of focus [238].

It can be noticed that by selecting smaller size of aperture, the angle β will decrease, which will contribute to the increase of the depth of field (D) and depth of focus (D'). For instance, when d_1 = 1 Å and β = 5×10^{-3} radius, the depth of the focus is 20 nm. It means any region of the specimen with a thickness less than 20 nm can be focused. Therefore, preparations of thin specimens are desired to have broader range of the D and D'.

2.3.3 Image and diffraction modes

When the coherent electron beam transmits through the specimen, it can be dispersed and refocused on the image plane by the objective lens, which generates the image of the specimen. In contrast, the beam dispersed and refocused on the back focal plane can generate the diffraction patterns. In this mode, the beam coming through the specimen will travel through the selected area diffraction (SAD) path, as shown in diagram in Figure 2.12(a) [239]. In this path, the size of the beam gets smaller with the change of the focal length of the intermediate lens. And the selected area diffraction (SAD) aperture is inserted in the image plane. Then the diffraction pattern is projected on the viewing screen.

The generation of the electron diffraction is related with two features. First, as the wavelength of the electron beam is much smaller than the lattice distance, the diffraction angle will be very small. Then Bragg's law defined as $n\lambda = 2d\sin\theta$ becomes $n\lambda = 2d \cdot \theta$ with θ < 0.5 °. Second, as the specimen is very thin, the projected diffraction will be in the rod form of the domain. The Ewald reflection sphere can then

overlap with the diffraction domain for active state of hkl reflection. Based on the relationship of the reflection indices, $hu + kv + lw = 0$, the reflection on the (hkl) planes will have the beam incident direction of [uvw] along the zone axis. Therefore the reciprocal plane (uvw) in the diffraction pattern includes the lattice point hkl.

In the image mode, as shown in Figure 2.12(b), the objective lens is inserted in the image plane of the objective lens and the focus length of the intermediate lens is adjusted to project the image on the viewing screen. In this mode, dark field (DF) and bright field (BF) images can be obtained depending on the objective aperture configuration and the beam diffraction as shown in Figure 2.13 [239]. BF image is formed when the aperture is positioned to allow the direct transmitted electrons to pass, while DF image is formed when the aperture is positioned to allow only certain diffracted electrons to pass. The DF image can also be obtained through a tilted incident beam, as shown in Figure 2.13(c). In the dark field mode, as the filtered beam just contains the information from certain diffraction planes, only the areas along such orientations in the specimen will be imaged (shown as bright on the screen). All the other areas will show in dark contrast on the screen.

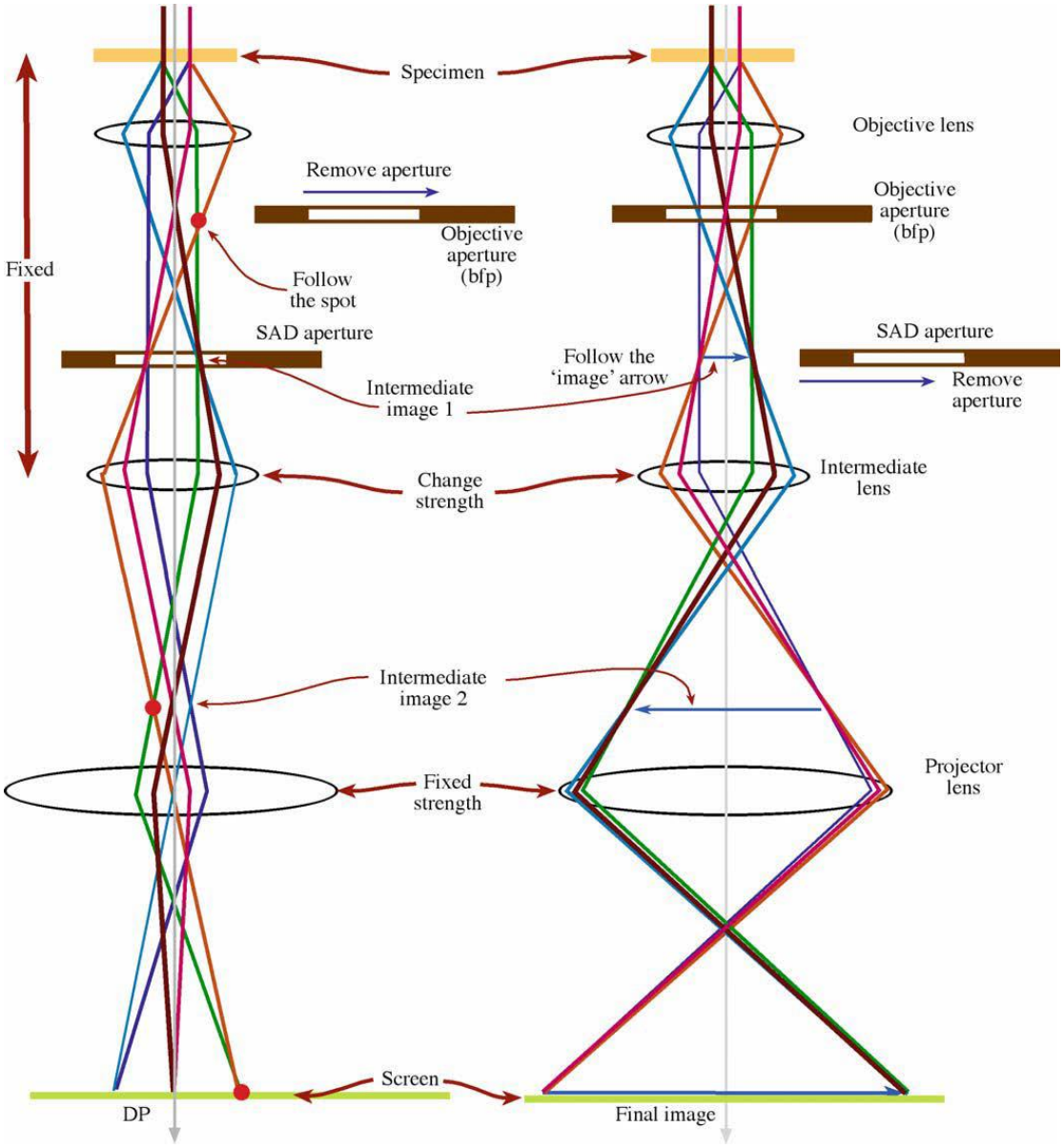

Figure 2.12 The electron beam paths of two basic operation modes of TEM: (a) the diffraction mode and (b) the imaging mode [239].

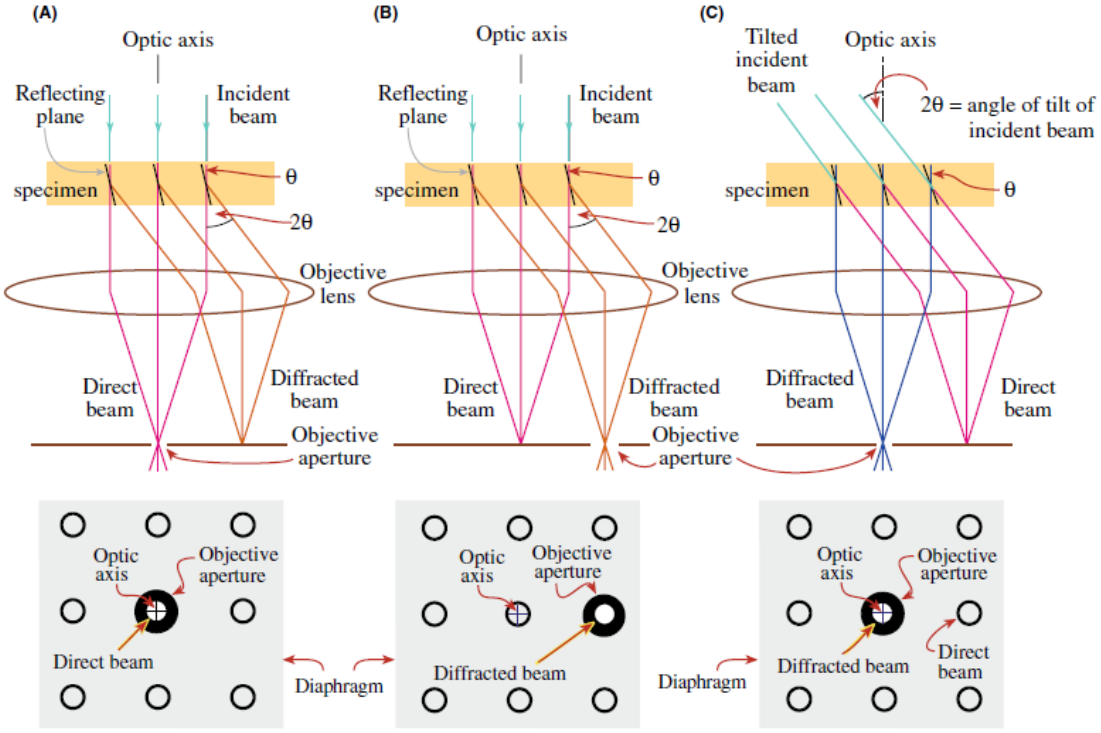

Figure 2.13 Diagrams of the objective lens and objective aperture coordinated production of (a) a BF image formed from the direct electron beam, (b) a displaced-aperture DF image formed by a certain orientation diffraction beam, and (c) a DF image formed by the tilted incident beam, which scatters certain diffraction beam to the optic axis [239].

2.3.4 TEM specimen preparations

As discussed in previous sections, the TEM specimen preparation is essential to obtain high quality TEM images. Typically, the region transparent to electrons should have the thickness less than 100nm. The preparation method depends on the material properties and objective. In this dissertation, both the cross-section and plan-view samples were prepared by conventional grinding, polishing, dimpling and ion milling

steps. First, the sample (substrate and film) is cut into thin slices by diamond pen. For cross-section samples, two slices are glued together. Second, the cut and glued samples are pre-thinned by sand papers and polished by diamond papers. Third, the thinned samples (usually less than 100μm) are then dimpled and polished by a copper wheel and leather wheel on a dimple machine. Finally, the dimpled samples are put into a precision ion polishing system (PIPS) for ion milling. The ion milling can bombard and thin the specimen to get a thin area (< 100 nm) surrounding the ion milling holes. Depend on the film and substrate materials and specimen types, various factors of ion milling can be adjusted, including beam energy, beam incident angles, and beam modulations. Generally, shorter ion milling duration is preferred to reduce the ion damages on the specimen.

2.4 Electrical properties measurements

In this dissertation, the phase transition properties of the VO_2 thin films were characterized by the electrical resistance switches with temperature variations, which were measured by a Physics Property Measurement System (PPMS) (EverCool, Quantum Design, Inc). The PPMS provides a flexible and automatic platform that can perform a variety of experiments with precise thermal control including magnetization and resistivity vs. temperature measurements (R-T). The PPMS has a capacity to apply magnetic fields up to ±9 Tesla and a temperature range of 1.9 ~ 400 K using liquid He and heater. The temperature sweep rate can be varied from 0.01 K/min to 12 K/min.

The DC transport measurements in PPMS incorporate a high precision current

source and a voltmeter in the Model 6000 control unit. The R-T option supports the four-terminal probe measurements. These measurements are typically conducted by introducing a known current through the sample from two electrodes, and measuring the voltage across the sample direction from another two electrodes. The sample resistivity is then calculated according to the Ohm's law and the sample dimension. The electrodes on the samples for the measurements were Au contacts deposited by a magnetron sputtering system.

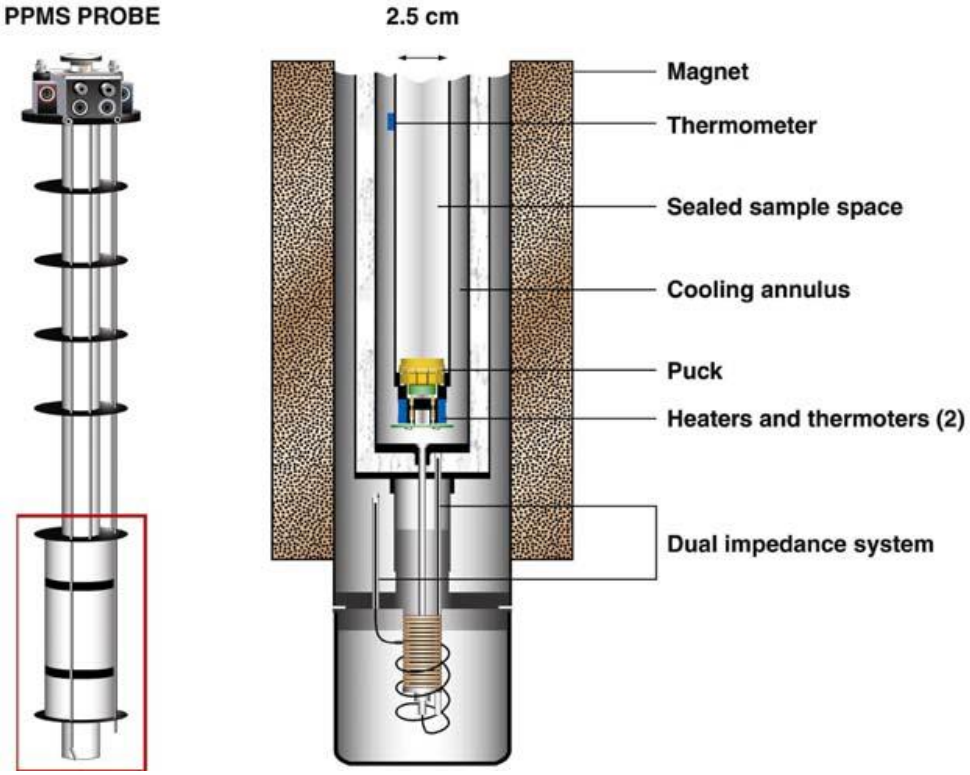

Figure 2.14 Schematics of the sample rod and puck setup in the dewar of PPMS for electrical measurements.

Figure 2.14 shows the sample rod used for the R-T measurements in PPMS. The sample is mounted on easily removable printed circuit boards as show in Figure 2.15. This DC Resistivity Standard puck has three channels, which can measure up to three samples at one time. For the VO_2 thin films, the R-T plot can be measured within the DC puck. And the phase transition properties, i.e. transition temperature, amplitude, sharpness, and width of thermal hysteresis, can then be characterized by the resistivity changing rate with temperature.

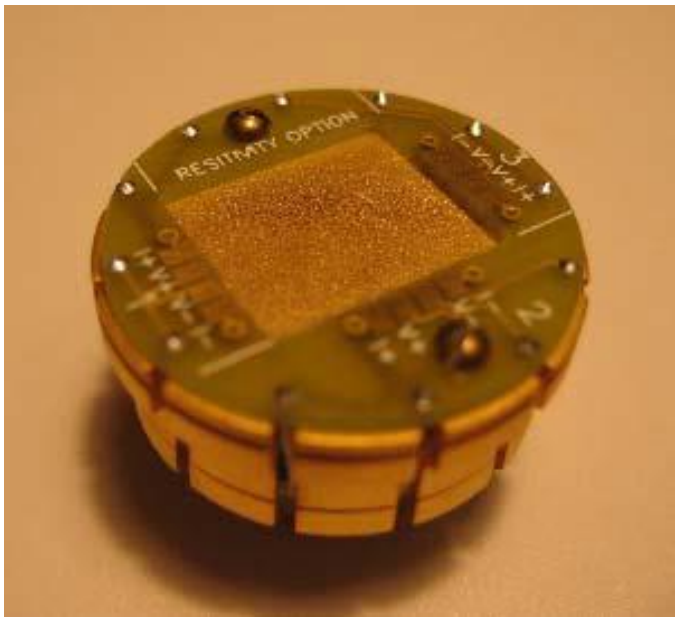

Figure 2.15 Standard four-point-probe DC Resistivity measurement puck with three channels.

CHAPTER III

SHARP SEMICONDUCTOR-TO-METAL TRANSITION OF VO_2 THIN FILMS ON GLASS SUBSTRATES*

3.1 Overview

Outstanding phase transition properties of Vanadium dioxide (VO_2) thin films on amorphous glass were achieved and compared with the ones grown on *c*-cut sapphire and Si (111) substrates, all by pulsed laser deposition. The films on glass substrate exhibit a sharp semiconductor-to-metal transition (~4.3 ℃) at a near bulk transition temperature of ~68.4 ℃ with an electrical resistance change as high as 3.2×10^3 times. The excellent phase transition properties of the films on glass substrate are correlated with the large grain size and low defects density achieved. The phase transition properties of VO_2 films on *c*-cut sapphire and Si (111) substrates were found to be limited by the high defect density.

* Reprinted with permission from "Sharp semiconductor-to-metal transition of VO_2 thin films on glass substrates" by Jie Jian, Aiping Chen, Wenrui Zhang and Haiyan Wang, Journal of Applied Physics 114, 244301, 2013. Copyright (2013).

3.2 Introduction

Vanadium dioxide (VO_2) has attracted extensive research interests and shows great potential in various devices such as sensors [14], switches [15], thermo/electrochromics [16], Mott transistors [48] and thermal actuators [17], because of its unique physical properties. For example, VO_2 single crystals exhibit an ultrafast (within 0.1 ℃) and reversible phase transition from a semiconductor phase to a metallic phase (SMT) at ~68 ℃ during heating process [5, 6, 45]. Through such a first-order phase transition [6], VO_2 transit from a tetragonal rutile phase ($P4_2/mnm$) to a monoclinic ($P2_1/c$) phase [7], which results in dramatic changes in its electrical [8-10] and optical properties [11-13].

One of the exciting electrical properties of VO_2 is that the resistivity switching during SMT can be as large as 10^4 to 10^5 times in bulk [87]. It is also desired to have a sharp transition and a small width of thermal hysteresis. However, it is quite challenging to grow such high quality of VO_2 films, especially on amorphous substrates, due to the existence of the multivalent vanadium ions (V^{2+}, V^{3+}, V^{4+}, V^{5+}) [24] and a wide range of point defects [81]. In addition, film stress, grain size, defects density and others could also vary [22, 23]. To achieve high quality and high performance VO_2 thin films, different substrates have been used [28, 176, 190, 240, 241]. Among all, *c*-cut sapphire substrate is commonly used to grow epitaxial VO_2 thin films [28, 167]. The films are highly textured along (001) or (010) on sapphire (0001) substrate [168]. Growth of VO_2 thin films on Si and amorphous glass substrates started about a decade ago [23, 191]. Si substrates are cheaper compared to sapphire ones. However it is quite challenging to

deposit high quality VO_2 thin films on Si because of the native oxide layer [169]. VO_2 films directly grown on glass substrates are in monoclinic phase [30] with preferred (011) out-of-plane orientation, however with random in-plane orientations [191]. A model has been previously proposed for the microstructure-property correlations of VO_2 based on defect density and interfacial energies [37]. Following that, much effort has been focused on achieving high quality VO_2 films with precise control of strain and SMT properties, either directly grown on sapphire and Si substrates [28, 176], or with different buffer layers [242, 243]. In contrast, the effort on the growth of high quality VO_2 thin films on glass substrates is much less, despite the advantages of the low cost of glass and the small substrate effect on the film electrical performance, as well as the great needs of high performance smart windows [16]. In general, VO_2 thin films on glass substrates have been reported to have poor electrical resistivity performance [30, 178, 191, 192]. For example, Hanlon *et al.* reported that a sputtering deposited VO_2 film on glass substrate exhibits a phase transition width as large as 10 ℃ [191]. The VO_2 film on glass substrate reported by Chiu *et al.* showed an 11 ℃ width of thermal hysteresis [178]. Therefore further exploration on the VO_2 growth on glass is essential to enable its future device applications on glass.

In this study, VO_2 thin films have been deposited on glass substrates and compared with the ones on *c*-cut sapphire and Si (111) substrates. Detailed electrical and microstructural characterizations have been conducted on samples on all different substrates. The microstructure properties, especially grain size, grain boundary orientation and defects density, have been correlated with the electrical performance

during heating and cooling process.

3.3 Experimental

VO_2 thin films were deposited on amorphous glass, single crystal *c*-cut sapphire and Si (111) substrates in a pulsed laser deposition (PLD) system with a KrF excimer laser (Lambda Physik Compex Pro 205, λ=248 nm). The laser beam was focused to obtain an energy density of approximately 3 J/cm^2 at a 45° angle of incidence. The depositions were conducted by using V_2O_5 target under oxygen deficient condition. The V_2O_5 targets were obtained by conventional powder pressing and sintering method. The oxygen pressure was optimized at 10 mTorr for all depositions. Substrate temperature was set to 500 ℃ during deposition for glass substrates, and 550 ℃ for *c*-cut sapphire and Si (111) substrates. All depositions were conducted at a repetition rate of 10 Hz and duration of 15 mins. Following deposition, the films were cooled down to room temperature under the same oxygen pressure with a cooling rate of 10 ℃/min.

The morphologies and microstructures of as-deposited films were characterized by X-ray diffraction (XRD) and transmission electron microscopy (TEM). XRD θ-2θ scans were performed using a Panalytical Empyrean 2 X-ray diffractometer with Cu K_α radiation. Detailed cross-section microstructural characterization including TEM and selected-area diffraction (SAD) patterns were acquired by JEOL 2010 analytical microscope with a point-to- point resolution of 0.23 nm. TEM samples were prepared using a standard cross-section sample preparation procedure, including manual grinding, polishing, dimpling and a final ion milling step (PIPS 691 precision ion polishing system,

3.7 keV). The electrical resistances of as deposited VO_2 films were measured by a standard four probe method with temperature varied from 17 ℃ (290 K) to 97 ℃ (370 K) in a physical property measurement system (PPMS, Quantum Design).

3.4 Results and discussion

Figure 3.1 shows the XRD θ-2θ scans of VO_2 thin films deposited on glass, *c*-cut sapphire and Si (111) substrates. For the film on glass substrate, a strong peak appears at ~27.8 °, which corresponds to monoclinic phase VO_2 (011). A minor peak at ~39.5 ° can be attributed to reflection from either VO_2 (020) or (002). This indicates that, despite the existence of other out-of-plane orientations, VO_2 prefers to texture along (011) on glass substrate since the (011) plane is the low-energy plane of monoclinic phase VO_2 [226]. The VO_2 on *c*-cut sapphire substrate shows primary peaks corresponding to monoclinic phase VO_2 (002) and Al_2O_3 (0006), which indicates that the VO_2 film has grown highly textured along *c*-axis. The film on Si (111) substrate shows peaks for VO_2 (011) and (022), which indicates that the VO_2 thin film deposited on Si (111) has its predominant texturing along (011) orientation owing to the low packing energy.

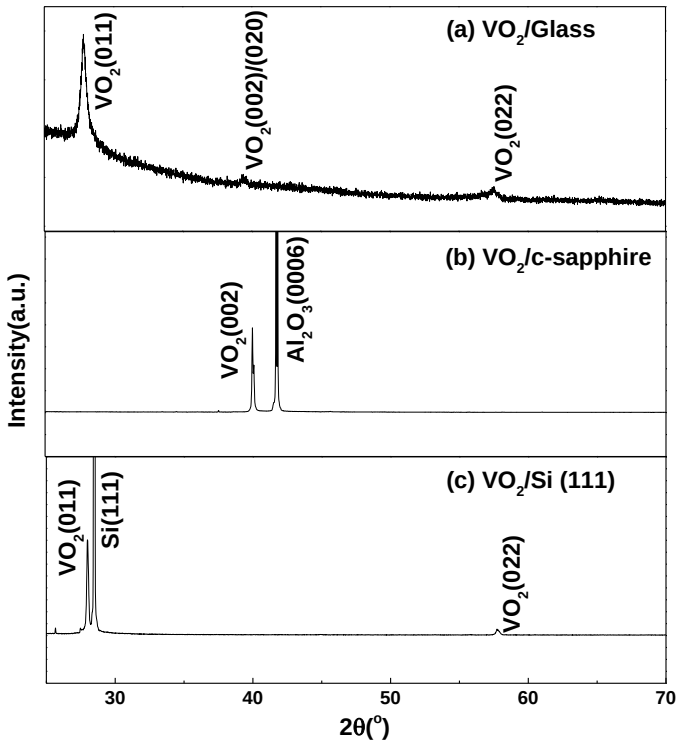

Figure 3.1 The XRD spectra of VO_2 thin films deposited on (a) glass, (b) *c*-cut sapphire and (c) Si (111) substrates.

Figure 3.2 shows the cross-section TEM images of the VO_2 thin film on glass substrate with a film thickness of approximately 230 nm. Obvious columnar structures have been observed in the film, as shown in Figure 3.2(a). The columnar width varies from about 90 nm to more than 130 nm. The high-resolution TEM (HR-TEM) image of the film/substrate interface (Figure 3.2(b)) confirmed the (011) preferred out-of-plane orientation of the VO_2 film on glass substrate. The corresponding SAD pattern, shown in Figure 3.2(c), was taken from the film/substrate interface area. A diffused diffraction ring is from the amorphous glass substrate while the diffraction dots are from the VO_2

film. The intensive out-of-plane VO_2 (011) diffraction confirmed the highly textured film. The slightly arced (011) and (022) diffraction dots indicate the slight misorientation of the grains out-of-plane.

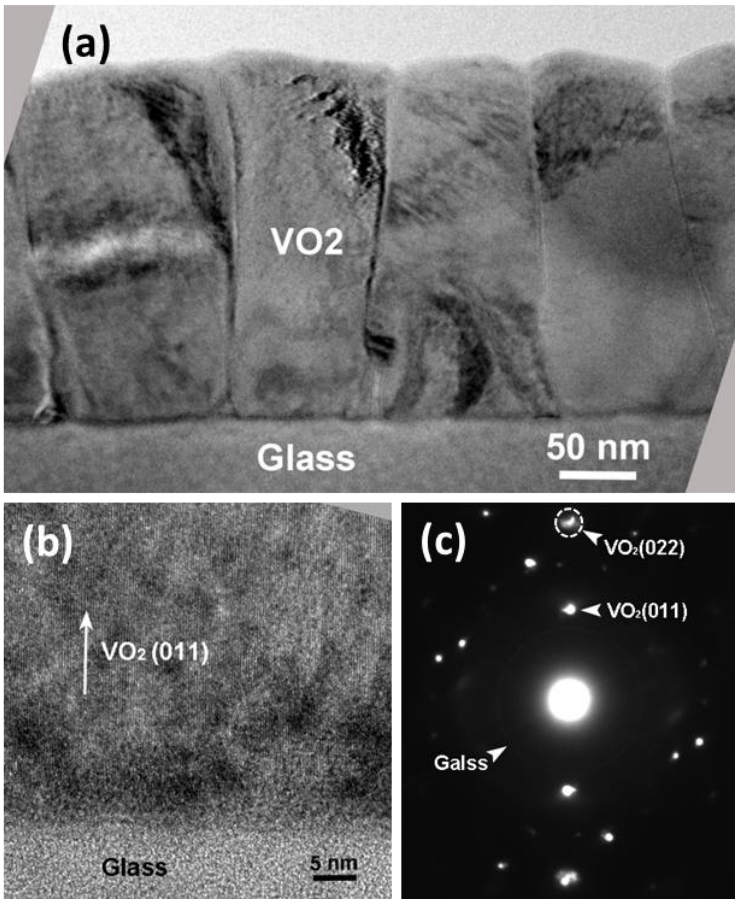

Figure 3.2 TEM study of VO_2 thin film on glass substrate: (a) Low magnification cross-section TEM image of film thickness and columnar grain structures, (b) HR-TEM image of VO_2/glass interface, (c) SAD pattern of film and substrate.

The VO_2 thin film on *c*-cut sapphire substrate shows a thickness of around 130 nm in the cross-section TEM image (Figure 3.3(a)). Ultrafine columnar domains have been observed in the film with an average width of approximately 5 nm. The HR-TEM image in Figure 3.3(b) shows a sharp and clean film/substrate interface. The (002) *d*-spacing of VO_2 is measured to be ~2.16 Å. The SAD pattern of the film/substrate interface area, shown in Figure 3.3(c), was taken from [200] zone of VO_2 ($[\bar{1}010]$ zone of *c*-cut sapphire). It further confirms the highly textured growth of the VO_2 film. Based on the diffraction pattern, the orientation relationships are determined to be VO_2 (002) // Al_2O_3 (0006) and VO_2 (020) // Al_2O_3 ($1\bar{2}10$). Furthermore, the overlap of the VO_2 (020) spot and the Al_2O_3 ($\bar{1}2\bar{1}0$) spot implies that along the $[1\bar{2}10]$ direction of *c*-cut sapphire, VO_2 and Al_2O_3 have almost perfect lattice matching. The SAD pattern in Figure 3.3(d) was taken from [020] zone of VO_2 ($[1\bar{2}10]$ zone of *c*-cut sapphire) by 30 ° tilting of the TEM sample. As the [020] zone of VO_2 is perpendicular to the [200] zone, it implies that the in-plane orientation of VO_2 on *c*-cut sapphire substrate has a three-fold symmetry, which may be attributed to the symmetry of sapphire (0001) plane. According to the diffraction patterns, it can be determined that the VO_2 (200) is almost parallel to the Al_2O_3 ($10\bar{1}2$). And along the $[10\bar{1}0]$ direction of *c*-cut sapphire, the VO_2 and Al_2O_3 have a 3:2 in-plane domain lattice matching relationship, i.e. 3 of VO_2 (200) match with 2 of Al_2O_3 ($10\bar{1}2$).

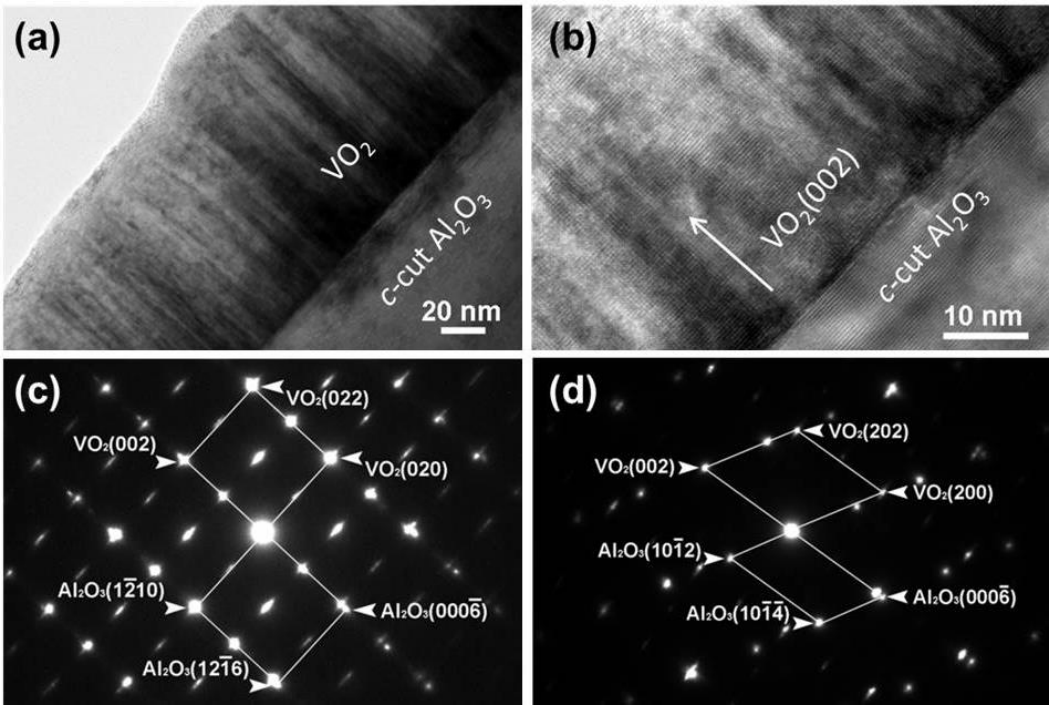

Figure 3.3 TEM study of VO_2 thin film on *c*-cut sapphire substrate: (a) Low magnification cross-section TEM image of film thickness and columnar domain structures, (b) HR-TEM image of VO_2/*c*-cut sapphire interface, (c) SAD pattern of film and substrate along the *c*-cut sapphire [$\bar{1}$010] zone, (d) SAD pattern of film and substrate along the *c*-cut sapphire [1$\bar{2}$10] zone.

It is interesting to note that the film grown on glass substrate results in a thicker film with a growth rate of around 0.26 Å/pulse while the film on *c*-cut sapphire substrate has that of about 0.15 Å/pulse. The different growth rate may be related with the film growth orientations as well as the different substrate surface energies. For example, the VO_2 (011) plane has a lower packing energy than (002) plane, which makes the adatoms easier to bond on the (011) free surface and thus lead to a higher growth rate along (011) orientation.

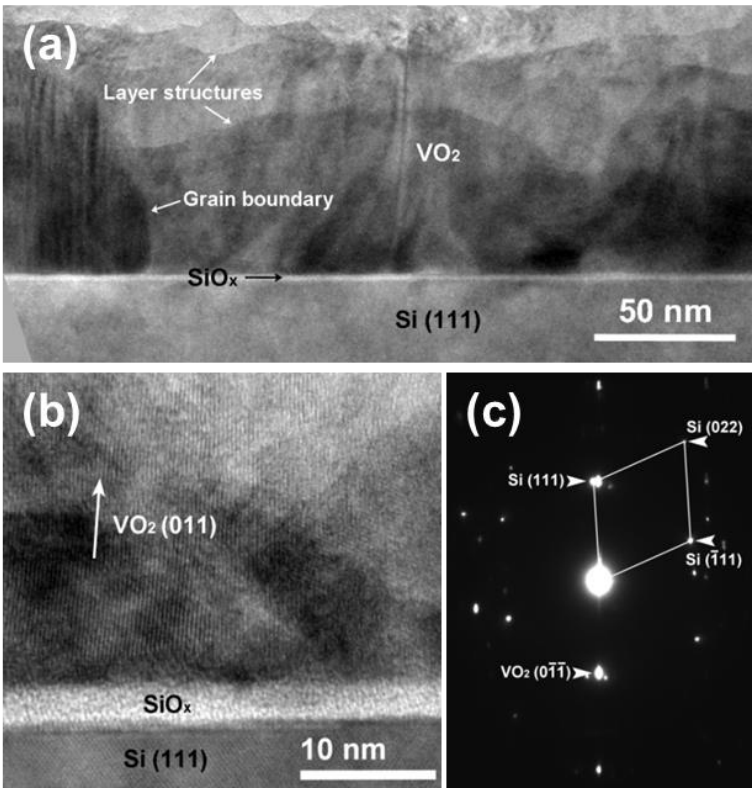

Figure 3.4 TEM study of VO_2 thin film on Si (111) substrate: (a) Low magnification cross-section TEM image of the layer structures and round grains in the film, (b) HR-TEM image of VO_2/Si (111) interface, (c) SAD pattern of film and substrate along the Si [$0\bar{1}1$] zone.

The cross-section TEM images of VO_2 thin film on Si (111) substrate are shown in Figure 3.4. The thickness of the film is estimated to be about 210 nm. A 2~3 nm silicon oxide (SiO_x) layer was observed between VO_2 films and Si (111) substrate in Figure 3.4(a). Instead of columnar grains/domains observed in the films on sapphire and glass substrates, the film on Si (111) substrate contains a layer structure with a few round grains. The interfaces between each layer are rough and sometimes discontinuous. The

(011) out-of-plane orientation of the film has been observed in the HR-TEM image of the film/substrate interface, as shown in Figure 3.4(b). The SAD pattern of the film/substrate interface area, shown in Figure 3.4(c), is taken in [011] zone of Si substrate. It also indicates a preferred (011) out-of-plane orientation of the film.

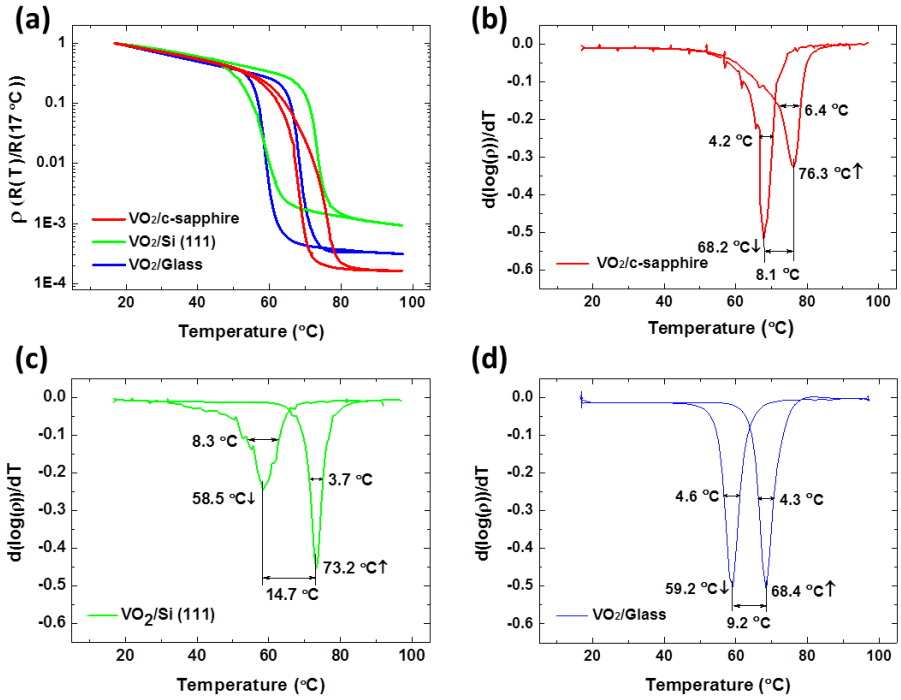

Figure 3.5 Phase transition influence on electrical resistance of VO_2 thin films grown on different substrates: (a) normalized resistance of all VO_2 films as a function of temperature, (b) resistance changing rate of VO_2 thin films on glass, (c) *c*-cut sapphire and (d) Si (111) substrates with temperature.

Figure 3.5(a) summarizes the normalized electrical resistances, ρ=R (T)/R (17 ℃), of VO_2 thin films on glass, *c*-cut sapphire and Si (111) substrates as a function of temperature. The film on glass substrate exhibits a resistance change (ΔA) of 3.2 × 10^3 times, which is smaller than that of the film on *c*-cut sapphire substrate (6.1 × 10^3) but larger than that of the film on Si (111) substrate (1.0 × 10^3). In order to determine the phase transition parameters, e.g. phase transition temperature (T_{SMT}), sharpness (ΔT) and the width of thermal hysteresis (ΔH) for each film, the derivation of $\log_{10}(\rho)$ has been calculated and plotted with respect to temperature, as shown in Figure 3.5(b), (c) and (d). Comparing to the VO_2 films on *c*-cut sapphire and Si (111) substrates, the film on glass substrate shows a much sharper and more reversible phase transition at a near bulk transition temperature. As summarized in Table 3.1, the VO_2 film on glass substrate possesses a T_{SMT} of around 68.4 ℃ during heating process, which is extremely close to that of the bulk single crystal VO_2 samples (~68 ℃). In comparison, the VO_2 films on *c*-cut sapphire and Si (111) substrates exhibit higher T_{SMT} (~76.3 ℃ and ~73.2 ℃, respectively). For the sharpness of phase transition, the VO_2 film on glass substrate has a ΔT as small as 4.3 ℃ for heating, and 4.6 ℃ for cooling processes, while the VO_2 film on *c*-cut sapphire substrate exhibits a ΔT of 6.4 ℃ during heating process and the film on Si (111) substrate shows a ΔT as large as 8.3 ℃ during cooling process. The two peaks in the derivation plot of the VO_2 film on glass substrate, as shown in Figure 3.5(d), are perfectly symmetric. This indicates that the film experienced two equal and reversible phase transition processes during heating and cooling. However, for the films on *c*-cut sapphire and Si (111) substrates, the width and amplitude of these two peaks are

quite different, which implies that the films may underwent unequal phase transition processes during heating and cooling. These results indicate the VO_2 film on glass substrate experiences a more reversible phase transition and thus possesses a more reliable performance. Besides, the VO_2 film on glass substrate exhibits a comparable ΔH (~9.2 ℃) with the film on *c*-cut sapphire substrate (~8.1 ℃), but much smaller than that of the film on Si (111) substrate (~14.7 ℃).

Table 3.1 Semiconductor-to-metal phase transition characteristics of VO_2 thin film deposited on different substrates.

Substrates	T_{SMT} (℃)	ΔT (℃)	ΔH (℃)	ΔA
Glass	68.4 (↑), 59.2 (↓),	4.3 (↑), 4.6 (↓)	9.2	3.2×10^3
c-sapphire	76.3 (↑), 68.2 (↓),	6.4 (↑), 4.2 (↓)	8.1	6.1×10^3
Si (111)	73.2 (↑), 58.5 (↓)	3.7 (↑), 8.3 (↓)	14.7	1.0×10^3

The phase transition temperature of the VO_2 thin films are heavily influenced by the film strain. Thus the near bulk T_{SMT} of the VO_2 film on glass substrate indicates a relatively small strain in the film. It is mainly because there is no lattice mismatch issue for the films grown on amorphous substrates. The higher T_{SMT} of VO_2 films on *c*-cut

sapphire and Si (111) substrates imply that these films may sustain large tensile strains.

The ΔA, ΔT, ΔH and reversibility of phase transition of the VO_2 thin films are strongly related with the film microstructures, such as defects density and grain (or domain) boundary orientation. Defects in the VO_2 film will lead to scattering of electrons and thus increase the resistivity of the film. This influence is more obvious for the metallic VO_2 because of its low resistivity. On the other hand, for semiconductor phase VO_2, defects will create extra energy levels in the band gap and lead to a decrease of resistivity [22]. Thus, high defects density will lower the resistivity amplitude and limit the sharpness and reversibility of phase transition. The thermal hysteresis is reported to be related with the interfacial energy, which depends on the nature and orientation of grain (domain) boundaries [37].

For the VO_2 film on glass substrate, the large grain size leads to a low grain boundary density and associated defects density, which could be the major reason of its outstanding electrical performance. In comparison, the high density of domain walls in the VO_2 film on *c*-cut sapphire substrate limits its properties. A large amount of random grain boundaries exist in the film on Si (111) substrate, which increases the density of defects and thus leads to a poor performance. Besides, the random boundaries increase the interfacial energy and contribute to a large width of thermal hysteresis of the film.

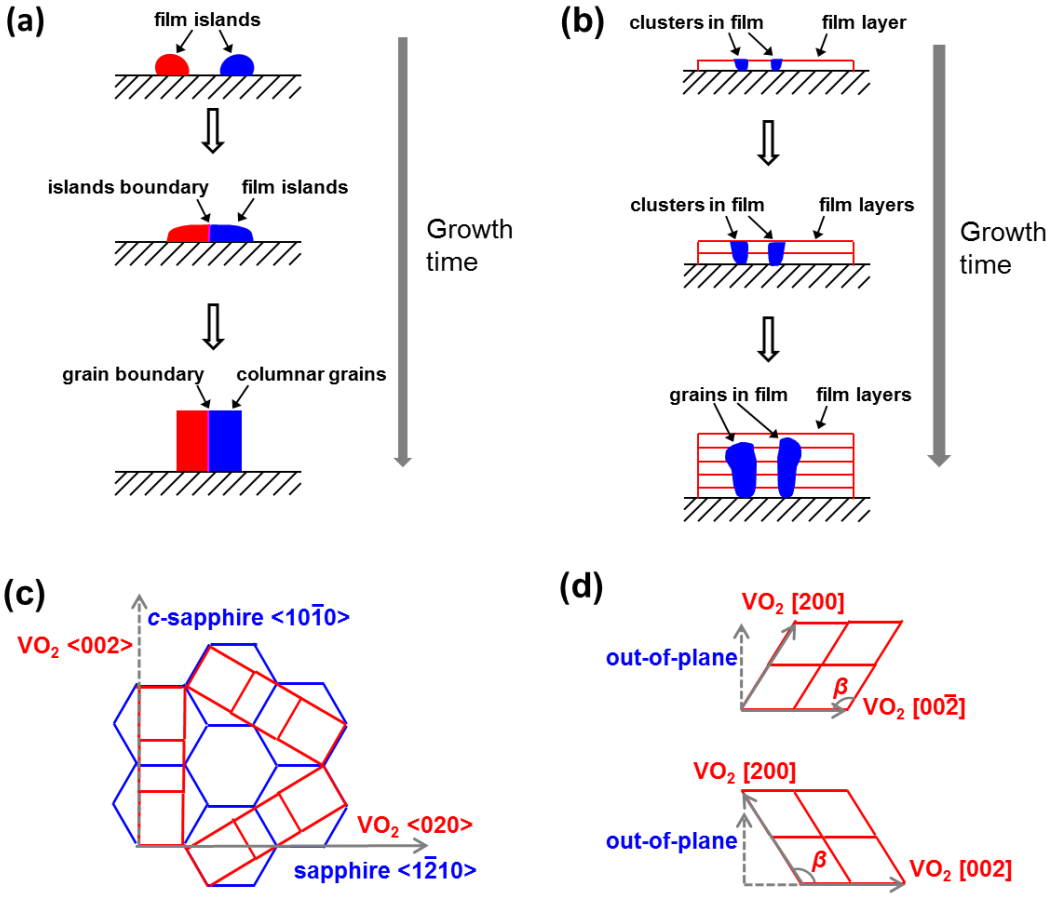

Figure 3.6 (a) features of the thin film varying with growth time when following Volmer-Weber mode, (b) features of the thin film varying with growth time following Stranski-Krastanov mode, (c) in-plane lattice matching schematic between VO_2 film and *c*-cut sapphire substrate based on the domain matching and the three-fold symmetry and (d) schematic of out-of-plane lattice orientations of VO_2 film on *c*-cut sapphire substrate based on the mirror symmetry.

The microstructures of VO_2 films on different substrates were attributed to the different film growth mechanisms, which are related with the surface energy and lattice matching relationship between films and substrates. The surface energy of VO_2 (011)

was reported to be 0.29 J/m^2 [244]. As high temperature will significantly lower the glass surface energy, VO_2 on glass substrate tends to grow in the Volmer-Weber mode (island growth mode), which requires the film to have a higher surface energy than the substrate. At the beginning of deposition, isolated VO_2 nucleus could form on substrate surface. These islands grow larger until meet with each other and form boundaries and therefore become columnar grains, as shown in Figure 3.6(a).

The surface energy of Si (111) was reported to be 1.74 J/m^2 when relaxed and 1.36 J/m^2 after 7×7 reconstruction [245], which is much higher than that of VO_2 (011). One could expect a 2D growth of VO_2 (011) on Si (111). However, the native SiO_x layer on Si(111) tends to lower the overall substrate surface energy, which leads to that the VO_2 film grows in the Stranski-Krastanov mode (2D-3D growth mode) on Si (111) substrate, as shown in Figure 3.6(b).

The excellent lattice matching relationship leads to a highly textured (002) orientation growth of VO_2 on *c*-cut sapphire substrate. However, the three-fold symmetry of sapphire (0001) results in an in-plane misorientation of VO_2, as shown in Figure 3.6(c). Interestingly, the VO_2 lattice has an out-of-plane mirror symmetry, as shown in Figure 3.6(d). These geometric symmetries cause the formation of fine domains in the VO_2 film on *c*-cut sapphire substrate. These in-plane and out-of-plane domain boundaries could strongly suppress the sharpness and reversibility of the phase transition.

3.5 Conclusion

Excellent electrical properties, i.e. a near bulk phase transition temperature (T_{SMT}) of around 68.4 ℃, a sharp transition (ΔT) of 4.3 ℃, a large resistance change (ΔA) of 3.2×10^3 times, and 9.2 ℃ width of thermal hysteresis (ΔH), are reported in the single phase VO_2 thin films on amorphous glass substrates. Their properties were compared with the ones on *c*-cut sapphire and Si (111) substrates, all deposited by PLD. VO_2 thin film on glass substrate has its predominant texturing along (011) orientation with large columnar grains. On *c*-cut sapphire substrate, highly textured (002) orientation VO_2 film was grown with a high density of domain boundaries both in-plane and out-of-plane. The VO_2 film on Si (111) substrate has a (011) preferred orientation with layer by layer microstructure. The outstanding SMT properties of the VO_2 films on glass substrates are related to their large grain size and low defects density. This study demonstrates that high performance VO_2 can be grown on low cost glass substrates, which is an important step toward low cost VO_2 based devices on glass.

CHAPTER IV

ROLES OF GRAIN BOUNDARIES ON THE SEMICONDUCTOR TO METAL PHASE TRANSITION OF VO_2 THIN FILMS*

4.1 Overview

Vanadium dioxide (VO_2) thin films with controlled grain sizes are deposited on amorphous glass substrates by pulsed laser deposition. The grain boundaries (GBs) are found as the dominating defects in the thin films. The semiconductor to metal transition (SMT) properties of VO_2 thin films are characterized and correlated to the GB density. The VO_2 films with lower GB density exhibit a sharper SMT with larger transition amplitude. A high resolution TEM study at GB area reveals the disordered atomic structures along the boundaries and the distorted crystal lattices near the boundaries. The VO_2 SMT amplitude and sharpness could be directly related to these defects at and near the boundaries.

---

* Reprinted with permission from "Roles of grain boundaries on the semiconductor to metal phase transition of VO_2 thin films" by Jie Jian, Wenrui Zhang, Clement Jacob, Aiping Chen, Han Wang, Jijie Huang and Haiyan Wang, Applied Physics Letters 107, 102105, 2015. Copyright (2015).

4.2 Introduction

Vanadium dioxide (VO_2) is known to exhibit an ultrafast (within 0.1 ℃) and reversible phase transition from a semiconductor phase to a metallic phase at ~68 ℃ [5, 45]. Because of this fascinating characteristic, VO_2 shows great potential in various devices including sensors [14], switches [15], thermo/electrochromics [16], Mott transistors [48], and thermal actuators [17], and thus has attracted extensive research interests. The semiconductor phase VO_2 has a monoclinic ($P2_1/c$) crystal structure [45]. By the first-order semiconductor-to-metal phase transition (SMT) process [5], VO_2 transits to tetragonal crystal structure ($P4_2/mnm$) [7] which results in dramatic changes in its electrical [9] and optical properties [11].

Compared with single crystalline VO_2, the properties of VO_2 thin films can be largely affected by many factors including defects density [22], strain [23], and the existence of the multivalent vanadium ions (V^{2+}, V^{3+}, V^{4+}, V^{5+}) [24]. Thus it's quite challenging to synthesize high quality VO_2 thin films with sharp transition width, narrow thermal hysteresis, and large electrical and optical property change. A model previously proposed by Narayan *et al*. has correlated some of the microstructures of VO_2 to its properties. It suggests that the sharpness of transition (ΔT) and the amplitude of transition (ΔA) are both related to the overall defects density in VO_2 [37]. Grain boundary (GB), as one of the major defects in the VO_2 thin films, has a dramatic influence on the SMT properties of VO_2 thin films [22, 203]. However, the GB effects on the SMT properties of VO_2 thin films are still under debate. Especially, the mechanisms of GB influence on VO_2 SMT properties are still under investigation.

Brassard *et al.* demonstrated that when VO_2 grew thicker on Si_3N_4 /Si substrates, the grains gradually grow larger in the top parts of the thin films and result in a sharper phase transition and larger transition amplitude [22]. Aliev *et al.* found that the grain size increase of VO_2 thin films on Al_2O_3 and Si substrates could reduce the width of thermal hysteresis but reduces the phase transition sharpness [203]. In addition, co-existence of other defects and VO_2 phases is also one of the major challenges for studying the GB effects on VO_2 SMT properties. For example, VO_2 thin films grown on *c*-cut sapphire substrates usually contain high density 120 ° in-plane rotated domain boundaries, which have dominant impacts on the SMT properties [28]. VO_2 films deposited on $SrTiO_3$ (STO) substrate contain a large amount of metastable (B) phase [246]. Furthermore, film thickness and the stress induced by substrates could also affect the SMT properties of VO_2 thin films [101, 247, 248].

In this work, we grew VO_2 thin films with controlled grain size and film thickness on amorphous glass substrates. Amorphous glass substrates allow a relatively free growth of thin films, which can minimize the existence of other kinds of defects including domain boundaries and misfit dislocations. As there's no lattice matching relationship between the film and substrate, the substrate induced stress could also be minimized. Electrical resistance measurements were conducted on VO_2 thin films with different grain sizes to characterize the SMT properties. The transition amplitude and sharpness were correlated to grain size and GB density. The microstructures of the GB areas were characterized by high resolution transmission electron microscopy (HR-TEM) and then used to explain the GB effects on the SMT properties of VO_2 films.

4.3 Experimental

VO_2 thin films on glass substrates were grown by a pulsed laser deposition (PLD) system (KrF laser, 248 nm). A V_2O_5 target, obtained by conventional powder pressing and sintering method, was used as the material source for VO_2. The phase of VO_2 was achieved by an optimized substrate temperature of 500 ℃ and oxygen pressure of 10 mTorr. The laser repetition rate was varied from 1Hz, 2Hz, 3Hz, to 10 Hz to control the grain size of VO_2 films. Deposition time was optimized for each repetition rate to obtain a 250 nm thick film. The microstructures of as-deposited films were characterized by X-ray diffraction (XRD) and transmission electron microscopy (TEM). XRD θ-2θ scans were performed using a PANalytical Empyrean 2 X-ray diffractometer with Cu K_α radiation. Bright field and dark field TEM images were acquired by FEI Tecnai G2 F20 analytical microscope with a point-to-point resolution of 0.24 nm. The electrical resistance of as-deposited VO_2 films were measured by a standard four probe method with temperature varied from 17 ℃ (290 K) to 97 ℃ (370 K) in a physical property measurement system (PPMS, Quantum Design).

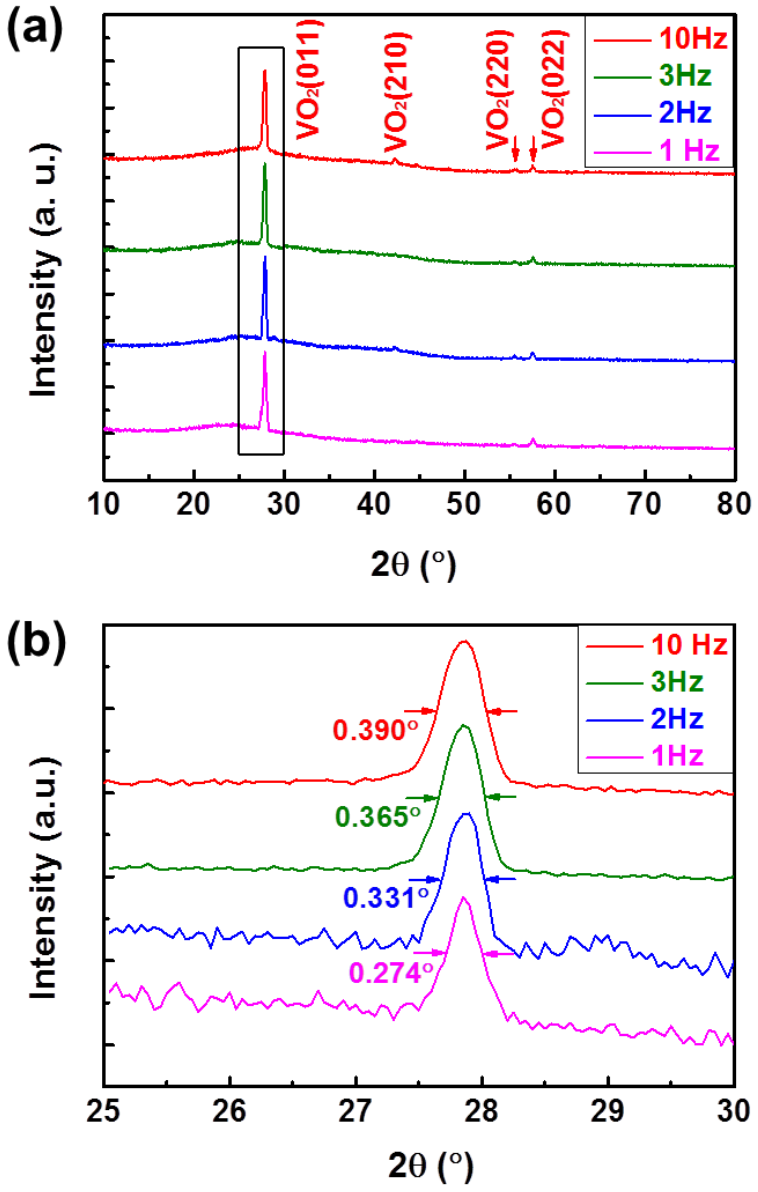

Figure 4.1 (a) The XRD *θ-2θ* spectra of VO_2 thin film deposited on amorphous glass substrate with a repetition rate of 10 Hz, 3 Hz, 2 Hz and 1 Hz. (b) Enlarged VO_2 (011) peak of VO_2 thin films deposited at different rates.

4.4 Results and discussion

Figure 4.1(a) shows the XRD θ-2θ scans of VO_2 thin films deposited at 1 Hz, 2 Hz, 3 Hz, and 10 Hz. All the VO_2 thin films with different deposition rates present similar XRD θ-2θ scan results. A strong peak appears at ~27.8 °, which corresponds to monoclinic phase VO_2 (011). The minor peak at ~42.2 ° is indexed as VO_2 (210). The weak peak at ~55.7 ° corresponds to VO_2 (220). The result indicates that, despite the lack of epitaxial growth, VO_2 prefers to texture along (011) on glass substrate since the (011) plane is the low-energy plane of VO_2 monoclinic phase. No obvious peaks corresponding to other VO_2 or VO_x phases have been observed, suggesting the high purity of VO_2 monoclinic phase in all the films. The rectangular area marked in Fig. 1(a), ranging from 25 ° to 30 °, is enlarged and shown in Figure 4.1(b). No obvious peak shift was measured for VO_2 films with different deposition rates. It implies that limited strains were introduced in the film when changing deposition rate. The width of the VO_2 (011) peaks shows a consistent change with the deposition rate. When the deposition rate reduced from 10 Hz to 1 Hz, the full width at half maximum (FWHM) of the VO_2 (011) peaks decreases from 0.39 ° to 0.274 °. As a sharper peak is attributed to larger average grain size in polycrystalline thin films [249], this result indicates that the VO_2 films with lower deposition rates could have larger average grain sizes.

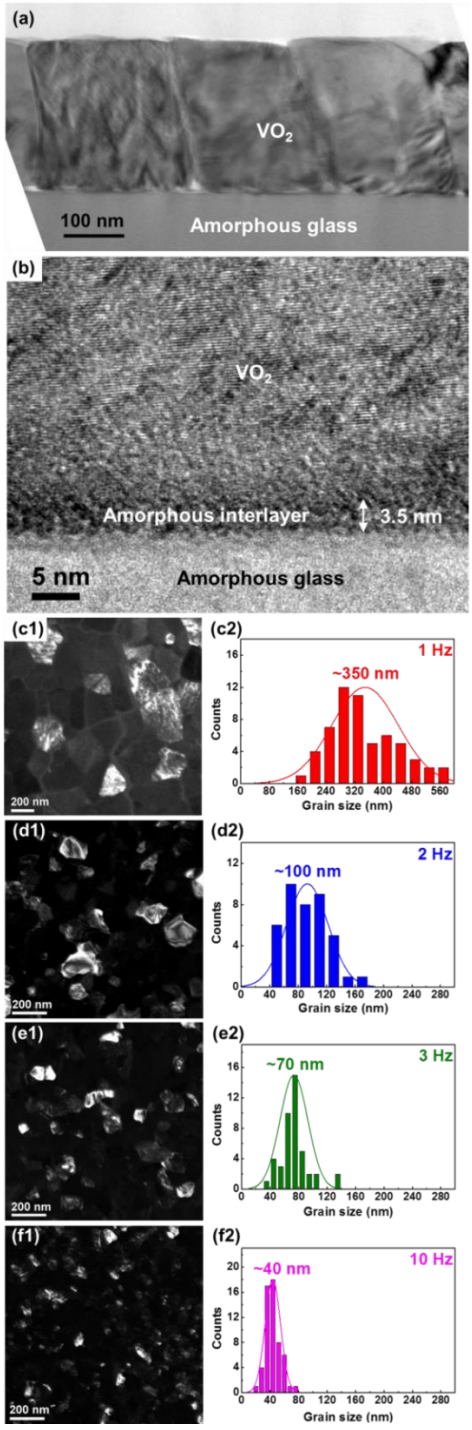

Figure 4.2 (a) Cross-section TEM image of the VO_2 thin film on glass substrate deposited at 2 Hz. (b) The corresponding HRTEM image of the film/substrate interface. (c1)-(f1) Plan-view dark field TEM images of the VO_2 thin films on glass substrates deposited at 1 Hz, 2 Hz, 3 Hz, and 10 Hz, respectively. (c2)-(f2) The corresponding grain size distributions of VO_2 thin films deposited at different rate.

The microstructures of VO_2 thin films, especially the grain size distribution, were further characterized by TEM. Figure 4.2(a) shows the cross-section TEM image of the VO_2 thin film deposited at 2 Hz. Figure 4.2(b) shows the corresponding high-resolution TEM (HRTEM) image at the film/substrate interface. All the films have a comparable thickness of about 250 nm with obvious columnar grain structures. A thin amorphous interlayer (~3.5 nm) exists in between the glass and crystalline VO_2, which could be attributed to the amorphous nature of glass substrate and a possible film-substrate interaction. Following this interfacial layer, the clean contrast of the grains indicates limited numbers of domains and point defects in each grain in the bulk part of the film. It has been previously reported that the substrate induced strain and defects at the film/substrate interface also play a critical role in the overall SMT properties [247, 248]. However, for this case, because of the amorphous substrate as well as the thin interfacial amorphous layer, the film shows little or no obvious contrast variation along the interface, which indicates that the substrate induced strain and defects are limited. Overall these microstructural characteristics suggest that GBs are dominant defects in the VO_2 thin films on glass substrates. Thus the GB density change is expected to be a major factor on the phase transition property of these films. Figure 4.2(c1)-(f1) shows the plan-view dark field TEM images of the VO_2 thin films under different deposition rates. The grain size decreases with the increase of deposition rate, which is consistent with the XRD results. A careful grain size distribution analysis in Figure 4.2(c2)-(f2) shows that the average grain size of 350 (±50) nm, 100 (±15) nm, 70 (±10) nm, and 40 (±5) nm for the films deposited at 1 Hz, 2 Hz, 3 Hz, and 10 Hz, respectively. The

impacts of the deposition rate on the grain size of VO_2 films could be the following. A lower deposition rate means a longer interval between two laser pulses, which allows longer diffusion time for the adatoms on the substrate surface. Larger grain sizes are thus expected. In addition, the films deposited at a lower rate usually require a longer deposition time which also results in higher thermal budget and thus a larger grain size.

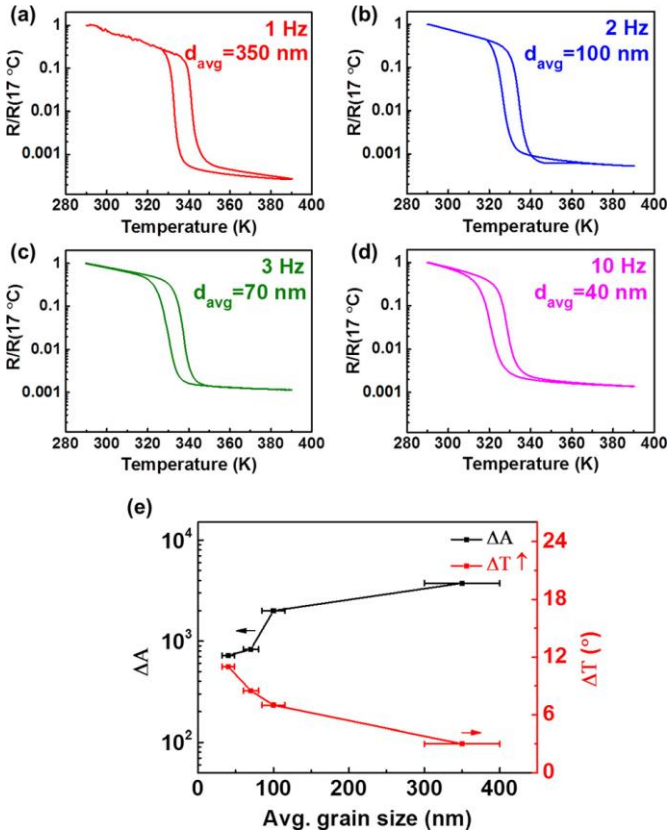

Figure 4.3 Normalized resistance of VO_2 films deposited at (a) 1 Hz, (b) 2 Hz, (c) 3Hz and (d) 10 Hz as a function of temperature. (e) The SMT width and the electrical resistance amplitude change of VO_2 thin films varying with average grain size.

The SMT properties of VO_2 films with different grain sizes were characterized by measuring the electrical resistance change during phase transition. Figure 4.3(a)-(d) summarizes the normalized electrical resistances, $\rho=R(T)/R(17\ ℃)$, of VO_2 thin films as a function of temperature. The transition amplitude (ΔA), sharpness ($\Delta T\uparrow$, $\Delta T\downarrow$), and width of thermal hysteresis (ΔH) of each film are calculated and listed in Table 4.1. The ΔA and $\Delta T\uparrow$ vs. average grain size are plotted in Figure 4.3(e). It is clear that both ΔA and ΔT are directly correlated to the film average grain size (GB density). As the average grain size increases from 40 nm to 350 nm, the transition amplitude of electrical resistance increases dramatically from 720 to 3750. Meanwhile, the transition gets sharper from ΔT=11 K to 3 K. This result suggests that the GBs strongly affect both the transition amplitude and sharpness of VO_2 thin films. It is noted that the ΔH values of VO_2 films don't completely follow the trend of grain size variation. A previous report suggested that ΔH could be strongly influenced by the nature and orientation of grain boundaries [37]. Because the in-plane grain orientations are random for all the VO_2 films on glass substrates, their ΔH values varies but are considered in a comparable range. It is also noted that in Figure 4.3(a) and (b), at high temperatures after major phase transitions (>350 K), the samples still show different resistance values at the same temperature during cooling and heating processes. This transition tail could be caused by the existence of a small amount of other VO_x phases in the samples.

Table 4.1 SMT characteristics of VO_2 thin film deposited at different repetition rate.

Dep. rate (Hz)	Avg. grain size (nm)	ΔA	ΔT↑ (K)	ΔT↓ (K)	ΔH (K)
1	350 ±50	3750	3.0	4.0	9.1
2	100 ±15	2000	7.0	7.5	9.6
3	70 ±10	830	8.5	8.9	10.1
10	40 ±5	720	11.0	15.0	9.5

Fig 4.4 (a) shows a high resolution TEM image of a typical GB area for the sample deposited at 2 Hz. As indicated in the middle of the image, the GB area is amorphous with a bright contrast and the GB width of around 5 nm. Right beside the GB, the VO_2 lattice on both sides of the GB shows a gradual contrast change inwards from bright to dark. In the inset, the average *d*-spacing of VO_2 lattice was plotted as a function of the distance from the GB. To minimize measurement errors, each *d*-spacing value was calculated by averaging the *d*-spacing of three neighboring lattices. The lattice close to the GB shows a *d*-spacing of around 0.3 nm. Interestingly, the *d*-spacing gradually increases with the distance from the GB and finally approaches to a constant value (~0.325 nm). This is very close to the *d*-spacing of VO_2 [011] (0.322 nm) and thus the grain orientation of the left side grain in Figure 4.4(a) is determined to be VO_2 (011). The *d*-spacing variation in the grain could be attributed to the stress field generated by GBs. GB-induced strain gradually decreases away from the GB area, which is similar to a previous report [250]. In the area next to the GB, marked in blue dashed lines, VO_2

lattice is highly distorted due to the strain and then gradually relaxed inwards away from the GB. The width of the distorted region in the left grain in Figure 4(a) is estimated to be about 6.8 nm.

The variation in transition amplitude (ΔA) and sharpness (ΔT) is related to the strain and disorders at the GB areas. For further illustration and discussion, a schematic diagram representing the above GB area was shown in Figure 4.4(b). The red ball symbols represent the location of vanadium atoms in the lattices. Two VO_2 grains with about 20 ° rotation are separated with an amorphous grain boundary area (light purple area in Figure 4.4(b)). This highly disordered area is usually 2~5 nm thick. Several VO_2 unit cells are labeled by blue squares to show the lattice parameter variation. The primary lattices shown in both grains are *c*-axis lattices. The lattice strain (ε) is represented by gradient blue color. First, due to the high disorders in GB areas, the phase transition during temperature change could be significantly different from the bulk regions. The films with smaller grain sizes have a higher GB density. It contains more disordered areas which lead to the decrease of transition amplitude (ΔA) and decreased transition sharpness (ΔT). Second, the distorted lattices also have impact on the overall phase transition characteristics. In the areas close to the GBs, the VO_2 lattices are highly strained as illustrated in the gradient blue areas in Figure 4.4(b). It was reported that, for ceramic materials, the strain in a typical lattice decreases exponentially with the distance

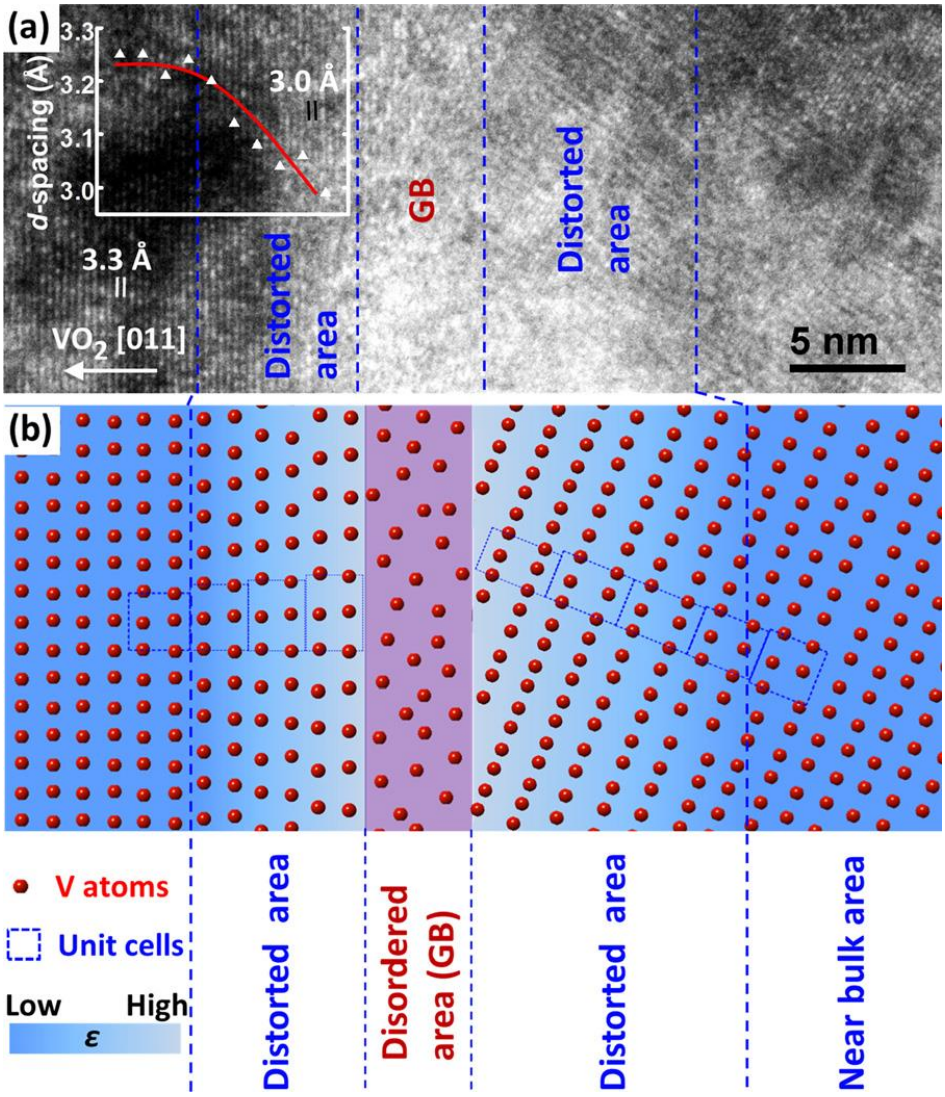

Figure 4.4 (a) HR-TEM image of a GB area in the VO_2 thin film. It contains amorphous boundary, distorted unit cells and uniform lattice. The inset shows the *d*-spacing profile as the distance from the GB. (b) Schematic diagram of a GB regime in the VO_2 thin films. In the boundary (purple area), the atoms are disordered. The VO_2 unit cells beside the boundary are distorted by stress. The stress is generated by the GB and decreases with distance (represented by gradient blue). The unit cells away from the GB are near bulk (dark blue areas).

from the GBs and it usually approaches to 0 within 10 nm from the GBs [115]. Thus in the area away from the GB, shown as uniform blue in Figure 4.4(b), the VO_2 lattice is close to the bulk. The model of strain distribution at GBs has been widely confirmed in both metallic and ceramic materials; and the magnitude and effective range of GB-generated strain vary with materials [250, 251]. Despite the strain generated by GBs is in a short range (~10 nm), the distorted area becomes significant in nanocrystalline grains, for example, 40 nm, 70 nm, and 100 nm in this case.

In the stress-temperature phase diagram of VO_2, the relationship between the transition temperature T_C and the uniaxial stress σ is calculated based on the Clausius-Clapeyron equation,

$$dT_C/d\sigma = (\varepsilon_0 T_C^0)/\Delta H \quad (4.1)$$

where T_C^0 is the transition temperature without stress (~68 ℃ for VO_2), ΔH is the latent heat of the transition, and ε_0 is a coefficient [106]. Based on this theory calculation, the stress in the distorted area could result in the shift of the VO_2 phase transition temperature. It was also reported that GBs with different orientations could introduce stress with different magnitudes [250, 251]. Thus the stress field generated by GBs could spread the phase transition temperature of VO_2 to a wider range and lead to the broadening of the transition sharpness (ΔT). The theoretic result of strain effect on VO_2 phase transition was supported by several experimental reports. For example, *Case* reported that by annealing the pre-deposited VO_2 thin films, the GB density decreased and the intrinsic stress could be released, which led to a higher phase transition amplitude and sharper transition width [91]. For the VO_2 nanoparticles, reports also

show that larger particle size results in sharper phase transition with larger amplitude because of less surface stress and disorders [112, 249]. In the case of VO_2 nanowires, large stress could have more significant effects on the overall transition properties such as metallic phase domain formation at room temperature [77, 105]. The previous reports and the current grain size dependent study all suggest that the stress (GB-induced stress for this case), played a critical role in the overall phase transition properties.

4.5 Conclusion

In conclusion, polycrystalline VO_2 thin films with the average grain size of 350 nm, 100 nm, 70 nm and 40 nm were deposited on amorphous glass substrates by PLD. The phase transition properties of each VO_2 film were correlated with the grain size. The film with larger average grain sizes (thus lower GB density) exhibits better phase transition properties, i.e. higher transition amplitude and sharper transition (ΔA as high as 3750 and ΔT as narrow as 3K for the sample with the grain size of 350 nm). HR-TEM image at the GB area revealed that the GB is highly disordered and the VO_2 lattices next to the GB are strained due to the stress at GBs. Both highly disordered GBs and strained lattices contribute to the decrease of transition amplitude and broadening of transition sharpness for VO_2 with grain size smaller than 100 nm. This study provides a direct understanding of the GBs effects on VO_2 phase transition properties and thus presents a guide for the structure designs of the VO_2-based devices with desired properties.

CHAPTER V

CONTINUOUS TUNING OF PHASE TRANSITION TEMPERATURE IN VO_2 THIN FILMS ON *C*-CUT SAPPHIRE SUBSTRATES VIA STRAIN VARIATION

5.1 Overview

Vanadium dioxide (VO_2) thin films with controlled thicknesses are deposited on *c*-cut sapphire substrates with Al-doped ZnO (AZO) buffer layers by pulsed laser deposition. The surface roughness of AZO buffer layers is varied by controlling oxygen pressure during growth. The strain in the VO_2 lattice is found to be dependent on the VO_2 thickness and the VO_2/AZO interface roughness. The semiconductor-to-metal transition (SMT) properties of VO_2 thin films are characterized and the transition temperature (T_c) is successfully tuned by the VO_2 thickness as well as the VO_2/AZO interface roughness. It shows that the T_c of VO_2 decreases with the decrease of film thickness or VO_2/AZO interface roughness. Other SMT properties of the VO_2 films are maintained during the T_c tuning. Atomic model of the VO_2/AZO coupling shows that the strain in the VO_2 films is mainly generated by their lattice mismatch. High resolution TEM study at a rough VO_2/AZO interface area reveals that the strain is localized close to the interface and relaxed by generating high density of dislocations.

5.2 Introduction

Vanadium dioxide (VO_2) is known to exhibit an ultrafast (within 0.1 ℃) and reversible semiconductor to metal phase transition (SMT) at ~341 K [5, 6, 45]. Through

such a first-order phase transition [6], VO_2 transit from a tetragonal rutile phase ($P4_2/mnm$) to a monoclinic ($P2_1/c$) phase [7], resulting in dramatic changes in its electrical[8-10] and optical properties [11-13]. Because of these unique characteristics, VO_2 has attracted extensive research interests and shows great potential in various devices such as sensors [14], switches [15], thermos /electrochromics [16], Mott transistors [48] and thermal actuators [17].

Comparing to their bulk counterparts, VO_2 thin film is desired in many applications owing to its 2-dimentional geometry and the compatibility with current devices [252]. In order for VO_2 thin films to be used in practical devices, the phase transition temperature (T_c) of VO_2 is required to be tunable to satisfy the working environments of different devices [143, 148, 252]. In the past decade, a significant amount of work has been focused on the T_c tuning of VO_2 thin films [192, 199, 253, 254]. Introducing doping elements provides a common approach of T_c tuning by shifting the fermi level of the semiconductor VO_2. VO_2 thin films with different doping elements, including Mg, Mo, W, Ti and Cr, have been achieved and the T_c of the films has been tuned from less than 200 K to more than 350 K [31, 34, 255, 256]. However, as the properties of VO_2 thin films are largely affected by defects [22, 207] and the existence of the multivalent vanadium ions (V^{2+}, V^{3+}, V^{4+}, V^{5+}) [24], increasing doping level in the VO_2 films was usually accompanied with a significant drop of the transition amplitude and broadening of transition sharpness. N. R. Mlyuka *et al.* reported that the T_c of VO_2 films was tuned to ~ 320 K with 5.8 at.% doping of Mg. However, the transition amplitude of the films was deducted by a factor of 2 and the transition process lasted for

more than 40 K [31].

As VO_2 is a Mott-insulating material [9], the T_c of VO_2 could also be controlled by lattice strain [70]. The strain in an epitaxial thin film is mainly dominated by the lattice mismatch between film and substrate. Therefore, various substrates have been used for the growth of VO_2 to tune the strain and thus the T_c of the films. VO_2 thin films on STO (111) [51] and *r*-cut sapphire substrates [176] have been usually reported to have a lower shift of T_c, while the VO_2 on MgO (111) [177] and *c*-cut sapphire [28] substrates commonly showed an upper shift of T_c. In addition, different buffer layers, such as TiO_2, CeO_2, ZnO, SnO_2, etc., have been incorporated between VO_2 and substrates to provide some range of strain tuning [136, 170, 175, 178, 179]. However, as the lattice matching relationship between VO_2 and each individual material is pre-determined, the T_c tuning based on lattice mismatch strain is thus discrete. Besides, with the increase of lattice mismatch, more defects could be introduced in the VO_2 film, which leads to the drop of other SMT properties [199]. Therefore, to enable device applications, it is essential for further exploration on continuous T_c tuning of VO_2 with maintenance of other SMT properties.

Based on the Stoney formula, the substrate could have more strain effects on the films with less thickness [257]. In addition, the interfacial roughness could further influence the strain status because of the different lattice matching relationships and the dislocations generations at local areas. Therefore in this work, we explored the feasibility of T_c tuning via strain in VO_2 thin films by two approaches: controlling the VO_2 film thicknesses and controlling the surface roughness of Al-doped ZnO (AZO)

buffer layers on *c*-cut sapphire substrates. Microstructural and strain characterizations have been conducted on all the samples. Electrical resistivity measurements were conducted on the VO_2 thin films to characterize the SMT properties. The transition temperature tuning was correlated to the film thickness and VO_2/AZO interface roughness. The lattice matching relationship between VO_2 and AZO was established. The atomic structures and strain distribution of rough VO_2/AZO interfaces were characterized by high resolution transmission electron microscopy (HR-TEM).

5.3 Experimental

AZO buffer layers and VO_2 thin films were all deposited by a pulsed laser deposition (PLD) system with a KrF excimer laser (Lambda Physik Compex Pro 205, λ=248 nm). The laser beam was focused to obtain an energy density of approximately 3 J/cm^2 at a 45 ° angle of incidence. The AZO target was hot pressed using a mixture of 5 wt% Al_2O_3 and ZnO powders and sintered at 1100 °C for 6 hours. The AZO buffer layers were all deposited at 750 ℃ on *c*-cut sapphire substrates. The oxygen partial pressure was varied from 50 mtorr, 100 mtorr, 150 mtorr, to 200 mtorr to control the surface roughness of AZO [258]. The deposition time was set as 6 min for 50, 100 and 150 mtorr samples and increased to 10 min for 200 mtorr samples in order to guarantee full coverage of the substrates. A V_2O_5 target, obtained by conventional powder pressing and sintering method, was then used as the material source for VO_2 deposition. The VO_2 thin films were all achieved on AZO buffer layers by an optimized oxygen pressure of 10 mTorr and laser repetition rate of 2 Hz. The Substrate temperature was set as 450 ℃ to

minimize the interaction between VO_2 and AZO. The thicknesses of VO_2 films were controlled by adjusting the deposition time from 10 min, 25 min to 50 min.

The microstructures of the as-deposited films were characterized by X-ray diffraction (XRD) and transmission electron microscopy (TEM). XRD θ-2θ scans were performed using a PANalytical Empyrean 2 X-ray diffractometer with Cu K_α radiation. Bright field EM images and selected area electron diffraction (SAED) patterns were acquired by FEI Tecnai G2 F20 analytical microscope with a point-to-point resolution of 0.24 nm. TEM samples were prepared using a standard cross-section sample preparation procedure, including manual grinding, polishing, dimpling and a final ion milling step (PIPS 691 precision ion polishing system, 3.7 keV). The electrical resistivity of as-deposited films was measured by a standard four probe method with temperature varied from 290 K to 370 K in a physical property measurement system (PPMS, Quantum Design).

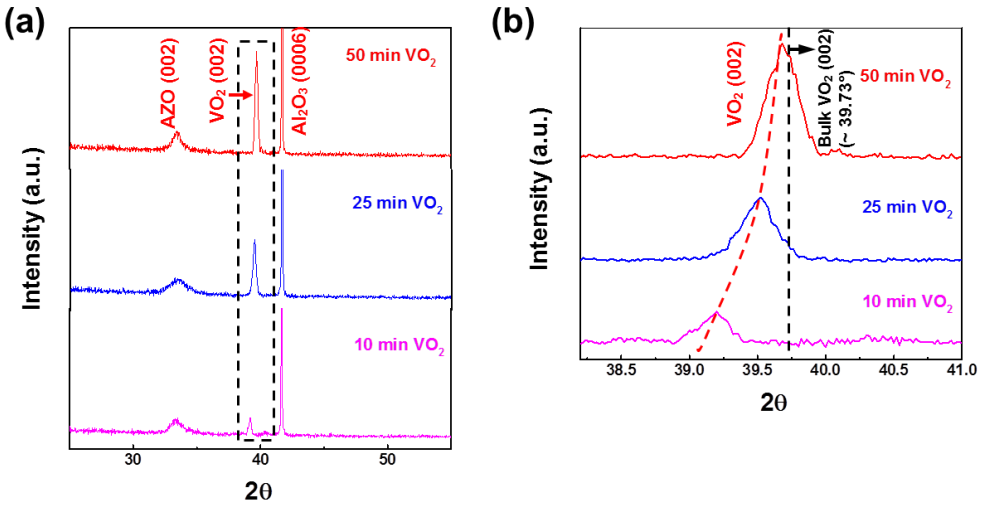

Figure 5.1 (a) The XRD θ-2θ spectra of VO_2 thin films deposited on AZO buffered *c*-cut sapphire substrates with deposition time of 50 min, 25 min and 10 min. (b) Enlarged VO_2 (002) peaks of VO_2 thin films with different thicknesses. The black dash line represents the bulk VO_2 (002) peak position.

5.4 Results and Discussion

5.4.1 T_c tuning by VO_2 film thickness

VO_2 thin films with different layer thicknesses were deposited on AZO buffered *c*-cut sapphire substrates. All the AZO buffer layers were deposited at the oxygen partial pressure of 50 mtorr. Figure 5.1(a) shows the XRD θ-2θ scans of VO_2 thin films with deposition time of 50 min, 25 min and 10 min, respectively. The AZO (002) peak appears at 33.45 ° for all samples. It shifts to lower angle compared to the standard ZnO (002) peak position (34.5 °), which indicates the effective doping of Al in ZnO lattice. All the VO_2 films show primary peaks corresponding to monoclinic phase VO_2 (002), which

indicates that the VO_2 films have grown highly textured along *c*-axis. The decrease of VO_2 (002) peak intensity is caused by the decrease of film thickness. The rectangular area marked in Figure 5.1(a), ranging from 38.2 ° to 41 °, is enlarged and shown in Figure 5.1(b). The black dash line represents the strain free VO_2 (002) peak position (39.73 °). The (002) peaks of all the VO_2 thin films shift to the lower angle side of the black dash line, which indicates tensile strains along the *c*-axis of VO_2 for all the films. The red dash line shows that with the decrease of VO_2 deposition time, the peak position of VO_2 (002) gradually shifts to lower angle and gets further away from the strain free VO_2 (002) peak (black dash line). This indicates that the decrease of VO_2 film deposition time leads to an increase of tensile strain along the VO_2 *c*-axis. Based on the XRD results, the tensile strains along the *c*-axis of VO_2 were calculated as 0.09%, 0.5% and 1.3% for the films deposited by 50 min, 25 min and 10 min, respectively. The *d*-spacing and strain of all the films are summarized in Table 5.1.

Table 5.1 Thicknesses of VO_2 thin films on 50 mtorr deposited AZO buffer layers, and the corresponding *d*-spacing and lattice strain along *c*-axis.

Dep. time (min)	VO_2 thickness (nm)	d-spacing (c-plane, nm)	lattice strain (%)
50	120	0.2271	+0.08
25	65	0.2280	+0.5
10	30	0.2298	+1.3

The microstructures of VO_2 thin films, especially the film thickness and VO_2/AZO interface, were further characterized by TEM. Figure 5.2(a)-(c) show the cross-section TEM images of VO_2 thin films with different deposition time. The AZO buffer layers have a similar thickness of around 20 nm for all the samples. The VO_2/AZO interfaces are smooth and clean, indicating minimal surface roughness for the 50 mtorr deposited AZO buffer layers and limited interaction between VO_2 and AZO. The VO_2 thicknesses are around 120 nm, 65 nm and 30 nm for the films deposited by 50 min, 25 min and 10 min. All the VO_2 films show columnar grain structures. The average grain width shows no obvious change with the layer thickness. In contrast to the VO_2 films directly deposited on *c*-cut sapphire substrates, the VO_2 films with AZO buffer layers show relatively clean contrast of grains without obvious 120 ° domain boundaries [101], indicating lower defects density in these films. Figure 5.2(d) and (e) are the SAED patterns of the 65 nm VO_2 sample, taken from the zone axes of Al_2O_3 $[\bar{1}010]$ and Al_2O_3 $[1\bar{2}10]$, respectively. The distinguished diffraction dots from the SAED patterns suggest a good epitaxial quality of the VO_2 films. The slightly arced diffraction dots of VO_2 indicate a minor mosaic rotation of the domains. Based on the SAED patterns, the out-of-plane matching relations are determined as VO_2 (002)//AZO (0002)//Al_2O_3 (0006). In the in-plane orientation, VO_2 and AZO have a domain lattice matching relationship with VO_2 (020) // AZO $(1\bar{1}00)$ and VO_2 (402) // AZO $(11\bar{2}0)$.

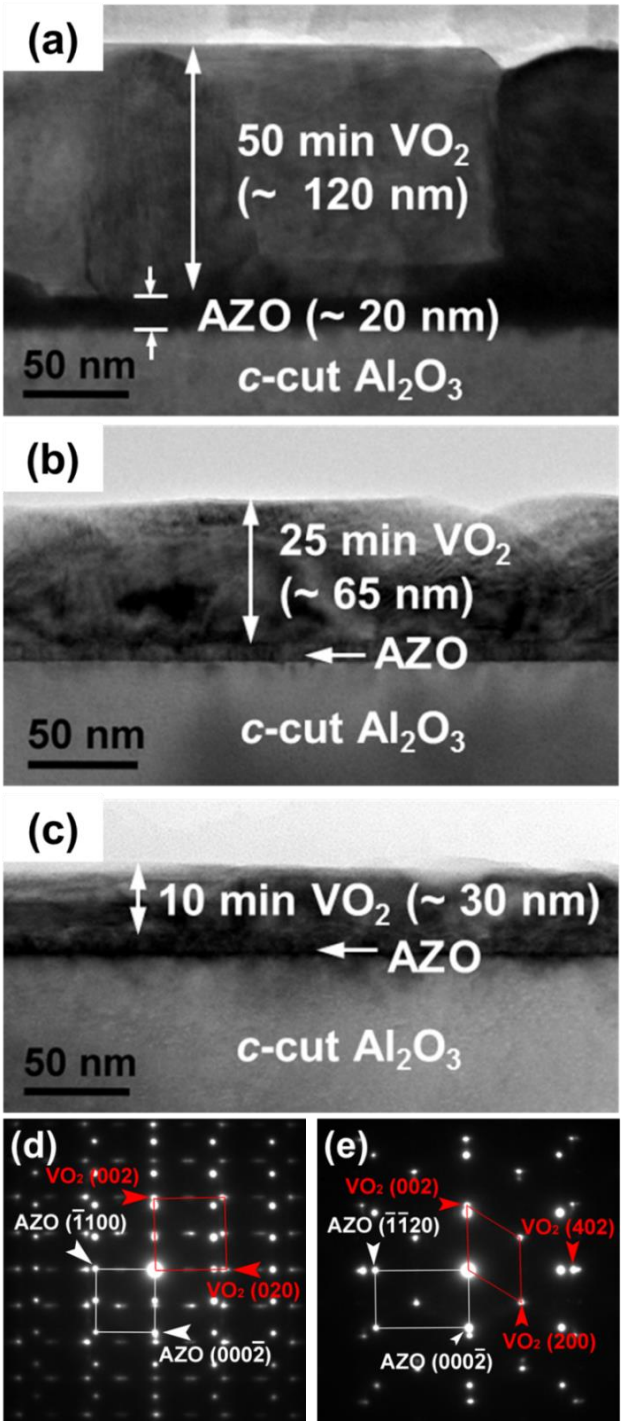

Figure 5.2 Cross-section TEM images of the VO_2 thin films on AZO buffered *c*-cut sapphire substrates with deposition time of (a) 50 min, (b) 25 min and (c) 10 min. The AZO buffer layers were all deposited at an oxygen pressure of 50 mtorr. (d) SAED pattern of the film with 65 nm VO_2 along the Al_2O_3 [$\bar{1}$010] zone. (e) SAED pattern of the film with 65 nm VO_2 along the Al_2O_3 [1$\bar{2}$10] zone.

The SMT properties of VO_2 films with different layer thicknesses were characterized by measuring the electrical resistivity change during phase transition. Figure 5.3(a) shows the schematics of the resistivity measurements. In order to get the resistivity of the individual VO_2 layers, six Au contacts were coated on each sample. The four contacts on the VO_2 film (marked as I+, I-, V+ and V-) were used for the film in-plane resistivity measurement. The two contacts on the AZO buffer layer were used to measure AZO resistivity. The VO_2 layer resistivity was then calculated by considering VO_2/AZO as two parallel resistors. Figure 5.3(b1)-(d1) show the normalized electrical resistivity, $\rho=\rho(T)/\rho(290K)$, of VO_2 thin films as a function of temperature. In order to determine the phase transition parameters, e.g. transition amplitude (ΔA), transition temperature (T_c), sharpness (ΔT) and the width of thermal hysteresis (ΔH) for each film, the derivation of $\log_{10}(\rho)$ has been calculated and plotted with respect to temperature, as shown in Figure 5.3(b2)-(d2). The plots show a clear peak position shift, indicating obvious T_c changing with VO_2 layer thickness. As summarized in Table 5.2, the T_c of VO_2 gradually decreases with the decrease of film thickness, which is attributed to the increase of film lattice strain. For 120 nm VO_2 film, the T_c is close to the bulk VO_2 transition temperature (341 K, 66.85 ℃) because of limited lattice strain. With the increase of strain, the 30 nm VO_2 film shows a T_c of 320.8K (47.6 ℃), much lower than the bulk T_c. The T_c of VO_2 films varying with lattice strain is plotted in Figure 5.3(e). Meanwhile, the ΔT slightly increases with the decrease of film thickness, indicating a tiny broadening of the transition. It could be related to the slightly increase of the overall defects density, such as dislocations and point defects, with the increase of film internal

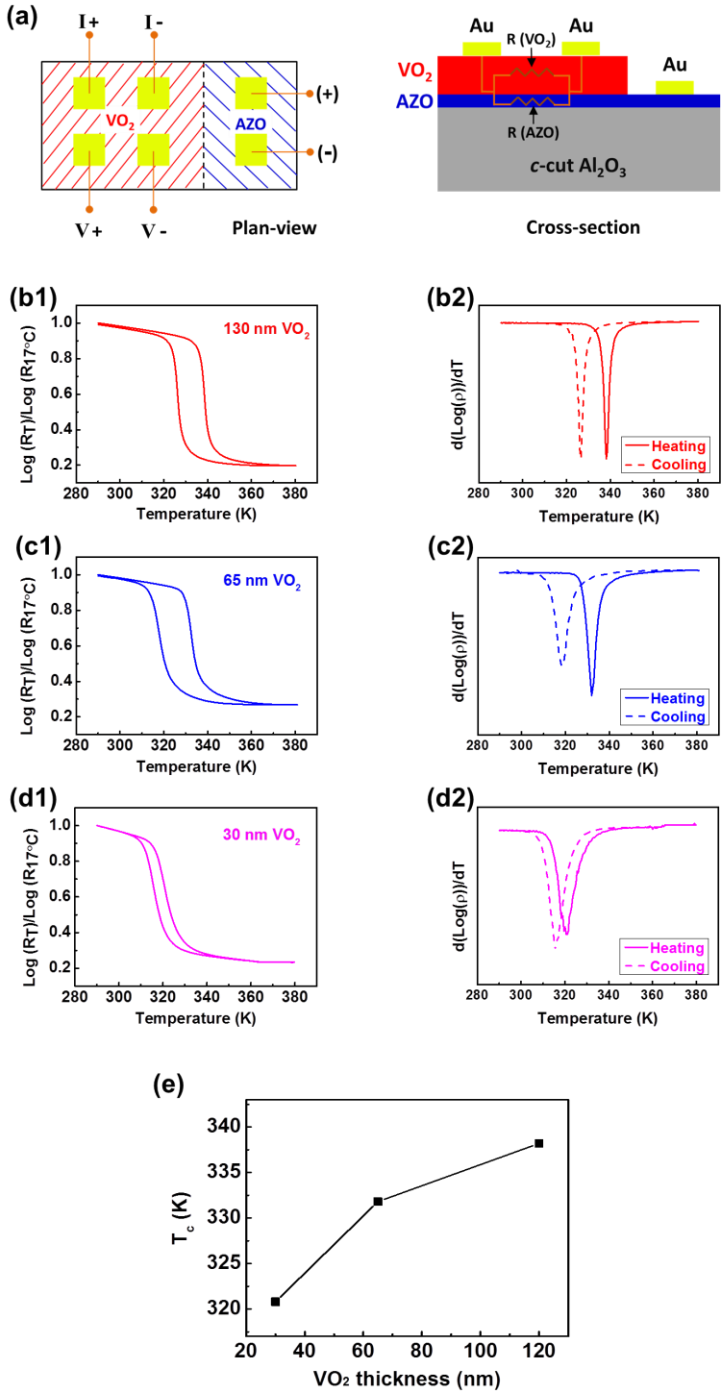

Figure 5.3 (a) Plan-view and cross-section schematics of the VO_2 electrical resistivity measurement set up. (b1)-(d1) Normalized resistivity of VO_2 films with different thicknesses as a function of temperature. (b2)-(d2) Resistivity changing rate of VO_2 films with different thicknesses. (e) The phase transition temperature as a function of VO_2 film thickness.

strain. Similar transition broadening due to additional defects and strain has been previously reported [37]. Despite of the broadening, the transition sharpness of these VO_2 films is still outstanding comparing to many of the VO_2 films with doping elements [31, 34, 255, 256]. The transition amplitude (ΔA) shows no significant change with the VO_2 thickness. It suggests that the increase of overall defects density has less influence on ΔA. In addition, the ΔH decreases with the VO_2 thickness, indicating a smaller thermal hysteresis of the thinner films. It could be related to that the thinner VO_2 films have less vertical grain boundaries, which contain less interfacial energies for switching as reported previously [37].

Table 5.2 SMT characteristics of VO_2 thin film with different layer thicknesses

VO_2 thickness (nm)	strain (%)	T_c (K)	ΔA	ΔT↑ (K)	ΔH (K)
120	+0.08	338.2	7800	2.6	11.6
65	+0.5	331.8	6600	4.5	13.0
30	+1.3	320.8	7200	8.3	5.3

The T_c tuning of VO_2 by varying film thickness is realized by the strain tuning of the VO_2 lattice. The film strain is introduced by the lattice mismatch between VO_2 and AZO. The strain continuously increases with the decrease of film thickness because of

more strain effects in thinner films [259]. It is noted that, with the VO_2 thickness variation, the films remain similar epitaxial qualities. Therefore, the strained buffer approach coupled with film thickness tuning provides a simple and straightforward approach to tune T_c continuously without significant deterioration of other STM properties.

5.4.2 T_c tuning by VO_2/AZO interface roughness

When the VO_2 film is grown on a rough AZO surface, the film growth is quite different from the smooth AZO cases discussed above. First, the VO_2 films could have lower epitaxial quality at the interface area, where the lattice matching between VO_2 and AZO plays a less significant role. Therefore the strain in the VO_2 film is not only dominated by the VO_2/AZO lattice mismatch but also influenced by the surface roughness of AZO buffer layers. In order to study the strain effects of VO_2/AZO interface roughness and its influence on the T_c and other SMT properties of VO_2, AZO buffer layers with different surface roughness conditions were synthesized on *c*-cut sapphire substrates under different oxygen partial pressures: 200 mtorr, 150 mtorr and 100 mtorr. The VO_2 films with similar thicknesses were then grown on these AZO buffer layers with the deposition time of 10 min.

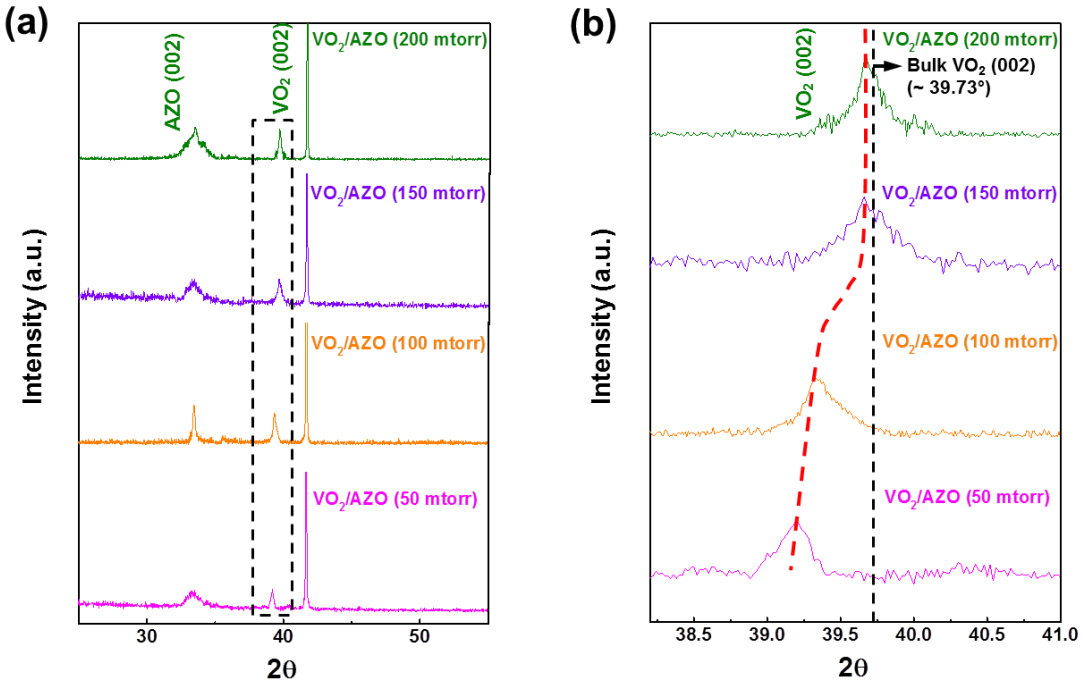

Figure 5.4 (a) The XRD θ-2θ spectra of 30 nm VO_2 thin films on AZO buffered *c*-cut sapphire substrates with the buffer layers grown under oxygen pressure of 200 mtorr, 150 mtorr, 100 mtorr and 50 mtorr. (b) Enlarged VO_2 (002) peaks of VO_2 thin films on different AZO buffer layers. The black dash line represents the bulk VO_2 (002) peak position.

Figure 5.4(a) shows the XRD θ-2θ scans of VO_2 thin films on AZO buffer layers deposited at 200 mtorr, 150 mtorr and 100 mtorr, respectively. The θ-2θ spectrum of VO_2 on 50 mtorr deposited AZO was replotted as a reference. The AZO (002) peak appears at ~33.5 ° for all samples, indicating that the oxygen pressure has limited influence on the doping level of Al in ZnO lattice. All the VO_2 films show primary peaks corresponding to monoclinic phase VO_2 (002), indicating that single phase VO_2 (M1) films texturing along *c*-axis were achieved in all samples. The similar intensity of VO_2

(002) peaks suggests a comparable quality of VO_2 films on different AZO buffer layers. The rectangular area marked in Figure 5.4(a), ranging from 38.2 ° to 41 °, is enlarged and shown in Figure 5.4(b). The black dashed line represents the bulk VO_2 (002) peak position (39.73 °). The shift of VO_2 (002) peaks indicates tensile strain along the *c*-axis for all the VO_2 films. The red dashed line shows that with the decrease of oxygen partial pressure during AZO buffer layer deposition, the peak position of VO_2 (002) gradually shifts to lower angle, indicating an increase of tensile strain in the VO_2 films along the *c*-axis. Based on the XRD results, the tensile strains along the *c*-axis of VO_2 were calculated as 0.10%, 0.15%, 0.93% and 1.3% for the films on AZO buffer layers deposited at 200 mtorr, 150 mtorr, 100 mtorr and 50 mtorr, respectively. The *d*-spacing and strain of all the VO_2 films were summarized in Table 5.3.

Table 5.3 The *d*-spacing and lattice strain (along *c*-axis) of VO_2 thin films on 200 mtorr, 150 mtorr, 100 mtorr and 50 mtorr deposited AZO buffer layers.

AZO growth pressure (mtorr)	d-spacing (c-plane, nm)	lattice strain (%)
200	0.2271	+0.1
150	0.2273	+0.15
100	0.2290	+0.93
50	0.2298	+1.3

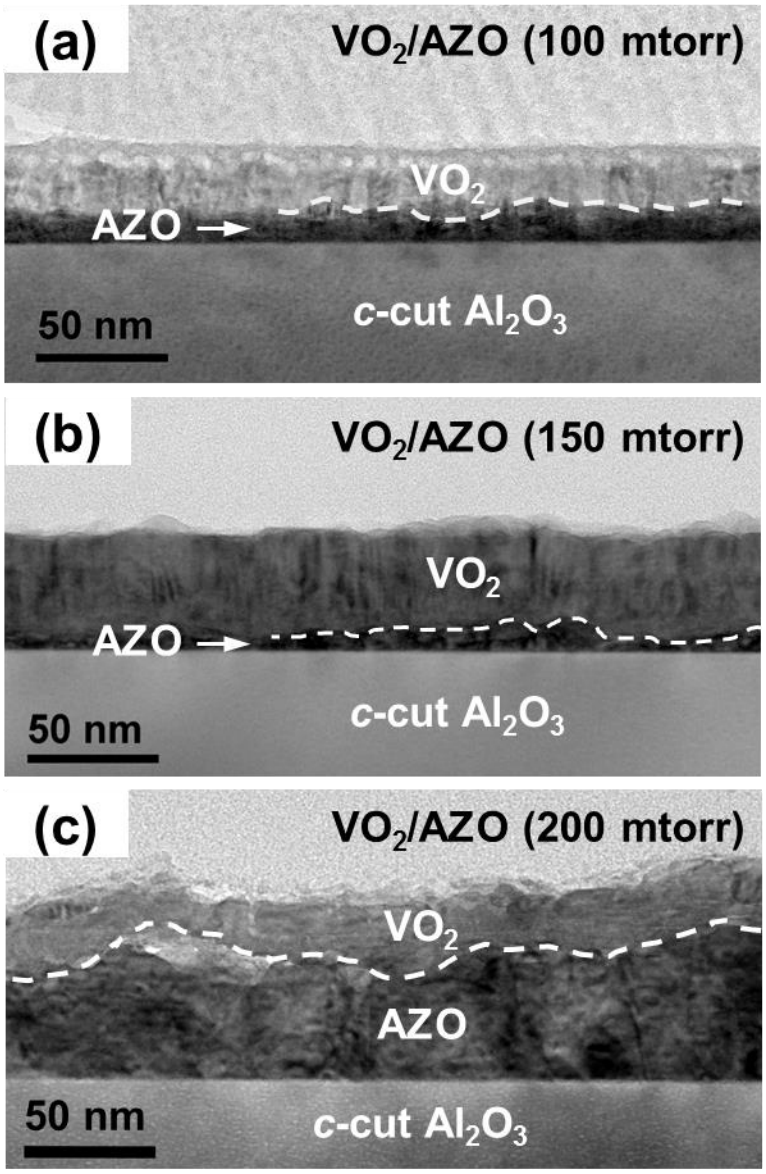

Figure 5.5 Cross-section TEM images of the VO_2 thin films on AZO buffered *c*-cut sapphire substrates with the buffer layers grown under oxygen pressure of (a) 100 mtorr, (b) 150 mtorr, and (c) 200 mtorr. The VO_2/AZO interfaces were marked by dash lines.

The microstructures of VO_2 thin films and AZO buffer layers were characterized by TEM. Figure 5.5 shows the cross-section TEM images of VO_2 thin films on different AZO buffer layers. The AZO buffer layers show very different surface roughness with different oxygen pressure during growth. The VO_2/AZO interfaces were marked by dash lines in the images. It clearly shows that the surface roughness of AZO increases with the increase of oxygen pressure. The AZO buffer layers deposited at 100 mtorr and 150 mtorr show a thickness of around 20 nm, comparable to the AZO deposited at 50 mtorr (Figure 5.2(c)). The AZO deposited at 200 mtorr has an average thickness of around 40 nm. Since it has the largest roughness, the increase of thickness could guarantee a full coverage of the sapphire substrate. The VO_2 films show a similar thickness of around 30 nm. They are all columnar grains with vertical grain boundaries. The VO_2 films have similar surface roughness as the AZO buffer layers, indicating uniform coverage of the AZO surfaces.

The SMT properties of VO_2 films on different AZO buffer layers were characterized by measuring the electrical resistivity change during phase transition. Figure 5.6(a1)-(c1) show the normalized electrical resistivity of VO_2 thin films as a function of temperature. Figure 5.6(a2)-(c2) plotted the derivation of $\log_{10}(\rho)$ with respect to temperature. Based on the plots, the SMT properties, i.e. T_c, ΔA, ΔT and ΔH were characterized for each film and summarized in Table 5.4. The SMT properties of the VO_2 film on 50 mtorr deposited AZO were also listed as a reference. The plots show that, with the decrease of buffer layer growth pressure, the VO_2 phase transition gradually shifts to lower temperatures. It means that more strain is introduced in the VO_2

film with the decrease of VO_2/AZO interface roughness, which leads to more significant shift of T_c. For the VO_2 film on 200 mtorr deposited AZO buffer layer, the T_c is around 337.2 K (64.0 ℃), close to the bulk T_c (341K, 67.84 ℃). With the decrease of VO_2/AZO interface roughness, the T_c decreases to 324.5 K (51.35 ℃) for the VO_2 on 100 mtorr deposited AZO buffer layer. The VO_2 film on 50 mtorr deposited AZO shows an even lower T_c owing to a smoother VO_2/AZO interface. The T_c of VO_2 films varying with buffer layer growth pressure is plotted in Figure 5.6(d). It is interesting that the T_c of VO_2 on 150 mtorr and 200 mtorr deposited AZO is close with each other, despite of the dramatic difference of the VO_2/AZO interface roughness shown in Figure 5.5. As both of the films have a T_c close to the bulk transition temperature, it suggests that the film strain is almost fully relaxed when the roughness of VO_2/AZO interface is beyond a threshold. The ΔA and ΔT are comparable for the VO_2 films on 50 mtorr and 100 mtorr deposited AZO. However the VO_2 films on 150 mtorr and 200 mtorr deposited AZO show an obvious drop of ΔA and increase of ΔT. It implies that with dramatic increase of the VO_2/AZO interface roughness, more defects could be introduced in the film. Meanwhile, the ΔH is in a comparable range for all the samples, which indicates that the buffer layer roughness has limited influence on the interfacial energies of the VO_2 film grain boundaries.

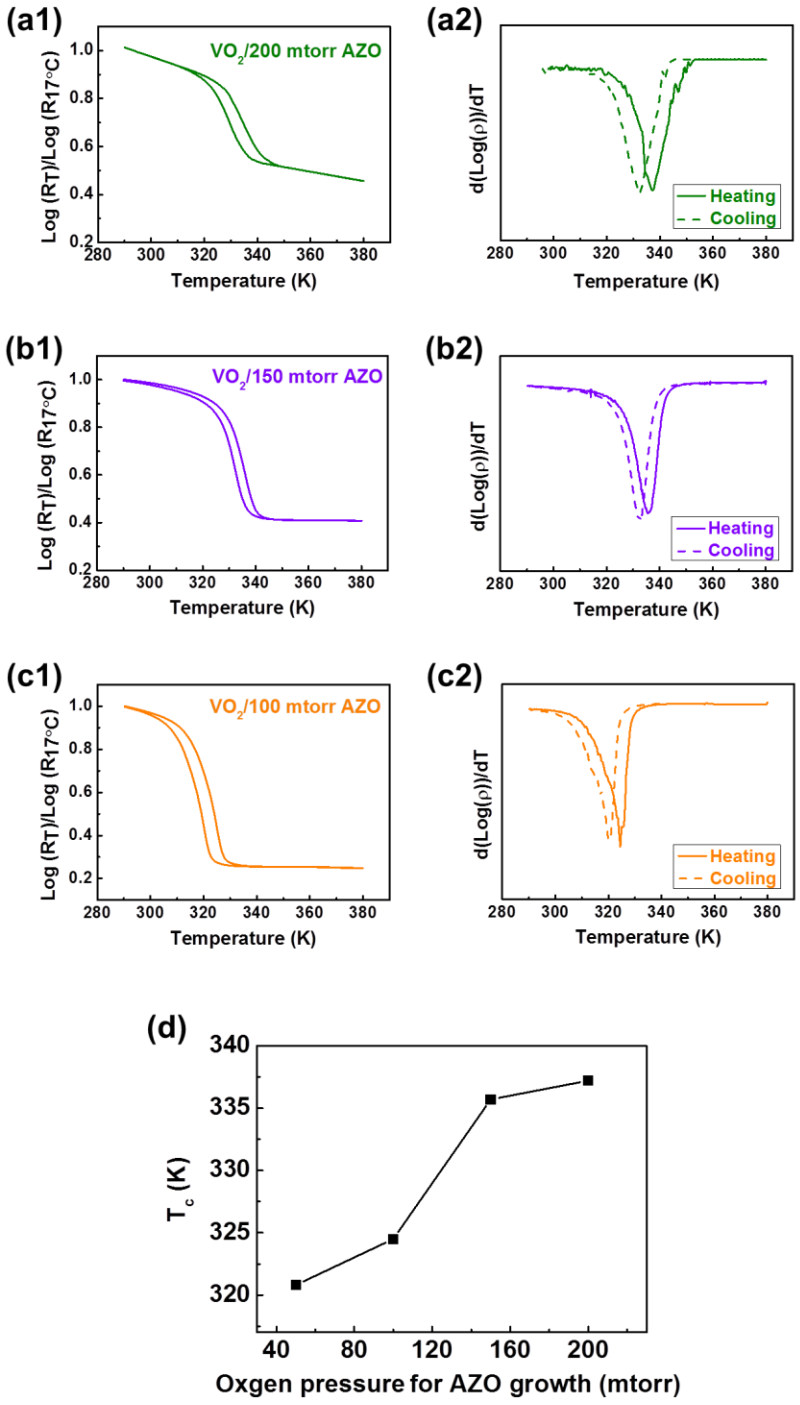

Figure 5.6 Normalized resistivity-temperature plots of VO_2 films on AZO buffer layers deposited under oxygen pressure of (a1) 200 mtorr, (b1) 150 mtorr and (c1) 100 mtorr. (a2)-(c2) The corresponding resistivity changing rate of VO_2 films on different AZO buffer layers. (d) The phase transition temperature of VO_2 as a function of AZO buffer layer growth oxygen pressure.

Table 5.4 SMT characteristics of VO_2 thin film on AZO buffer layers deposited under different oxygen pressures.

AZO growth pressure (mtorr)	VO_2 strain (%)	T_c (K)	ΔA	ΔT↑ (K)	ΔH (K)
200	+0.1	337.2	3200	11.1	4.9
150	+0.15	335.7	4600	9.1	3.5
100	+0.93	324.5	6800	8.4	5.1
50	+1.3	320.8	7200	8.3	5.3

5.4.3 Discussion

For both of the above two cases, i.e. VO_2 thickness change and VO_2/AZO interface roughness variation, the T_c tuning was achieved by VO_2 lattice strain control. In the stress-temperature phase diagram of VO_2, the relationship between the transition temperature T_c and the uniaxial stress σ is calculated based on the Clausius-Clapeyron equation,

$$dT_C/d\sigma = (\varepsilon_0 T_C^0)/\Delta H \quad (5.1)$$

where σ is the stress along *c*-axis of M1 phase VO_2 (*a*-axis of R phase VO_2), T_C^0 is the transition temperature without stress (~68 ℃ for VO_2), ΔH is the latent heat of the transition, and ε_0 is a coefficient [106]. Based on this theory calculation, the increase of tensile strain along *c*-axis of VO_2 leads to a decrease of T_c, which agrees with the above experimental results. For epitaxial VO_2 films, the lattice strain is mainly dominated by VO_2/AZO lattice mismatch. Figure 5.7 shows the atomic modeling of the VO_2/AZO interface coupling. The AZO lattice parameters were set on the basis of the XRD results.

The red and blue ball symbols represent the locations of vanadium and zinc atoms in the lattices, respectively. The unit cells are marked by the dashed blue frames. It can be noted that along both the *a*- and *b*-axis of VO_2, the *d*-spacing of AZO is much smaller than that of VO_2. Therefore, compressive strain will be introduced in both *a*- and *b*-axis of VO_2 when it matches on top of AZO. In order to sustain the volume of the unit cell, tensile strain will then be introduced in the *c*-axis of VO_2, as observed in the XRD results. The strain effect of AZO buffer layers decreases with the distance from the interface [259]. Therefore, with the increase of VO_2 film thickness, the lattice mismatch strain is gradually relaxed, which leads to a close-to-bulk T_c in the 120 nm VO_2.

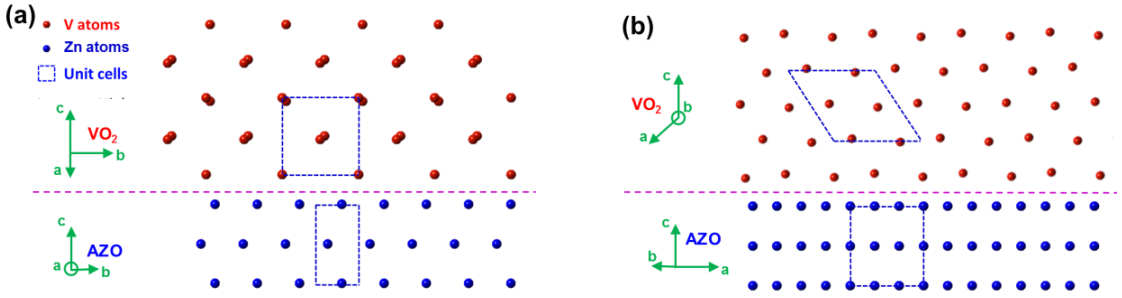

Figure 5.7 Atomic modeling of the VO_2/AZO interface coupling along (a) AZO [11$\bar{2}$0] zone and (b) AZO[1$\bar{1}$00] zone. The red and bule ball symbols represent the locations of vanadium and zinc atoms in the lattices, respectively. The unit cells are marked by the dashed blue frames.

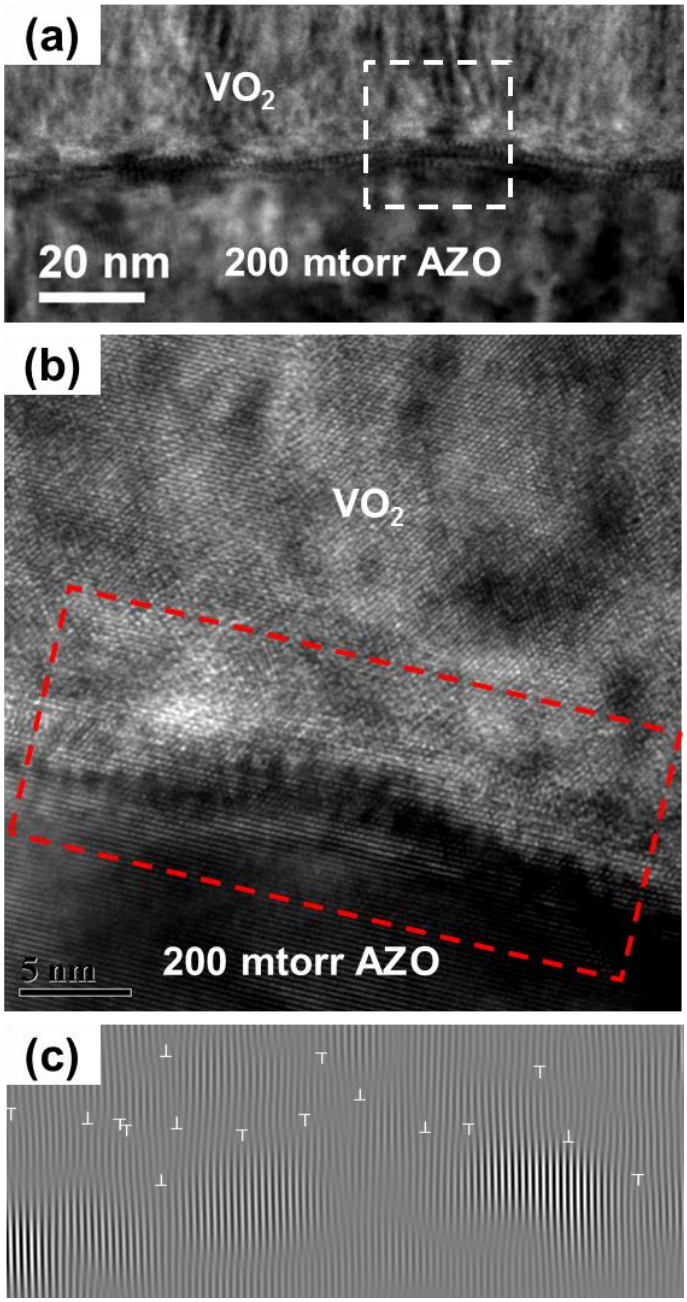

Figure 5.8 (a) High magnification TEM image of the interface of VO_2 on 200 mtorr deposited AZO. (b) HR-TEM image of the squared area in (a). The strain is localized within 8 nm region around the interface. (c) IFFT of the strained area by selecting the diffraction dots of AZO ($1\bar{1}00$).

For the VO_2 films on rough AZO surfaces, the XRD results show a strain relaxation with the increase of AZO surface roughness. Figure 5.8(a) shows a high resolution image of the interface of VO_2 on 200 mtorr deposited AZO. The interface region shows a darker contrast compared to other areas, indicating a high strain around the interface. The HR-TEM image of the squared area is shown in Figure 5.8(b). It suggests that the highly strained area is localized within ~8 nm region around the interface, 5 nm on the VO_2 side and 3 nm on the AZO side. The inverse Fast Fourier Transform (IFFT) was performed on the strained area, as shown in Figure 5.8(c). The diffraction dots of AZO ($1\bar{1}00$) were selected for the IFFT. High density dislocations can be observed in this area. It suggests that for the VO_2 on a rough AZO surface, the lattice mismatch strain is relaxed by the generation of dislocations in the region close to the interface. Thus most of the VO_2 lattices could remain almost strain free, which leads to a close-to-bulk T_c of the overall film, such as the VO_2 on 150 mtorr and 200 mtorr deposited AZO.

Based on the SMT property characterizations in this work, during the T_c tuning of VO_2, the transition amplitude of the films shows a maximum degradation of around 2 times, while the transition sharpness exhibits a maximum broadening of 8.5 K. Comparing to the T_c tuning with doping elements, this strain induced T_c tuning leads to less degradations of the phase transition amplitude and sharpness, and even results in the reduction of the thermal hysteresis. The dopants in the VO_2 films usually cause broken bonds in the VO_2 lattice and generate intrinsic strained areas around the elements [209]. Furthermore, dopants and the corresponding oxide compounds could form clusters in the

VO_2 films with high doping levels, which could result in significant degradations of the film SMT properties [211]. In contrast, the substrate and buffer layer induced strain applies on the entire VO_2 films, and thus introduces fewer defects in the films. The misfit dislocations are mainly concentrated near the interface areas, which has less effects on the overall film properties. Therefore, the VO_2 SMT properties, i.e. phase transition amplitude, sharpness, and thermal hysteresis, are better maintained during the T_c tuning via strain variation.

5.5 Conclusion

In summary, we have demonstrated two simple and effective approaches in tuning the T_c of VO_2 films using AZO buffers. One is to couple film thickness and the strain effect from AZO buffer. Epitaxial VO_2 thin films with thickness of 120 nm, 65 nm and 30 nm were deposited on AZO buffered *c*-cut sapphire substrates by PLD. The second approach is to tune the film strain by AZO buffer surface roughness. The oxygen pressures for AZO buffer layers growth were varied from 50 mtorr, 100 mtorr, 150 mtorr, to 200 mtorr to achieve different surface roughness. Through these two approaches, the T_c of VO_2 films was continuously tuned from 338.2 K (65.05 ℃) to 320.8 K (47.65 ℃). With the decrease of VO_2 thickness or VO_2/AZO interface roughness, tensile strain increases along the *c*-axis of VO_2 lattice, which leads to the decrease of T_c. No significant degradation of other SMT properties, i.e. ΔA, ΔT and ΔH, has been observed. The strain in the VO_2 thin films was mainly generated by the lattice mismatch between VO_2 and AZO. With the increase of VO_2/AZO interface roughness, the VO_2 film strain

was gradually released by generating high density of dislocations around the interface area. This study provides two effective approaches to tune the T_c of VO_2 thin films continuously with minimal impacts on the other SMT properties, which could make VO_2 a step further toward its practical applications in devices.

CHAPTER VI

PHASE TRANSITION STABILITY OF VO_2 THIN FILM ON *C*-CUT SAPPHIRE SUBSTRATE PROBED BY *EX SITU* AND *IN SITU* HEATING STUDIES

6.1 Overview

Epitaxial vanadium dioxide (VO_2) thin films have been deposited on *c*-cut sapphire substrate by pulsed laser deposition. The stability of the semiconductor-to-metal phase transition (SMT) properties with multiple thermal cycles has been investigated. The film shows the broadening of transition sharpness (ΔT) and width of thermal hysteresis (ΔH) after 30 cycles. *In situ* transmission electron microscopy (TEM) heating studies reveal that the film contains high density 120° domain boundaries. During thermal cycles, large strain was accumulated around the domain boundaries, which was correlated with the phase transition induced lattice constant change and the thermal expansion. It suggests that the degradation of domain boundary structures in the VO_2 films caused the transition property reduction (e.g., the decrease of ΔT and ΔH), but also played an important role to prevent the film from fracture during thermal cycles.

6.2 Introduction

Vanadium dioxide (VO_2) single crystal is known to exhibit an ultrafast (within 0.1 ℃) and reversible phase transition from a semiconductor phase to a metallic phase (SMT) at ~68 ℃ during heating process [5, 6, 45]. Through such a first-order phase

transition [6], VO_2 transits from a monoclinic phase ($P2_1/c$) to a tetragonal rutile phase ($P4_2/mnm$) [7], accompanied with significant changes in the electrical [8-10] and optical properties [11-13]. Owing to the fascinating characteristics, VO_2 shows great potential in various devices including gas sensors [14], electrical switches [15], thermochromics [137], thermal actuators [17], and memory devices [18], and thus has attracted extensive research interests.

To enable practical device applications of VO_2, it is desired to have high stability during multiple cycles of phase transitions. The SMT process is accompanied with a strain change in the VO_2 lattice, which is caused by the lattice constant difference between two phases. The bulk VO_2 was reported to have poor ductility (<0.2%) [77]. Therefore during multiple thermal cycles, it showed a degradation of the SMT properties because of the strain generated micro-cracks [260]. In contrast, the nanostructured VO_2 was reported to have much higher capability to sustain strain. Among all, the VO_2 thin films have attracted particular interest because of the 2-dimentional geometry and the compatibility with current device manufacture. However, the stability of the SMT properties of VO_2 thin films is still under investigation. Especially, the previous reports showed quite different results on the stability of different VO_2 thin films. In 1996, Guzman *et al.* reported that the SMT behaviors of the sol-gel synthesized VO_2 films were still maintained after 10^8 cycles of current-voltage induced Joule heating [261]. Ko *et al.* then reported a consistent result, in which the sputtered polycrystalline VO_2 thin films showed no obvious degradation of the SMT properties up to successive 102 thermal cycles [262]. However, Crunteanu *et al.* showed that the transition amplitude of

the pulsed laser deposition (PLD) prepared VO_2 thin films had a decrease of ~20dB after multiple cycles of electrical field induced phase transitions [133]. Moreover, Balakrishnan *et al.* reported the fractures of VO_2 thin films deposited on Si_3N_4 substrates during the phase transition processes, which resulted in a large degradation of the SMT properties [228]. These studies indicated that the stability of VO_2 thin films could be highly dependent on the synthesis processes and the film microstructures.

The *c*-cut sapphire substrate is one of the most commonly used substrates for epitaxial VO_2 film growth [28]. In this work, we reported the first phase transition stability study on the VO_2 thin films grown on *c*-cut sapphire substrates. Electrical resistance measurements were conducted on the VO_2 thin films to characterize the SMT property changes with multiple thermal cycles. *In situ* TEM heating experiments were then conducted to investigate the film microstructure evolutions during phase transition cycles. The SMT property variations were correlated with the strain effects at the domain boundaries of the VO_2 films.

6.3 Experimental

VO_2 thin films on *c*-cut sapphire substrates were grown by a pulsed laser deposition (PLD) system (KrF laser, 248 nm). The laser beam was focused to obtain an energy density of approximately 3 J/cm^2 at a 45 ° angle of incidence. A V_2O_5 target, obtained by conventional powder pressing and sintering method, was used as the material source for VO_2. Monoclinic phase VO_2 was achieved by optimizing substrate temperature to 600 ℃ and oxygen pressure at 10 mTorr. The depositions were conducted

at a laser repetition rate of 10 Hz and duration of 10 mins. The microstructures of the as-deposited films were characterized by X-ray diffraction (XRD) using a PANalytical Empyrean 2 X-ray diffractometer with Cu K_α radiation. The electrical resistance of the VO_2 films were measured by a standard four probe method with temperature varied from 17 ℃ (290 K) to 97 ℃ (370 K) for 30 cycles in a physical property measurement system (PPMS, Quantum Design). Detailed cross-section microstructural characterization including transmission electron microscopy (TEM) images and selected-area diffraction (SAD) patterns were acquired by JEOL 2010 analytical microscope with a point-to-point resolution of 0.23 nm. The *in situ* TEM heating experiments were conducted using an *in situ* heating holder manufactured by Gatan Inc.

6.4 Results and discussion

Figure 6.1 shows the XRD θ-2θ scan of the VO_2 thin film on *c*-cut sapphire substrate. A primary peak appears at ~40.0 °, which corresponds to monoclinic phase VO_2 (002). This peak is slightly shifted to higher angle compared to the bulk VO_2 (002) peak position (39.73 °), indicating a compressive strain along the *c*-axis of the VO_2 film. The sharp width of the peak indicates that the VO_2 film has grown highly textured along *c*-axis. No extra film peaks are observed in the θ-2θ scan, which suggests a high purity and single phase of the film.

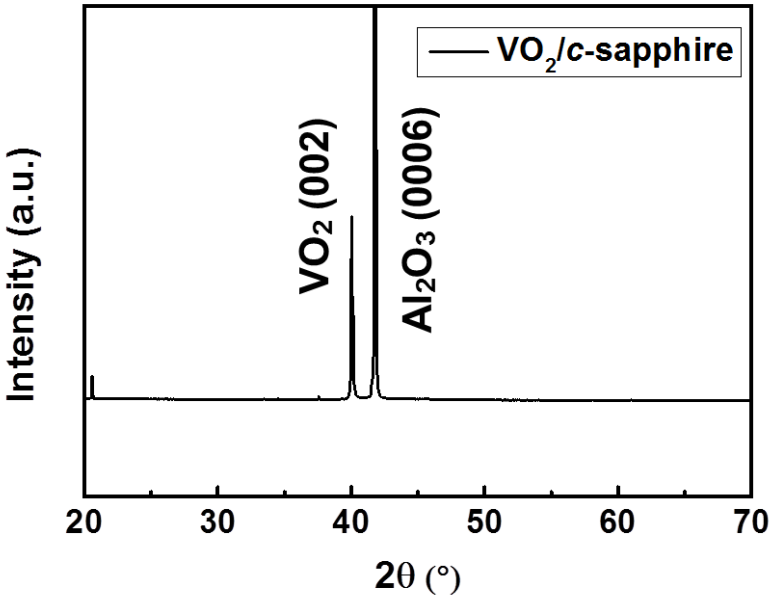

Figure 6.1 XRD θ-2θ spectra of the VO_2 thin film on *c*-cut sapphire substrate.

The SMT properties of the VO_2 thin film were characterized by measuring the electrical resistance changes during phase transitions. Totally 30 thermal cycles were applied on the film. During each cycle, the temperature was varied from 17 ℃ (290 K) to 97 ℃ (370 K) as a loop. Figure 6.2(a) shows the normalized electrical resistance, ρ=R (T)/R (17 ℃), of VO_2 thin film at the 1st and 30th cycle as a function of temperature. The 1st cycle of the film phase transition shows an electrical resistance switching of about 6000 times. Very limited change of the phase transition amplitude (ΔA) is observed after 30 thermal cycles. In order to determine the other SMT parameters, e.g. transition temperature (T_c), sharpness (ΔT) and the width of thermal hysteresis (ΔH) for the film,

the derivation of $\log_{10}(\rho)$ has been calculated and plotted with respect to temperature, as shown in Figure 6.2(b) and (c). At the first cycle, the film shows a T_c of 75.7 ℃ during heating process. The T_c shifts to higher temperature compared to bulk VO_2 (68 ℃), which was commonly reported for VO_2 films on *c*-cut sapphire. It is mainly caused by the film/substrate lattice mismatch induced strain. During the 1st cycle, the phase transition shows a relatively sharp ΔT of ~6.3 ℃ and a narrow ΔH of ~7.4 ℃. After 30 cycles of phase transition, as shown in Figure 6.2(c), the T_c slightly decreases to 73.4 ℃, possibly because of the relaxation of lattice misfit strain by thermal treatment. Compared to the 1st cycle, the 30th transition cycle shows a much broader ΔT of ~12.3 ℃ and a much wider ΔH of ~11.5 ℃. The changes of ΔT and ΔH with the cycling numbers are plotted in Figure 6.2(d). Both of their values increase with the cycling numbers. These results demonstrate that the VO_2 film has a degradation of the SMT behaviors, especially the transition width and thermal hysteresis, but maintains the transition amplitude after multiple cycles of phase transitions. More interestingly, the ΔT and ΔH show higher increasing rates at the first several thermal cycles and then increase slower after 15-20 cycles, indicating a saturation mechanism of the degradation of SMT properties.

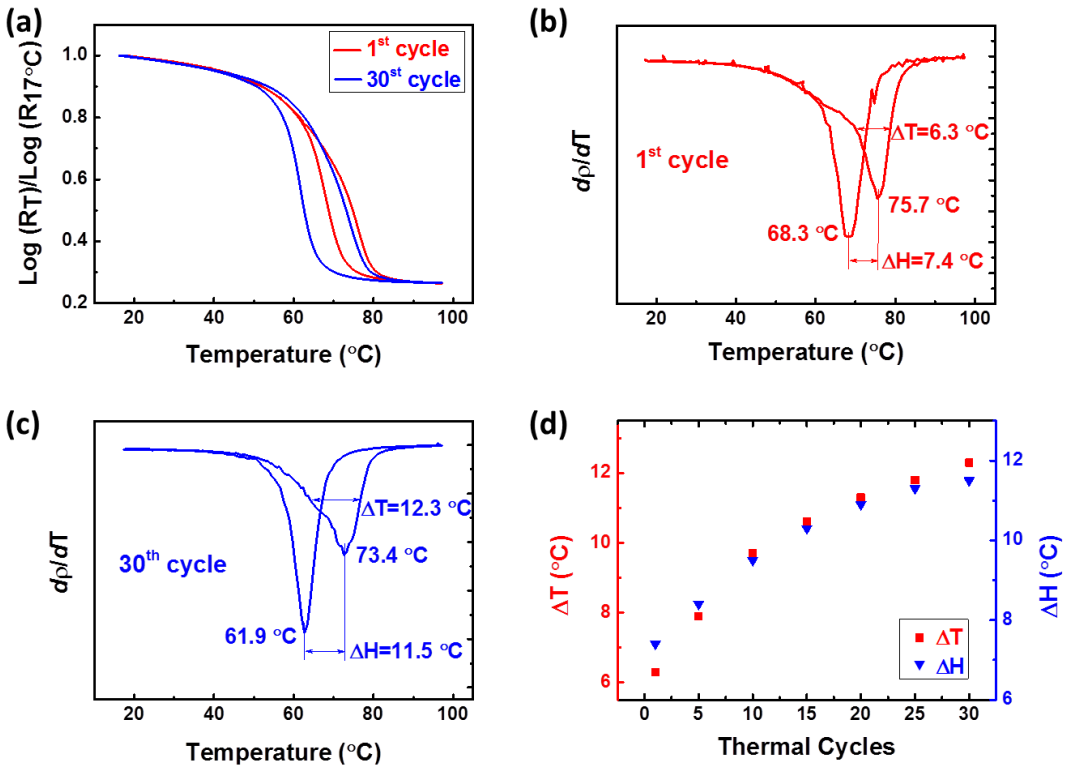

Figure 6.2 Phase transition properties of the VO_2 thin film on *c*-cut sapphire substrates. (a) Normalized resistance change of the film at the 1st and 30th thermal cycles as a function of temperature. (b)-(c) Resistance changing rate of the VO_2 film at the 1st and 30th thermal cycles. (d) The phase transition sharpness and width of thermal hysteresis as a function of cycling numbers.

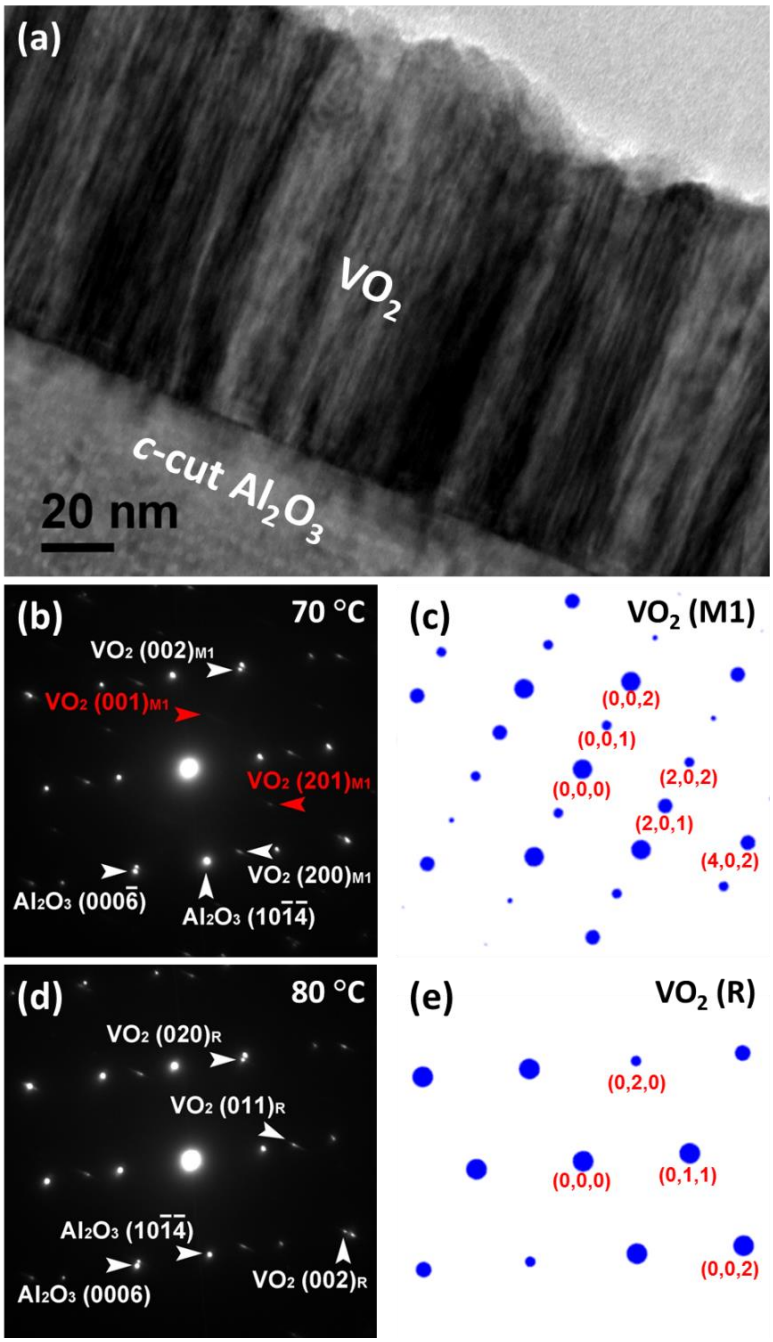

Figure 6.3 (a) Cross-section TEM image of the VO_2 thin film on *c*-cut sapphire substrate before thermal cycling. (b) SAD pattern of the film and substrate along the Al_2O_3 $[1\bar{2}10]$ zone at the specimen temperature of 70 ℃. (c) Simulated electron diffraction pattern of the monoclinic phase VO_2 along the zone axis of [020]. (d) SAD pattern of the film and substrate along the Al_2O_3 $[1\bar{2}10]$ zone at the specimen temperature of 80 ℃. (e) Simulated electron diffraction pattern of the tetragonal rutile phase VO_2 along the zone axis of [200].

In order to investigate the mechanisms of the VO_2 SMT property degradation, *in situ* TEM heating experiments were conducted on the as-deposited sample. Figure 6.3(a) shows the bright field TEM image of the VO_2 thin film on *c*-cut sapphire substrate before the 1st thermal cycle. The film shows a thickness of around 120 nm. It contains high density of ultrafine columnar domains with the width of about 5 nm. These domains are induced by the three-fold symmetry of the sapphire (0006) plane and form 120 ° boundaries with each other. Most of the domains have clear boundaries with coherent connection to the nearby domains, which indicates low interfacial strains around the domain boundaries. The different contrast throughout the film implies a non-uniform distribution of the substrate induced strain in the film. Figure 6.3(b) shows the SAD pattern of the film and substrate at an elevated temperature of 70 ℃. It was taken from [020] zone of VO_2 ([$1\bar{2}10$] zone of *c*-cut sapphire). The SAD pattern suggests a good epitaxial quality of the VO_2 film. The slightly arced diffraction dots of VO_2 indicate the slight misorientation of the domains. Based on the SAD pattern, it can be determined that in the out-of-plane orientation, VO_2 (002) is parallel to Al_2O_3 (0006), and in the in-plane orientation, VO_2 (200) is parallel to Al_2O_3 ($10\bar{1}2$) with a 3:2 domain matching relationship.

It is very difficult to distinguish the phase transition of VO_2 by TEM imaging because the transition process is accompanied with just a small amount of lattice change. Therefore, the SAD patterns were used to identify the phase transition processes. The electron diffraction theory indicates that the monoclinic lattice has strong higher-order Laue zone (HOLZ) reflections of the electron beam, which results in secondary

diffraction dots in the diffraction patterns. Figure 6.3(c) shows the simulation result of the monoclinic VO_2 electron diffraction pattern. It shows secondary diffractions at VO_2 (001), (201), etc. These secondary diffraction dots are also observed in the experimental result in Figure 6.3(b) (marked by red arrows), which further confirms the monoclinic phase of the VO_2 film at low temperatures. With the increase of temperature on the TEM holder, the intensity of the secondary diffraction dots gradually decreases and finally disappears at a temperature close to 80 ℃, as shown in Figure 6.3(d). The SAD pattern in Figure 6.3(d) matches well with the simulated diffraction pattern of the tetragonal rutile VO_2 shown in Figure 6.3(e). It indicates a complete phase transition of the VO_2 film within 10 ℃, which is consistent with the *ex situ* electrical measurement results.

In Figure 6.4(a), a significant change of the film microstructures can be observed after 5 cycles of phase transitions. The non-uniform contrast of the film is reduced, indicating a relaxation of the substrate induced strain in the lattice. However, the domain boundaries become much thicker with large contrast difference from nearby areas. It suggests that large strains are accumulated around the domain boundaries after multiple thermal cycles. The SAD pattern in Figure 6.4(b) shows more concentrated film diffraction dots compared to the pattern before 1st cycle (Figure 6.3(b)), indicating an increase of domain texturing quality after thermal treatment. The intensity of the secondary diffraction dots in the SAD pattern starts to decrease at around 65 ℃. However, they still exist after 10 ℃ of temperature increase, as shown in Figure 6.4(c), indicating an incomplete phase transition of the film. Moreover, when the temperature keeps increase to 85 ℃, the diffraction dot corresponding to VO_2 ($\bar{2}0\bar{1}$) can still be

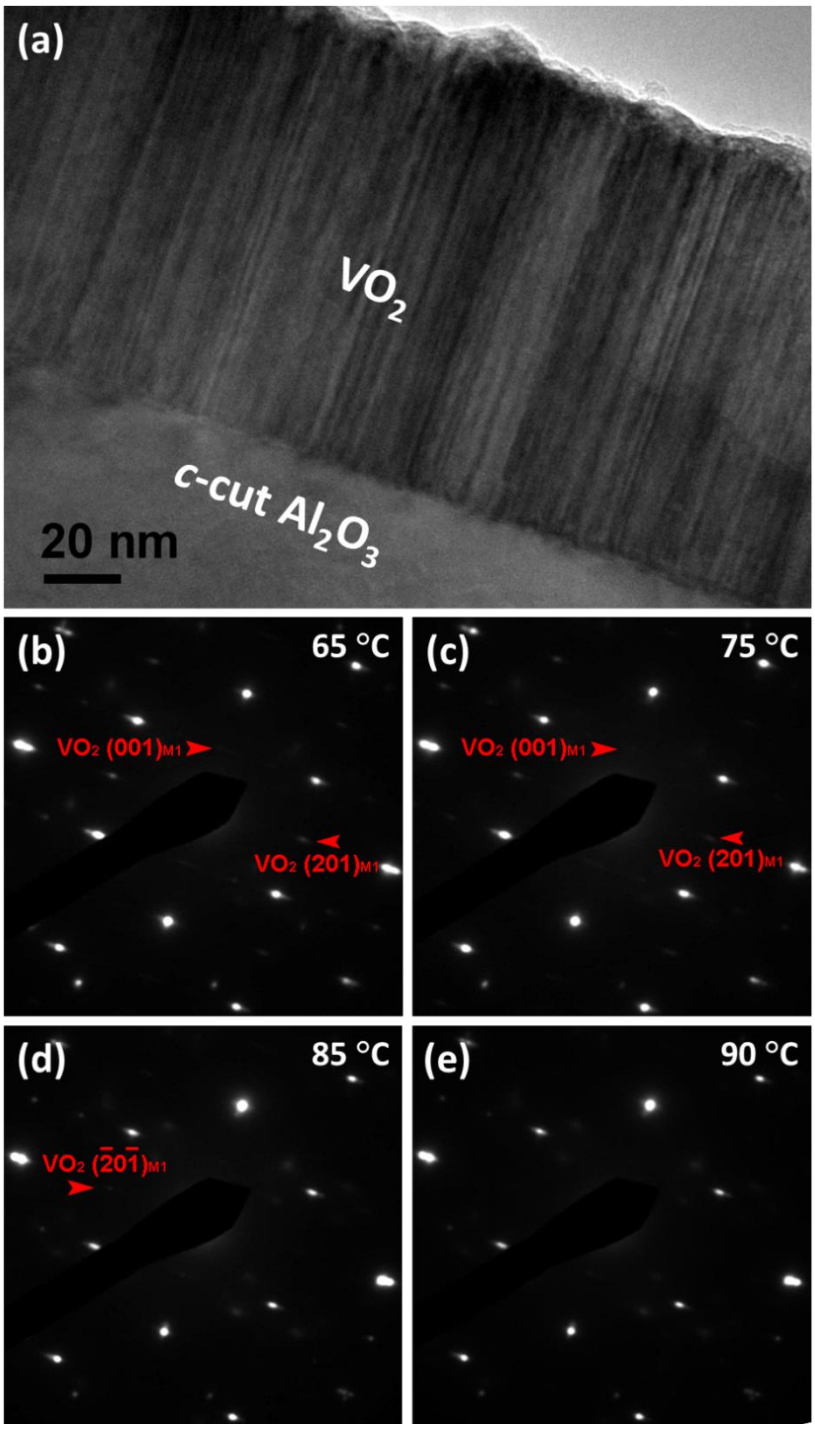

Figure 6.4 (a) Cross-section TEM image of the VO_2 thin film on *c*-cut sapphire substrate after 5 cycles of phase transitions. (b)-(e) SAD pattern of the film and substrate along the Al_2O_3 [$1\bar{2}10$] zone at the specimen temperature of 65 ℃, 75 ℃, 85 ℃ and 90 ℃, respectively. Secondary diffraction dots from monoclinic VO_2 completely disappear at 90 ℃.

observed, as shown in Figure 6.4(d). The low intensity of the dot implies the small amount of the existing monoclinic phase VO_2. The phase transition process is fully accomplished at a temperature close to 90 ℃, as shown in Figure 6.4(e), where no secondary diffraction dots are observed any more. The result of the 5^{th} cycle *in situ* heating experiment shows a phase transition process lasts for over 20 ℃, which is much wider than the 1^{st} transition cycle. This result is consistent with the *ex situ* electrical measurement and the ΔT broadening is more obvious, which could be because the small size of the TEM specimen.

Based on the lattice matching relationship, the monoclinic VO_2 has a lattice misfit of ~2.6% along the [200] direction with the sapphire substrate. This leads to a compressive strain along the *a*-axis and results in the increase of T_c of the as-deposited VO_2 film. During thermal cycles, the heat treatment leads to the strain relaxation by slightly reorganizing the domain orientations, which contributes to the slightly decrease of T_c.

As observed in Figure 6.4, with the multiple thermal cycles, large strain is accumulated around the domain boundaries in the VO_2 thin films. The strain accumulation could mainly be caused by the phase transition. The VO_2 phase transition is described as a martensitic transformation [23], during which nano-size tetragonal phase nuclei emerge from the monoclinic host and increase in numbers and sizes to form a percolating transition [112, 155]. Meanwhile, the VO_2 exhibits ~1% of lattice constant change when transit from the monoclinic phase to tetragonal phase. Therefore, when the tetragonal nuclei are formed in the matrix, the strain will be generated around the phase

boundaries. Furthermore, with the growth of the tetragonal nuclei, the strain will propagate together with the phase boundaries. The previous *in situ* TEM heating experiments conducted by Beteille *et al.* revealed that in polycrystalline VO_2 film, each grain exhibited the phase transition independently, without any collective transformation through the film [38]. Thus for the VO_2 film on *c*-cut sapphire substrate, the domains could undergo phase transition processes independently. Based on this hypothesis, tetragonal phase nuclei are formed in each individual domain during the thermal cycles, introducing strain inside the domain. Then with the completion of phase transition of the entire domain, the strain finally propagates to the domain boundaries. In addition, the thermal expansion of VO_2 could also introduce strain in the domain boundaries. The VO_2 was reported to have a large anisotropy of the thermal expansion [263]. As each domain has different orientations, the misfit of the thermal expansion coefficients will generate interfacial strain with temperature variations.

The strain accumulated around the domain boundaries is believed as the main reason that caused the broadening of ΔT and ΔH. Based on the stress-temperature phase diagram of VO_2, the strain around the domain boundaries will result in the shift of the VO_2 phase transition temperature. As the strain at each boundary is different and gradually decreases towards the inside of the domain, it will spread the phase transition temperature of VO_2 to a wider range and lead to the broadening of ΔT. As observed in the *in situ* heating process of the 5^{th} cycle, some parts of the film start to transit to tetragonal phase at the temperature as low as 65 ℃, while some particular areas remain in monoclinic phase at the temperature as high as 85 ℃. The ΔH was reported to be

related with the interfacial energy of boundaries in the VO_2 film. With the accumulation of the strain at the domain boundaries, their interfacial energies are increased, which results in the increase of the thermal hysteresis width. The strain at the domain boundaries could be generated more significantly within the first several thermal cycles because of the initial low strain status of the film. Therefore, more rapid degradations of the ΔT and ΔH are observed in the first 15 thermal cycles of the *ex situ* electrical measurements.

The phase transition amplitude (ΔA) is impacted by several factors. With the thermal treatment, the VO_2 film gets more epitaxial by reorganization of the domains, which will result in the increase of ΔA. On the other hand, the strain at domain boundaries could generate more defects including point defects and dislocations, and therefore will lead to the decrease of ΔA. As a combination result of these effects, the ΔA was observed to be almost stable throughout the 30 cycles of phase transitions in this study.

Despite that the domain boundaries in the VO_2 film caused the degradation of SMT behaviors, they actually provided an effective way to accommodate the thermal and phase transition induced strain. For the VO_2 film with very low boundary density, such as the VO_2 film on Si_3N_4 reported by Balakrishnan *et al.*, micro-cracks could easily be generated during phase transition cycles because of the poor ductility of VO_2 single crystals [228]. Therefore the boundaries actually play an important role to sustain the strain and protect the film from fracture. Optimized boundary densities are desired in the VO_2 films to balance between the phase transition stability and the failure of the film.

6.5 Conclusion

In conclusion, epitaxial VO_2 thin film was deposited on *c*-cut sapphire substrate by PLD. The SMT properties were characterized throughout 30 thermal cycles. The film maintains high transition amplitude (ΔA~6000) but exhibits the degradations of the transition width and thermal hysteresis with cycling numbers, where ΔT increases from 6.3 ℃ to 12.3 ℃ and ΔH increases from 7.4 ℃ to 11.5 ℃ after 30 cycles. Moreover, the degradations of the ΔT and ΔH are more rapid within the first 15 cycles. *In situ* TEM heating studies revealed that the film contains high density of domain boundaries, around which large strain is accumulated during thermal cycles. The strain accumulation, which could be caused by the phase transition induced lattice constant change and the film thermal expansions, is correlated with the degradations of ΔT and ΔH. Despite of that, the boundaries actually provide an effective way to accommodate the strain generated during thermal cycles and thus protect the film from failure. This study provides fundamental understandings of the SMT property degradation as well as the strain accommodation mechanisms of the VO_2 thin films, and thus presents a guide for the high stability VO_2 films for future device applications.

CHAPTER VII

SUMMARY

In this dissertation, the VO_2 thin film phase transition properties were systematically investigated and correlated with the film microstructures and strain status.

First, VO_2 thin films with excellent electrical properties, i.e. a near bulk phase transition temperature (T_{SMT}) of around 68.4 ℃, a sharp transition (ΔT) of 4.3 ℃, a large resistance change (ΔA) of 3.2 $\times 10^3$ times, and 9.2 ℃ width of thermal hysteresis (ΔH), were achieved on amorphous glass substrates. Their properties were compared with the ones on *c*-cut sapphire and Si (111) substrates, all deposited by PLD. VO_2 thin film on glass substrate has its predominant texturing along (011) orientation with large columnar grains. On *c*-cut sapphire substrate, highly textured (002) orientation VO_2 film is grown with a high density of domain boundaries both in-plane and out-of-plane. The VO_2 film on Si (111) substrate has a (011) preferred orientation with layer by layer microstructure. The outstanding SMT properties of the VO_2 films on glass substrates are related to their large grain size and low defects density.

In order to investigate the grain boundary effects on VO_2 film SMT properties, polycrystalline VO_2 thin films with the average grain size of 350 nm, 100 nm, 70 nm and 40 nm were then deposited on amorphous glass substrates by PLD. The phase transition properties of each VO_2 film were correlated with the grain size. The film with larger average grain sizes (thus lower GB density) exhibits better phase transition properties, i.e. higher transition amplitude and sharper transition (ΔA as high as 3750 and ΔT as narrow as 3K for the sample with the grain size of 350 nm). HR-TEM image at the GB

area revealed that the GB is highly disordered and the VO_2 lattices next to the GB are strained due to the stress at GBs. Both highly disordered GBs and strained lattices contribute to the decrease of transition amplitude and broadening of transition sharpness for VO_2 with grain size smaller than 100 nm.

Third, two simple and effective approaches in tuning the T_c of VO_2 films were demonstrated using AZO buffers. One is to couple film thickness and the strain effect from AZO buffer. Epitaxial VO_2 thin films with thickness of 120 nm, 65 nm and 30 nm were deposited on AZO buffered *c*-cut sapphire substrates by PLD. The second approach is to tune the film strain by AZO buffer surface roughness. The oxygen pressures for AZO buffer layers growth were varied from 50 mtorr, 100 mtorr, 150 mtorr, to 200 mtorr to achieve different surface roughness. Through these two approaches, the T_c of VO_2 films was continuously tuned from 338.2 K (65.05 ℃) to 320.8 K (47.65 ℃). With the decrease of VO_2 thickness or VO_2/AZO interface roughness, tensile strain increases along the *c*-axis of VO_2 lattice, which leads to the decrease of T_c. No significant degradation of other SMT properties, i.e. ΔA, ΔT and ΔH, has been observed. The strain in the VO_2 thin films was mainly generated by the lattice mismatch between VO_2 and AZO. With the increase of VO_2/AZO interface roughness, the VO_2 film strain was gradually released by generating high density of dislocations around the interface area.

Finally, the stability of SMT properties of epitaxial VO_2 thin film on *c*-cut sapphire substrate was investigated. The SMT properties were characterized throughout 30 thermal cycles. The film maintains high transition amplitude (ΔA~6000) but exhibits the degradations of the transition width and thermal hysteresis with cycling numbers,

where ΔT increases from 6.3 ℃ to 12.3 ℃ and ΔH increases from 7.4 ℃ to 11.5 ℃ after 30 cycles. Moreover, the degradations of the ΔT and ΔH are more rapid within the first 15 cycles. *In situ* TEM heating studies revealed that the film contains high density of domain boundaries, around which large strain is accumulated during thermal cycles. The strain accumulation, which could be caused by the phase transition induced lattice constant change and the film thermal expansions, is correlated with the degradations of ΔT and ΔH. Despite of that, the boundaries actually provide an effective way to accommodate the strain generated during thermal cycles and thus protect the film from failure.

REFERENCES

1. Hanaor, D. A. H.; Sorrell, C. C., Review of the anatase to rutile phase transformation. *J Mater Sci* 2011, 46, 855-874.

2. Kuwahara, H.; Tomioka, Y.; Asamitsu, A.; Moritomo, Y.; Tokura, Y., A first-order phase-transition induced by a magnetic-field. *Science* 1995, 270, 961-963.

3. Urushibara, A.; Moritomo, Y.; Arima, T.; Asamitsu, A.; Kido, G.; Tokura, Y., Insulator-metal transition and giant magnetoresistance in la1-xsrxmno3. *Phys Rev B* 1995, 51, 14103-14109.

4. Partlow, D. P.; Gurkovich, S. R.; Radford, K. C.; Denes, L. J., Switchable vanadium-oxide films by a sol-gel process. *J Appl Phys* 1991, 70, 443-452.

5. Goodenough, J. B., 2 components of crystallographic transition in vo2. *J Solid State Chem* 1971, 3, 490-+.

6. Imada, M.; Fujimori, A.; Tokura, Y., Metal-insulator transitions. *Rev Mod Phys* 1998, 70, 1039-1263.

7. Eyert, V., The metal-insulator transitions of vo2: A band theoretical approach. *Ann Phys-Berlin* 2002, 11, 650-702.

8. Zylbersztejn, A.; Mott, N. F., Metal-insulator transition in vanadium dioxide. *Phys Rev B* 1975, 11, 4383-4395.

9. Stefanovich, G.; Pergament, A.; Stefanovich, D., Electrical switching and mott transition in vo2. *J Phys-Condens Mat* 2000, 12, 8837-8845.

10. Rogers, K. D.; Coath, J. A.; Lovell, M. C., Characterization of epitaxially grown films of vanadium-oxides. *J Appl Phys* 1991, 70, 1412-1415.

11. Benmoussa, M.; Ibnouelghazi, E.; Bennouna, A.; Ameziane, E. L., Structural, electrical and optical-properties of sputtered vanadium pentoxide thin-films. *Thin Solid Films* 1995, 265, 22-28.

12. Chain, E. E., Optical-properties of vanadium dioxide and vanadium pentoxide thin-films. *Appl Optics* 1991, 30, 2782-2787.

13. Choi, H. S.; Ahn, J. S.; Jung, J. H.; Noh, T. W.; Kim, D. H., Mid-infrared properties of a vo2 film near the metal-insulator transition. *Phys Rev B* 1996, 54, 4621-4628.

14. Strelcov, E.; Lilach, Y.; Kolmakov, A., Gas sensor based on metal-insulator

transition in vo2 nanowire thermistor. *Nano Lett* 2009, 9, 2322-2326.

15. Nori, S.; Yang, T. H.; Narayan, J., Vo2 thin films: Defect mediation in room temperature ferromagnetic switching characteristics. *Jom-Us* 2011, 63, 29-33.

16. Granqvist, C. G., Electrochromic materials - microstructure, electronic bands, and optical-properties. *Appl Phys a-Mater* 1993, 57, 3-12.

17. Rua, A.; Fernandez, F. E.; Sepulveda, N., Bending in vo2-coated microcantilevers suitable for thermally activated actuators. *J Appl Phys* 2010, 107.

18. Driscoll, T.; Kim, H. T.; Chae, B. G.; Di Ventra, M.; Basov, D. N., Phase-transition driven memristive system. *Appl Phys Lett* 2009, 95.

19. Ruzmetov, D.; Ramanathan, S., Metal-insulator transition in thin film vanadium dioxide. *Thin Film Metal-Oxides: Fundamentals and Applications in Electronics and Energy* 2010, 51-94.

20. Liu, M. K.; Hwang, H. Y.; Tao, H.; Strikwerda, A. C.; Fan, K. B.; Keiser, G. R.; Sternbach, A. J.; West, K. G.; Kittiwatanakul, S.; Lu, J. W.; Wolf, S. A.; Omenetto, F. G.; Zhang, X.; Nelson, K. A.; Averitt, R. D., Terahertz-field-induced insulator-to-metal transition in vanadium dioxide metamaterial. *Nature* 2012, 487, 345-348.

21. Wei, J.; Wang, Z. H.; Chen, W.; Cobden, D. H., New aspects of the metal-insulator transition in single-domain vanadium dioxide nanobeams. *Nat Nanotechnol* 2009, 4, 420-424.

22. Brassard, D.; Fourmaux, S.; Jean-Jacques, M.; Kieffer, J. C.; El Khakani, M. A., Grain size effect on the semiconductor-metal phase transition characteristics of magnetron-sputtered vo2 thin films. *Appl Phys Lett* 2005, 87.

23. Suh, J. Y.; Lopez, R.; Feldman, L. C.; Haglund, R. F., Semiconductor to metal phase transition in the nucleation and growth of vo2 nanoparticles and thin films. *J Appl Phys* 2004, 96, 1209-1213.

24. Fan, L. L.; Wu, Y. F.; Si, C.; Zou, C. W.; Qi, Z. M.; Li, L. B.; Pan, G. Q.; Wu, Z. Y., Oxygen pressure dependent vo2 crystal film preparation and the interfacial epitaxial growth study. *Thin Solid Films* 2012, 520, 6124-6129.

25. Greenberg, C. B., Undoped and doped vo2 films grown from vo(oc3h7)3. *Thin Solid Films* 1983, 110, 73-82.

26. Borek, M.; Qian, F.; Nagabushnam, V.; Singh, R. K., Pulsed-laser deposition of oriented vo2 thin-films on r-cut sapphire substrates. *Appl Phys Lett* 1993, 63, 3288-3290.

27. Case, F. C., Effects of low-energy low-flux ion-bombardment on the properties of

vo2 thin-films. *Journal of Vacuum Science & Technology a-Vacuum Surfaces and Films* 1989, 7, 1194-1198.

28. Yang, T. H.; Jin, C. M.; Aggarwal, R.; Narayan, R. J.; Narayan, J., On growth of epitaxial vanadium oxide thin film on sapphire (0001). *J Mater Res* 2010, 25, 422-426.

29. Can, M. M.; Shah, S. I.; Doty, M. F.; Haughn, C. R.; Firat, T., Electrical and optical properties of point defects in zno thin films. *J Phys D Appl Phys* 2012, 45.

30. Nishikawa, M.; Nakajima, T.; Manabe, T.; Okutani, T.; Tsuchiya, T., Preparation of polycrystalline vo2 films on glass and tio2/glass substrates by means of excimer laser assisted metal organic deposition. *J Ceram Soc Jpn* 2010, 118, 788-791.

31. Mlyuka, N. R.; Niklasson, G. A.; Granqvist, C. G., Mg doping of thermochromic vo2 films enhances the optical transmittance and decreases the metal-insulator transition temperature. *Appl Phys Lett* 2009, 95.

32. Macchesn.Jb; Guggenhe.Hj, Growth and electrical properties of vanadium dioxide single crystals containing selected impurity ions. *J Phys Chem Solids* 1969, 30, 225-&.

33. Soltani, M.; Chaker, M.; Haddad, E.; Kruzelesky, R., 1 x 2 optical switch devices based on semiconductor-to-metallic phase transition characteristics of vo2 smart coatings. *Meas Sci Technol* 2006, 17, 1052-1056.

34. Takahashi, I.; Hibino, M.; Kudo, T., Thermochromic properties of double-doped vo2 thin films prepared by a wet coating method using polyvanadate-based sols containing w and mo or w and ti. *Jpn J Appl Phys 1* 2001, 40, 1391-1395.

35. Chae, B. G.; Kim, H. T.; Yun, S. J., Characteristics of w- and ti-doped vo(2) thin films prepared by sol-gel method. *Electrochem Solid St* 2008, 11, D53-D55.

36. Beteille, F.; Livage, J., Optical switching in vo2 thin films. *J Sol-Gel Sci Techn* 1998, 13, 915-921.

37. Narayan, J.; Bhosle, V. M., Phase transition and critical issues in structure-property correlations of vanadium oxide. *J Appl Phys* 2006, 100.

38. Beteille, F.; Mazerolles, L.; Livage, J., Microstructure and metal-insulating transition of vo2 thin films. *Mater Res Bull* 1999, 34, 2177-2184.

39. He, X. F.; Xu, T.; Xu, X. F.; Zeng, Y. J.; Xu, J.; Sun, L. T.; Wang, C. R.; Xing, H. Z.; Wu, B. H.; Lu, A. J.; Liu, D. Q.; Chen, X. S.; Chu, J. H., In situ atom scale visualization of domain wall dynamics in vo2 insulator-metal phase transition. *Sci Rep-Uk* 2014, 4.

40. Guo, H.; Chen, K.; Oh, Y.; Wang, K.; Dejoie, C.; Asif, S. A. S.; Warren, O. L.; Shan, Z. W.; Wu, J.; Minor, A. M., Mechanics and dynamics of the strain-induced m1-m2

structural phase transition in individual vo2 nanowires. *Nano Lett* 2011, 11, 3207-3213.

41. Guo, H.; Wang, K. V.; Deng, Y.; Oh, Y.; Asif, S. A. S.; Warren, O. L.; Shan, Z. W.; Wu, J.; Minor, A. M., Nanomechanical actuation from phase transitions in individual vo2 micro-beams. *Appl Phys Lett* 2013, 102.

42. Surnev, S.; Ramsey, M. G.; Netzer, F. P., Vanadium oxide surface studies. *Prog Surf Sci* 2003, 73, 117-165.

43. Griffith.Ch; Eastwood, H. K., Influence of stoichiometry on metal-semiconductor transition in vanadium dioxide. *J Appl Phys* 1974, 45, 2201-2206.

44. Nag, J.; Haglund, R. F., Synthesis of vanadium dioxide thin films and nanoparticles. *J Phys-Condens Mat* 2008, 20.

45. Morin, F. J., Oxides which show a metal-to-insulator transition at the neel temperature. *Phys Rev Lett* 1959, 3, 34-36.

46. Blum, R. P.; Niehus, H.; Hucho, C.; Fortrie, R.; Ganduglia-Pirovano, M. V.; Sauer, J.; Shaikhutdinov, S.; Freund, H. J., Surface metal-insulator transition on a vanadium pentoxide (001) single crystal. *Phys Rev Lett* 2007, 99.

47. Kang, M.; Kim, I.; Kim, S. W.; Ryu, J. W.; Park, H. Y., Metal-insulator transition without structural phase transition in v2o5 film. *Appl Phys Lett* 2011, 98.

48. Kim, H. T.; Chae, B. G.; Youn, D. H.; Maeng, S. L.; Kim, G.; Kang, K. Y.; Lim, Y. S., Mechanism and observation of mott transition in vo2-based two- and three-terminal devices. *New J Phys* 2004, 6.

49. Piccirillo, C.; Binions, R.; Parkin, I. P., Synthesis and functional properties of vanadium oxides: V(2)o(3), vo(2), and v(2)o(5) deposited on glass by aerosol-assisted cvd. *Chem Vapor Depos* 2007, 13, 145-151.

50. Chudnovskii, F. A.; Pergament, A. L.; Schaefer, D. A.; Stefanovich, G. B., Optical medium on the basis of vanadium oxide films. *P Soc Photo-Opt Ins* 1996, 2777, 80-84.

51. Lee, S.; Ivanov, I. N.; Keum, J. K.; Lee, H. N., Epitaxial stabilization and phase instability of vo2 polymorphs. *Sci Rep-Uk* 2016, 6.

52. Mcwhan, D. B.; Marezio, M.; Remeika, J. P.; Dernier, P. D., X-ray-diffraction study of metallic vo2. *Phys Rev B* 1974, 10, 490-495.

53. Longo, J. M.; Kierkega.P, A refinement of structure of vo2. *Acta Chem Scand* 1970, 24, 420-&.

54. Wentzcovitch, R. M.; Schulz, W. W.; Allen, P. B., Vo2 - peierls or mott-hubbard - a

view from band theory. *Phys Rev Lett* 1994, 72, 3389-3392.

55. Wentzcovitch, R. M.; Schulz, W. W.; Allen, P. B., Comment on vo2 - peierls or mott-hubbard - a view from band theory - reply. *Phys Rev Lett* 1994, 73, 3043-3043.

56. Marezio, M.; Mcwhan, B.; Dernier, P. D.; Remeika, J. P., Structural aspects of metal-insulator transitions in cr-doped vo2. *Phys Rev B-Solid St* 1972, 5, 2541-&.

57. Shin, S.; Suga, S.; Taniguchi, M.; Fujisawa, M.; Kanzaki, H.; Fujimori, A.; Daimon, H.; Ueda, Y.; Kosuge, K.; Kachi, S., Vacuum-ultraviolet reflectance and photoemission-study of the metal-insulator phase-transitions in vo2, v6o13, and v2o3. *Phys Rev B* 1990, 41, 4993-5009.

58. Bongers, P. F., Anisotropy of the electrical conductivity of vo(2) single crystals. *Solid State Commun* 1965, 3, 275-277.

59. Kosuge, K., Phase transition in vo2. *J Phys Soc Jpn* 1967, 22, 551-&.

60. Sawatzky, G. A.; Post, D., X-ray photoelectron and auger-spectroscopy study of some vanadium-oxides. *Phys Rev B* 1979, 20, 1546-1555.

61. Goodenou.Jb, Narrow-band electrons in transition-metal oxides. *Czech J Phys* 1967, 17, 304-&.

62. Cavalleri, A.; Dekorsy, T.; Chong, H. H. W.; Kieffer, J. C.; Schoenlein, R. W., Evidence for a structurally-driven insulator-to-metal transition in vo2: A view from the ultrafast timescale. *Phys Rev B* 2004, 70.

63. Fisher, B., Metal-semiconductor domain configurations during switching of vo-2 single-crystals. *J Phys C Solid State* 1976, 9, 1201-1209.

64. Peierls, R. E., *More surprises in theoretical physics*. Princeton University Press: Princeton, N.J., 1991; p vi, 106 p.

65. Hansen, L. K.; Carneiro, K., On the peierls transition in a periodic potential. *Solid State Commun* 1984, 49, 531-535.

66. Mott, N. F.; Friedman, L., Metal-insulator transitions in vo2, ti2o3 and ti2-xvxo3. *Philos Mag* 1974, 30, 389-402.

67. Jordens, R.; Strohmaier, N.; Gunther, K.; Moritz, H.; Esslinger, T., A mott insulator of fermionic atoms in an optical lattice. *Nature* 2008, 455, 204-U34.

68. De Boer, J. H.; Verwey, E. J. W., Semi-conductors with partially and with completely filled 3d-lattice bands. *P Phys Soc* 1937, 49, A59-A71.

69. Mott, N. F.; Peierls, R., Discussion of the paper by de boer and verwey. *P Phys Soc* 1937, 49, A72-A73.

70. Mott, N. F., The basis of the electron theory of metals, with special reference to the transition metals. *P Phys Soc Lond A* 1949, 62, 416-422.

71. Hubbard, J., Electron correlations in narrow energy bands. *Proc R Soc Lon Ser-A* 1963, 276, 238-+.

72. Kuiper, P.; Kruizinga, G.; Ghijsen, J.; Sawatzky, G. A.; Verweij, H., Character of holes in lixni1-xo and their magnetic-behavior. *Phys Rev Lett* 1989, 62, 221-224.

73. Cyrot, M., Theory of mott transition - applications to transition-metal oxides. *J Phys-Paris* 1972, 33, 125-&.

74. Zimmermann, R.; Steiner, P.; Claessen, R.; Reinert, F.; Hufner, S.; Blaha, P.; Dufek, P., Electronic structure of 3d-transition-metal oxides: On-site coulomb repulsion versus covalency. *J Phys-Condens Mat* 1999, 11, 1657-1682.

75. Berglund, C. N.; Guggenhe.Hj, Electronic properties of vo2 near semiconductor-metal transition. *Phys Rev* 1969, 185, 1022-&.

76. Qazilbash, M. M.; Burch, K. S.; Whisler, D.; Shrekenhamer, D.; Chae, B. G.; Kim, H. T.; Basov, D. N., Correlated metallic state of vanadium dioxide. *Phys Rev B* 2006, 74.

77. Cao, J.; Gu, Y.; Fan, W.; Chen, L. Q.; Ogletree, D. F.; Chen, K.; Tamura, N.; Kunz, M.; Barrett, C.; Seidel, J.; Wu, J., Extended mapping and exploration of the vanadium dioxide stress-temperature phase diagram. *Nano Lett* 2010, 10, 2667-2673.

78. Kim, H. T.; Chae, B. G.; Youn, D. H.; Kim, G.; Kang, K. Y.; Lee, S. J.; Kim, K.; Lim, Y. S., Raman study of electric-field-induced first-order metal-insulator transition in vo2-based devices. *Appl Phys Lett* 2005, 86.

79. West, K. G.; Lu, J. W.; Yu, J.; Kirkwood, D.; Chen, W.; Pei, Y. H.; Claassen, J.; Wolf, S. A., Growth and characterization of vanadium dioxide thin films prepared by reactive-biased target ion beam deposition. *J Vac Sci Technol A* 2008, 26, 133-139.

80. Rini, M.; Hao, Z.; Schoenlein, R. W.; Giannetti, C.; Parmigiani, F.; Fourmaux, S.; Kieffer, J. C.; Fujimori, A.; Onoda, M.; Wall, S.; Cavalleri, A., Optical switching in vo(2) films by below-gap excitation. *Appl Phys Lett* 2008, 92.

81. Whittaker, L.; Zhang, H. S.; Banerjee, S., Vo2 nanosheets exhibiting a well-defined metal-insulator phase transition. *J Mater Chem* 2009, 19, 2968-2974.

82. Takala, J.; Keinanen, O.; Vaisanen, P.; Kari, A., Measurement of gas-exchange in intensive-care - laboratory and clinical validation of a new device. *Crit Care Med* 1989,

17, 1041-1047.

83. Chen, S.; Yi, X.; Ma, H.; Wang, H.; Tao, X.; Chen, M.; Ke, C., A novel structural vo2 micro-optical switch. *Opt Quant Electron* 2003, 35, 1351-1355.

84. Huang, Z. L.; Chen, S. H.; Lv, C. H.; Huang, Y.; Lai, J. J., Infrared characteristics of vo2 thin films for smart window and laser protection applications. *Appl Phys Lett* 2012, 101.

85. Neto, G.; de Almeida, L. A. L.; Lima, A. M. N.; Moreira, C. S.; Neff, H., Figures of merit and optimization of a vo(2) microbolometer with strong electrothermal feedback. *Opt Eng* 2008, 47.

86. Ryabova, L. A.; Serbinov, I. A.; Darevsky, A. S., Preparation and properties of pyrolysis of vanadium oxide-films. *J Electrochem Soc* 1972, 119, 427-&.

87. Kim, D. H.; Kwok, H. S., Pulsed-laser deposition of vo2 thin-films. *Appl Phys Lett* 1994, 65, 3188-3190.

88. Chain, E. E., The influence of deposition temperature on the structure and optical-properties of vanadium-oxide films. *Journal of Vacuum Science & Technology a-Vacuum Surfaces and Films* 1986, 4, 432-435.

89. Kusano, E.; Theil, J. A., Effects of microstructure and nonstoichiometry on electrical-properties of vanadium dioxide films. *Journal of Vacuum Science & Technology a-Vacuum Surfaces and Films* 1989, 7, 1314-1317.

90. Jerominek, H.; Picard, F.; Vincent, D., Vanadium-oxide films for optical switching and detection. *Opt Eng* 1993, 32, 2092-2099.

91. Case, F. C., Modifications in the phase-transition properties of predeposited vo-2 films. *Journal of Vacuum Science & Technology a-Vacuum Surfaces and Films* 1984, 2, 1509-1512.

92. Denatale, J. F.; Hood, P. J.; Harker, A. B., Formation and characterization of grain-oriented vo2 thin-films. *J Appl Phys* 1989, 66, 5844-5850.

93. Kim, H. K.; You, H.; Chiarello, R. P.; Chang, H. L. M.; Zhang, T. J.; Lam, D. J., Finite-size effect on the 1st-order metal-insulator-transition in vo2 films grown by metal-organic chemical-vapor-deposition. *Phys Rev B* 1993, 47, 12900-12907.

94. Sahana, M. B.; Subbanna, G. N.; Shivashankar, S. A., Phase transformation and semiconductor-metal transition in thin films of vo2 deposited by low-pressure metalorganic chemical vapor deposition. *J Appl Phys* 2002, 92, 6495-6504.

95. Chae, B. G.; Kim, H. T.; Yun, S. J.; Kim, B. J.; Lee, Y. W.; Youn, D. H.; Kang, K. Y.,

Highly oriented vo2 thin films prepared by sol-gel deposition. *Electrochem Solid St* 2006, 9, C12-C14.

96. Fuls, E. N.; Hensler, D. H.; Ross, A. R., Reactively sputtered vanadium dioxide thin films. *Appl Phys Lett* 1967, 10, 199-&.

97. Okimura, K.; Kubo, N., Growth of vo2 films with metal-insulator transition on silicon substrates in inductively coupled plasma-assisted sputtering. *Thin Solid Films* 2007, 515, 4992-4995.

98. Hirvonen, J. K., Ion-beam assisted thin-film deposition. *Mater Sci Rep* 1991, 6, 215-274.

99. Okimura, K.; Kubo, N., Preparation of vo2 films with metal-insulator transition on sapphire and silicon substrates by inductively coupled plasma-assisted sputtering. *Jpn J Appl Phys 2* 2005, 44, L1150-L1153.

100. Wang, H. C.; Yi, X. J.; Lai, J. J.; Li, Y., Fabrication and characterization of nanocrystalline vo2 thin films. *Chinese Phys Lett* 2005, 22, 1746-1748.

101. Jian, J.; Chen, A. P.; Zhang, W. R.; Wang, H. Y., Sharp semiconductor-to-metal transition of vo2 thin films on glass substrates. *J Appl Phys* 2013, 114.

102. Wu, X. C.; Tao, Y. R.; Lin, D.; Wang, Z. H.; Zheng, H., Preparation of vo2 nanowires and their electric characterization. *Mater Res Bull* 2005, 40, 315-321.

103. Guiton, B. S.; Gu, Q.; Prieto, A. L.; Gudiksen, M. S.; Park, H., Single-crystalline vanadium dioxide nanowires with rectangular cross sections. *J Am Chem Soc* 2005, 127, 498-499.

104. Sohn, J. I.; Joo, H. J.; Ahn, D.; Lee, H. H.; Porter, A. E.; Kim, K.; Kang, D. J.; Welland, M. E., Surface-stress-induced mott transition and nature of associated spatial phase transition in single crystalline vo2 nanowires. *Nano Lett* 2009, 9, 3392-3397.

105. Wu, J. Q.; Gu, Q.; Guiton, B. S.; de Leon, N. P.; Lian, O. Y.; Park, H., Strain-induced self organization of metal-insulator domains in single-crystalline vo2 nanobeams. *Nano Lett* 2006, 6, 2313-2317.

106. Cao, J.; Ertekin, E.; Srinivasan, V.; Fan, W.; Huang, S.; Zheng, H.; Yim, J. W. L.; Khanal, D. R.; Ogletree, D. F.; Grossmanan, J. C.; Wu, J., Strain engineering and one-dimensional organization of metal-insulator domains in single-crystal vanadium dioxide beams. *Nat Nanotechnol* 2009, 4, 732-737.

107. Bruckner, W.; Moldenhauer, W.; Wich, H.; Wolf, E.; Oppermann, H.; Gerlach, U.; Reichelt, W., Range of homogeneity of vo2 and influence of composition on

physical-properties .2. Change of physical-properties in range of homogeneity. *Phys Status Solidi A* 1975, 29, 63-70.

108. Joannopoulos, J. D.; Villeneuve, P. R.; Fan, S. H., Photonic crystals: Putting a new twist on light (vol 386, pg 143, 1997). *Nature* 1997, 387, 830-830.

109. Haes, A. J.; Van Duyne, R. P., A nanoscale optical blosensor: Sensitivity and selectivity of an approach based on the localized surface plasmon resonance spectroscopy of triangular silver nanoparticles. *J Am Chem Soc* 2002, 124, 10596-10604.

110. Maier, S. A.; Kik, P. G.; Atwater, H. A.; Meltzer, S.; Harel, E.; Koel, B. E.; Requicha, A. A. G., Local detection of electromagnetic energy transport below the diffraction limit in metal nanoparticle plasmon waveguides. *Nat Mater* 2003, 2, 229-232.

111. Lopez, R.; Feldman, L. C.; Haglund, R. F., Size-dependent optical properties of vo2 nanoparticle arrays. *Phys Rev Lett* 2004, 93.

112. Lopez, R.; Haynes, T. E.; Boatner, L. A.; Feldman, L. C.; Haglund, R. F., Size effects in the structural phase transition of vo2 nanoparticles. *Phys Rev B* 2002, 65.

113. Donev, E. U.; Ziegler, J. I.; Haglund, R. F.; Feldman, L. C., Size effects in the structural phase transition of vo2 nanoparticles studied by surface-enhanced raman scattering. *J Opt a-Pure Appl Op* 2009, 11.

114. Li, S. Y.; Niklasson, G. A.; Granqvist, C. G., Nanothermochromics: Calculations for vo2 nanoparticles in dielectric hosts show much improved luminous transmittance and solar energy transmittance modulation. *J Appl Phys* 2010, 108.

115. Appavoo, K.; Lei, D. Y.; Sonnefraud, Y.; Wang, B.; Pantelides, S. T.; Maier, S. A.; Haglund, R. F., Role of defects in the phase transition of vo2 nanoparticles probed by plasmon resonance spectroscopy. *Nano Lett* 2012, 12, 780-786.

116. Seiyama, T.; Kato, A.; Fujiishi, K.; Nagatani, M., A new detector for gaseous components using semiconductive thin films. *Anal Chem* 1962, 34, 1502-1503.

117. Choi, K. J.; Jang, H. W., One-dimensional oxide nanostructures as gas-sensing materials: Review and issues. *Sensors-Basel* 2010, 10, 4083-4099.

118. Patolsky, F.; Zheng, G. F.; Lieber, C. M., Nanowire-based biosensors. *Anal Chem* 2006, 78, 4260-4269.

119. Comini, E.; Baratto, C.; Faglia, G.; Ferroni, M.; Vomiero, A.; Sberveglieri, G., Quasi-one dimensional metal oxide semiconductors: Preparation, characterization and application as chemical sensors. *Prog Mater Sci* 2009, 54, 1-67.

120. Chen, P. C.; Shen, G. Z.; Zhou, C. W., Chemical sensors and electronic noses

based on 1-d metal oxide nanostructures. *Ieee T Nanotechnol* 2008, 7, 668-682.

121. Kolmakov, A., Some recent trends in the fabrication, functionalisation and characterisation of metal oxide nanowire gas sensors. *Int J Nanotechnol* 2008, 5, 450-474.

122. Pearton, S. J.; Kang, B. S.; Gila, B. P.; Norton, D. P.; Kryliouk, O.; Ren, F.; He, Y. W.; Chang, C. Y.; Chi, G. C.; Wang, W. M.; Chen, L. C., Gan, zno and inn nanowires and devices. *J Nanosci Nanotechno* 2008, 8, 99-110.

123. Law, M.; Sirbuly, D. J.; Yang, P. D., Chemical sensing with nanowires using electrical and optical detection. *Int J Nanotechnol* 2007, 4, 252-262.

124. Baik, J. M.; Kim, M. H.; Larson, C.; Yavuz, C. T.; Stucky, G. D.; Wodtke, A. M.; Moskovits, M., Pd-sensitized single vanadium oxide nanowires: Highly responsive hydrogen sensing based on the metal-insulator transition. *Nano Lett* 2009, 9, 3980-3984.

125. Ovshinsk.Sr, Reversible electrical switching phenomena in disordered structures. *Phys Rev Lett* 1968, 21, 1450-&.

126. Duchene, J. C.; Terraill.Mm; Pailly, M.; Adam, G. B., Initiation of switching in vo2 coplanar devices. *Ieee T Electron Dev* 1971, Ed18, 1151-&.

127. Mansingh, A.; Singh, R., The mechanism of electrical threshold switching in vo2 crystals. *J Phys C Solid State* 1980, 13, 5725-5733.

128. Higgins, J. K.; Temple, B. K.; Lewis, J. E., Electrical-properties of vanadate-glass threshold switches. *J Non-Cryst Solids* 1977, 23, 187-215.

129. Lee, J. S.; Ortolani, M.; Schade, U.; Chang, Y. J.; Noh, T. W., Time-resolved visualization of the heat flow in vo2/al2o3 films. *Appl Phys Lett* 2007, 90.

130. Okimura, K.; Sakai, J., Time-dependent characteristics of electric field-induced metal-insulator transition of planer vo2/c-al2o3 structure. *Jpn J Appl Phys 2* 2007, 46, L813-L816.

131. Okimura, K.; Ezreena, N.; Sasakawa, Y.; Sakai, J., Electric-field-induced multistep resistance switching in planar vo2/c-al2o3 structure. *Jpn J Appl Phys* 2009, 48.

132. Ha, S. D.; Zhou, Y.; Fisher, C. J.; Ramanathan, S.; Treadway, J. P., Electrical switching dynamics and broadband microwave characteristics of vo2 radio frequency devices. *J Appl Phys* 2013, 113.

133. Crunteanu, A.; Givernaud, J.; Leroy, J.; Mardivirin, D.; Champeaux, C.; Orlianges, J. C.; Catherinot, A.; Blondy, P., Voltage- and current-activated metal-insulator transition in vo2-based electrical switches: A lifetime operation analysis.

Sci Technol Adv Mat 2010, 11.

134. Gong, X. Q.; Li, J. X.; Chen, S. Y.; Wen, W. J., Copolymer solution-based "smart window". *Appl Phys Lett* 2009, 95.

135. Bonora, S.; Bortolozzo, U.; Residori, S.; Balu, R.; Ashrit, P. V., Mid-ir to near-ir image conversion by thermally induced optical switching in vanadium dioxide. *Opt Lett* 2010, 35, 103-105.

136. Kato, K.; Song, P. K.; Odaka, H.; Shigesato, Y., Study on thermochromic vo2 films grown on zno-coated glass substrates for "smart windows". *Japanese Journal of Applied Physics Part 1-Regular Papers Brief Communications & Review Papers* 2003, 42, 6523-6531.

137. Granqvist, C. G., Transparent conductors as solar energy materials: A panoramic review. *Sol Energ Mat Sol C* 2007, 91, 1529-1598.

138. Babulanam, S. M.; Eriksson, T. S.; Niklasson, G. A.; Granqvist, C. G., Thermochromic vo2 films for energy-efficient windows. *Sol Energ Mater* 1987, 16, 347-363.

139. Jin, P.; Xu, G.; Tazawa, M.; Yoshimura, K., Design, formation and characterization of a novel multifunctional window with vo2 and tio2 coatings. *Appl Phys a-Mater* 2003, 77, 455-459.

140. Heinilehto, S. T.; Lappalainen, J. H.; Jantunen, H. M.; Lantto, V., Ir-wavelength optical shutter based on ito/vo2/ito thin film stack. *J Electroceram* 2011, 27, 7-12.

141. Burkhardt, W.; Christmann, T.; Meyer, B. K.; Niessner, W.; Schalch, D.; Scharmann, A., W- and f-doped vo2 films studied by photoelectron spectrometry. *Thin Solid Films* 1999, 345, 229-235.

142. Hu, S. L.; Li, S. Y.; Ahuja, R.; Granqvist, C. G.; Hermansson, K.; Niklasson, G. A.; Scheicher, R. H., Optical properties of mg-doped vo2: Absorption measurements and hybrid functional calculations. *Appl Phys Lett* 2012, 101.

143. Zhou, J. D.; Gao, Y. F.; Zhang, Z. T.; Luo, H. J.; Cao, C. X.; Chen, Z.; Dai, L.; Liu, X. L., Vo2 thermochromic smart window for energy savings and generation. *Sci Rep-Uk* 2013, 3.

144. Riethmuller, W.; Benecke, W., Thermally excited silicon microactuators. *Ieee T Electron Dev* 1988, 35, 758-763.

145. LeMieux, M. C.; McConney, M. E.; Lin, Y. H.; Singamaneni, S.; Jiang, H.; Bunning, T. J.; Tsukruk, V. V., Polymeric nanolayers as actuators for ultrasensitive

thermal bimorphs. *Nano Lett* 2006, 6, 730-734.

146. Cabrera, R.; Merced, E.; Sepulveda, N., Performance of electro-thermally driven vo2-based mems actuators. *J Microelectromech S* 2014, 23, 243-251.

147. Lee, S.; Cheng, C.; Guo, H.; Hippalgaonkar, K.; Wang, K.; Suh, J.; Liu, K.; Wu, J. Q., Axially engineered metal-insulator phase transition by graded doping vo2 nanowires. *J Am Chem Soc* 2013, 135, 4850-4855.

148. Cao, J. B.; Fan, W.; Zhou, Q.; Sheu, E.; Liu, A. W.; Barrett, C.; Wu, J., Colossal thermal-mechanical actuation via phase transition in single-crystal vo2 microcantilevers. *J Appl Phys* 2010, 108.

149. Di Ventra, M.; Pershin, Y. V.; Chua, L. O., Circuit elements with memory: Memristors, memcapacitors, and meminductors. *P Ieee* 2009, 97, 1717-1724.

150. Chua, L. O., Memristor - missing circuit element. *Ieee T Circuits Syst* 1971, Ct18, 507-&.

151. Chua, L. O.; Kang, S. M., Memristive devices and systems. *P Ieee* 1976, 64, 209-223.

152. Driscoll, T.; Quinn, J.; Klein, S.; Kim, H. T.; Kim, B. J.; Pershin, Y. V.; Di Ventra, M.; Basov, D. N., Memristive adaptive filters. *Appl Phys Lett* 2010, 97.

153. Bae, S. H.; Lee, S.; Koo, H.; Lin, L.; Jo, B. H.; Park, C.; Wang, Z. L., The memristive properties of a single vo2 nanowire with switching controlled by self-heating. *Adv Mater* 2013, 25, 5098-5103.

154. Yang, J. J.; Pickett, M. D.; Li, X. M.; Ohlberg, D. A. A.; Stewart, D. R.; Williams, R. S., Memristive switching mechanism for metal/oxide/metal nanodevices. *Nat Nanotechnol* 2008, 3, 429-433.

155. Sharoni, A.; Ramirez, J. G.; Schuller, I. K., Multiple avalanches across the metal-insulator transition of vanadium oxide nanoscaled junctions. *Phys Rev Lett* 2008, 101.

156. Dearnaley, G.; Stoneham, A. M.; Morgan, D. V., Electrical phenomena in amorphous oxide films. *Rep Prog Phys* 1970, 33, 1129-+.

157. Asamitsu, A.; Tomioka, Y.; Kuwahara, H.; Tokura, Y., Current switching of resistive states in magnetoresistive manganites. *Nature* 1997, 388, 50-52.

158. Custer, J. S.; Polman, A.; Vanpinxteren, H. M., Erbium in crystal silicon - segregation and trapping during solid-phase epitaxy of amorphous-silicon. *J Appl Phys* 1994, 75, 2809-2817.

159. Thompson, C. V., The materials science of thin-films - ohring,m. *Nature* 1992, 357, 292-292.

160. Masselink, W. T.; Pearah, P. J.; Klem, J.; Peng, C. K.; Morkoc, H.; Sanders, G. D.; Chang, Y. C., Absorption-coefficients and exciton oscillator-strengths in algaas-gaas superlattices. *Phys Rev B* 1985, 32, 8027-8034.

161. Homma, H.; Yang, K. Y.; Schuller, I. K., Role of lattice matching in epitaxy - novel ce phase and new fcc-bcc epitaxial relationship. *Phys Rev B* 1987, 36, 9435-9438.

162. Narayan, J.; Larson, B. C., Domain epitaxy: A unified paradigm for thin film growth. *J Appl Phys* 2003, 93, 278-285.

163. Myers, M. A.; Lee, J. H.; Bi, Z. X.; Wang, H. Y., High quality p-type ag-doped zno thin films achieved under elevated growth temperatures (vol 24, 145802, 2012). *J Phys-Condens Mat* 2012, 24.

164. Narayan, J.; Tiwari, P.; Chen, X.; Singh, J.; Chowdhury, R.; Zheleva, T., Epitaxial-growth of tin films on (100) silicon substrates by laser physical vapor-deposition. *Appl Phys Lett* 1992, 61, 1290-1292.

165. Berglund, C. N.; Jayaraman, A., Hydrostatic-pressure dependence of electronic properties of vo2 near semiconductor-metal transition temperature. *Phys Rev* 1969, 185, 1034-+.

166. Cavalleri, A.; Chong, H. H. W.; Fourmaux, S.; Glover, T. E.; Heimann, P. A.; Kieffer, J. C.; Mun, B. S.; Padmore, H. A.; Schoenlein, R. W., Picosecond soft x-ray absorption measurement of the photoinduced insulator-to-metal transition in vo2. *Phys Rev B* 2004, 69.

167. Zhou, H.; Chisholm, M. F.; Yang, T. H.; Pennycook, S. J.; Narayan, J., Role of interfacial transition layers in vo2/al2o3 heterostructures. *J Appl Phys* 2011, 110.

168. Jin, P.; Yoshimura, K.; Tanemura, S., Dependence of microstructure and thermochromism on substrate temperature for sputter-deposited vo2 epitaxial films. *Journal of Vacuum Science & Technology a-Vacuum Surfaces and Films* 1997, 15, 1113-1117.

169. Youn, D. H.; Kim, H. T.; Chae, B. G.; Hwang, Y. J.; Lee, J. W.; Maeng, S. L.; Kang, K. Y., Phase and structural characterization of vanadium oxide films grown on amorphous sio2/si substrates. *J Vac Sci Technol A* 2004, 22, 719-724.

170. Muraoka, Y.; Hiroi, Z., Metal-insulator transition of vo2 thin films grown on tio2 (001) and (110) substrates. *Appl Phys Lett* 2002, 80, 583-585.

171. Yang, T. H.; Jin, C. M.; Zhou, H. H.; Narayan, R. J.; Narayan, J., Role of twin boundaries in semiconductor to metal transition characteristics of vo2 films. *Appl Phys Lett* 2010, 97.

172. Minami, T.; Sato, H.; Imamoto, H.; Takata, S., Substrate-temperature dependence of transparent conducting al-doped zno thin-films prepared by magnetron sputtering. *Japanese Journal of Applied Physics Part 2-Letters* 1992, 31, L257-L260.

173. Wu, H. Z.; He, K. M.; Qiu, D. J.; Huang, D. M., Low-temperature epitaxy of zno films on si(001) and silica by reactive e-beam evaporation. *J Cryst Growth* 2000, 217, 131-137.

174. Koo, H.; Shin, D.; Bae, S. H.; Ko, K. E.; Chang, S. H.; Park, C., The effect of ceo2 antireflection layer on the optical properties of thermochromic vo2 film for smart window system. *J Mater Eng Perform* 2014, 23, 402-407.

175. Montero, J.; Ji, Y. X.; Li, S. Y.; Niklasson, G. A.; Granqvist, C. G., Sputter deposition of thermochromic vo2 films on in2o3: Sn, sno2, and glass: Structure and composition versus oxygen partial pressure. *J Vac Sci Technol B* 2015, 33.

176. Yang, T. H.; Aggarwal, R.; Gupta, A.; Zhou, H. H.; Narayan, R. J.; Narayan, J., Semiconductor-metal transition characteristics of vo2 thin films grown on c- and r-sapphire substrates. *J Appl Phys* 2010, 107.

177. Koo, H.; Yoon, S.; Kwon, O. J.; Ko, K. E.; Shin, D.; Bae, S. H.; Chang, S. H.; Park, C., Effect of lattice misfit on the transition temperature of vo2 thin film. *J Mater Sci* 2012, 47, 6397-6401.

178. Chiu, T. W.; Tonooka, K.; Kikuchi, N., Growth of b-axis oriented vo2 thin films on glass substrates using zno buffer layer. *Appl Surf Sci* 2010, 256, 6834-6837.

179. Jin, P.; Tanemura, S., Formation and thermochromism of vo(2) films deposited by rf magnetron sputtering at low substrate-temperature. *Japanese Journal Of Applied Physics Part 1-Regular Papers Brief Communications & Review Papers* 1994, 33, 1478-1483.

180. Wei, P. S. P.; Smith, A. W., Structure of (0001) surface of alpha-alumina. *J Vac Sci Technol* 1972, 9, 1209-&.

181. Kronberg, M. L., Plastic deformation of single crystals of sapphire - basal slip and twinning. *Acta Metall Mater* 1957, 5, 507-524.

182. French, R. H., Electronic band-structure of al2o3, with comparison to aion and ain. *J Am Ceram Soc* 1990, 73, 477-489.

183. Lucht, M.; Lerche, M.; Wille, H. C.; Shvyd'ko, Y. V.; Ruter, H. D.; Gerdau, E.; Becker, P., Precise measurement of the lattice parameters of alpha-al2o3 in the temperature range 4.5-250 k using the mossbauer wavelength standard. *J Appl Crystallogr* 2003, 36, 1075-1081.

184. Zhao, Y.; Lee, J. H.; Zhu, Y. H.; Nazari, M.; Chen, C. H.; Wang, H. Y.; Bernussi, A.; Holtz, M.; Fan, Z. Y., Structural, electrical, and terahertz transmission properties of vo2 thin films grown on c-, r-, and m-plane sapphire substrates. *J Appl Phys* 2012, 111.

185. Samela, J.; Nordlund, K.; Popok, V. N.; Campbell, E. E. B., Origin of complex impact craters on native oxide coated silicon surfaces. *Phys Rev B* 2008, 77.

186. Shi, Q. W.; Huang, W. X.; Yan, J. Z.; Zhang, Y. B.; Mao, M.; Zhang, Y.; Xu, Y. J.; Zhang, Y. X., Preparation and phase transition characterization of vo2 thin film on single crystal si (100) substrate by sol-gel process. *J Sol-Gel Sci Techn* 2011, 59, 591-597.

187. Dumas-Bouchiat, F.; Champeaux, C.; Catherinot, A.; Crunteanu, A.; Blondy, P., Rf-microwave switches based on reversible semiconductor-metal transition of vo(2) thin films synthesized by pulsed-laser deposition. *Appl Phys Lett* 2007, 91.

188. Chae, B. G.; Kim, H. T.; Yun, S. J.; Kim, B. J.; Lee, Y. W.; Kang, K. Y., Comparative analysis of vo2 thin films prepared on sapphire and sio2/si substrates by the sol-gel process. *Japanese Journal of Applied Physics Part 1-Regular Papers Brief Communications & Review Papers* 2007, 46, 738-743.

189. Yun, S. J.; Lim, J. W.; Noh, J. S.; Chae, B. G.; Kim, H. T., Vanadium dioxide films deposited on amorphous sio2- and al2o3-coated si substrates by reactive rf-magnetron sputter deposition. *Jpn J Appl Phys* 2008, 47, 3067-3069.

190. Gupta, A.; Aggarwal, R.; Gupta, P.; Dutta, T.; Narayan, R. J.; Narayan, J., Semiconductor to metal transition characteristics of vo2 thin films grown epitaxially on si (001). *Appl Phys Lett* 2009, 95.

191. Hanlon, T. J.; Walker, R. E.; Coath, J. A.; Richardson, M. A., Comparison between vanadium dioxide coatings on glass produced by sputtering, alkoxide and aqueous sol-gel methods. *Thin Solid Films* 2002, 405, 234-237.

192. Chiu, T. W.; Tonooka, K.; Kikuchi, N., Influence of oxygen pressure on the structural, electrical and optical properties of vo2 thin films deposited on zno/glass substrates by pulsed laser deposition. *Thin Solid Films* 2010, 518, 7441-7444.

193. Fierro, J. L. G., *Metal oxides : Chemistry and applications*. Taylor & Francis: Boca Raton, FL, 2006; p xxi, 783 p.

194. Pearton, S. J.; Norton, D. P.; Ip, K.; Heo, Y. W.; Steiner, T., Recent progress in processing and properties of zno. *Prog Mater Sci* 2005, 50, 293-340.

195. Ohtomo, A.; Kawasaki, M.; Koida, T.; Masubuchi, K.; Koinuma, H.; Sakurai, Y.; Yoshida, Y.; Yasuda, T.; Segawa, Y., Mgxzn1-xo as a ii-vi widegap semiconductor alloy. *Appl Phys Lett* 1998, 72, 2466-2468.

196. Makino, T.; Segawa, Y.; Kawasaki, M.; Ohtomo, A.; Shiroki, R.; Tamura, K.; Yasuda, T.; Koinuma, H., Band gap engineering based on mgxzn1-xo and cdyzn1-yo ternary alloy films. *Appl Phys Lett* 2001, 78, 1237-1239.

197. Ozgur, U.; Alivov, Y. I.; Liu, C.; Teke, A.; Reshchikov, M. A.; Dogan, S.; Avrutin, V.; Cho, S. J.; Morkoc, H., A comprehensive review of zno materials and devices. *J Appl Phys* 2005, 98.

198. Srivastava, A.; Herng, T. S.; Saha, S.; Nina, B.; Annadi, A.; Naomi, N.; Liu, Z. Q.; Dhar, S.; Ariando; Ding, J.; Venkatesan, T., Coherently coupled zno and vo2 interface studied by photoluminescence and electrical transport across a phase transition. *Appl Phys Lett* 2012, 100.

199. Koo, H.; Xu, L.; Ko, K. E.; Ahn, S.; Chang, S. H.; Park, C., Effect of oxide buffer layer on the thermochromic properties of vo2 thin films. *J Mater Eng Perform* 2013, 22, 3967-3973.

200. Molaei, R.; Bayati, R.; Wu, F.; Narayan, J., A microstructural approach toward the effect of thickness on semiconductor-to-metal transition characteristics of vo2 epilayers. *J Appl Phys* 2014, 115.

201. Kawatani, K.; Kanki, T.; Tanaka, H., Formation mechanism of a microscale domain and effect on transport properties in strained vo2 thin films on tio2(001). *Phys Rev B* 2014, 90.

202. Sohn, A.; Kanki, T.; Tanaka, H.; Kim, D. W., Visualization of local phase transition behaviors near dislocations in epitaxial vo2/tio2 thin films. *Appl Phys Lett* 2015, 107.

203. Aliev, R. A.; Andreev, V. N.; Kapralova, V. M.; Klimov, V. A.; Sobolev, A. I.; Shadrin, E. B., Effect of grain sizes on the metal-semiconductor phase transition in vanadium dioxide polycrystalline thin films. *Phys Solid State+* 2006, 48, 929-934.

204. Gurvitch, M.; Luryi, S.; Polyakov, A.; Shabalov, A.; Dudley, M.; Wang, G.; Ge, S.; Yakovlev, V., Vo2 films with strong semiconductor to metal phase transition prepared by the precursor oxidation process. *J Appl Phys* 2007, 102.

205. Barreca, D.; Depero, L. E.; Franzato, E.; Rizzi, G. A.; Sangaletti, L.; Tondello,

E.; Vettori, U., Vanadyl precursors used to modify the properties of vanadium oxide thin films obtained by chemical vapor deposition. *J Electrochem Soc* 1999, 146, 551-558.

206. Cao, J.; Fan, W.; Zheng, H.; Wu, J., Thermoelectric effect across the metal-insulator domain walls in vo2 microbeams. *Nano Lett* 2009, 9, 4001-4006.

207. Jian, J.; Zhang, W. R.; Jacob, C.; Chen, A. P.; Wang, H.; Huang, J. J.; Wang, H. Y., Roles of grain boundaries on the semiconductor to metal phase transition of vo2 thin films. *Appl Phys Lett* 2015, 107.

208. Wu, Z. P.; Miyashita, A.; Yamamoto, S.; Abe, H.; Nashiyama, I.; Narumi, K.; Naramoto, H., Molybdenum substitutional doping and its effects on phase transition properties in single crystalline vanadium dioxide thin film. *J Appl Phys* 1999, 86, 5311-5313.

209. Tan, X. G.; Yao, T.; Long, R.; Sun, Z. H.; Feng, Y. J.; Cheng, H.; Yuan, X.; Zhang, W. Q.; Liu, Q. H.; Wu, C. Z.; Xie, Y.; Wei, S. Q., Unraveling metal-insulator transition mechanism of vo2 triggered by tungsten doping. *Sci Rep-Uk* 2012, 2.

210. Hanlon, T. J.; Coath, J. A.; Richardson, M. A., Molybdenum-doped vanadium dioxide coatings on glass produced by the aqueous sol-gel method. *Thin Solid Films* 2003, 436, 269-272.

211.Xu, S. Q.; Ma, H. P.; Dai, S. X.; JIang, Z. H., Study on optical and electrical switching properties and phase transition mechanism of mo6+-doped vanadium dioxide thin films. *J Mater Sci* 2004, 39, 489-493.

212. Nishikawa, M.; Nakajima, T.; Kumagai, T.; Okutani, T.; Tsuchiya, T., Adjustment of thermal hysteresis in epitaxial vo2 films by doping metal ions. *J Ceram Soc Jpn* 2011, 119, 577-580.

213. Du, J.; Gao, Y. F.; Luo, H. J.; Kang, L. T.; Zhang, Z. T.; Chen, Z.; Cao, C. X., Significant changes in phase-transition hysteresis for ti-doped vo2 films prepared by polymer-assisted deposition. *Sol Energ Mat Sol C* 2011, 95, 469-475.

214. Chen, S.; Liu, J. J.; Wang, L. H.; Luo, H. J.; Gao, Y. F., Unraveling mechanism on reducing thermal hysteresis width of vo2 by ti doping: A joint experimental and theoretical study. *J Phys Chem C* 2014, 118, 18938-18944.

215. Burkhardt, W.; Christmann, T.; Franke, S.; Kriegseis, W.; Meister, D.; Meyer, B. K.; Niessner, W.; Schalch, D.; Scharmann, A., Tungsten and fluorine co-doping of vo2 films. *Thin Solid Films* 2002, 402, 226-231.

216. Fan, Z.; Jian, J.; Liu, Y.; Chen, Y.; Song, M.; Jiao, L.; Wang, H.; Zhang, X., In situ studies on superior thermal stability of bulk fezr nanocomposites. *Acta Mater* 2015,

101, 125-135.

217. Dannenberg, R.; Stach, E. A.; Groza, J. R.; Dresser, B. J., In-situ tem observations of abnormal grain growth, coarsening, and substrate de-wetting in nanocrystalline ag thin films. *Thin Solid Films* 2000, 370, 54-62.

218. Su, Q.; Jian, J.; Wang, H. Y.; Nastasi, M., Thermal stability of amorphous sioc/crystalline fe composite. *Philos Mag* 2015, 95, 3876-3887.

219. Dorcet, V.; Trolliard, G.; Boullay, P., Reinvestigation of phase transitions in na(0.5)bi(0.5)tio(3) by tem. Part i: First order rhombohedral to orthorhombic phase transition. *Chem Mater* 2008, 20, 5061-5073.

220. Legros, M.; Gianola, D. S.; Hemker, K. J., In situ tem observations of fast grain-boundary motion in stressed nanocrystalline aluminum films. *Acta Mater* 2008, 56, 3380-3393.

221. Lee, J. H.; Holland, T. B.; Mukherjee, A. K.; Zhang, X. H.; Wang, H. Y., Direct observation of lomer-cottrell locks during strain hardening in nanocrystalline nickel by in situ tem. *Sci Rep-Uk* 2013, 3.

222. Bufford, D.; Liu, Y.; Wang, J.; Wang, H.; Zhang, X., In situ nanoindentation study on plasticity and work hardening in aluminium with incoherent twin boundaries. *Nat Commun* 2014, 5.

223. Liu, Y.; Karaman, I.; Wang, H.; Zhang, X., Two types of martensitic phase transformations in magnetic shape memory alloys by in-situ nanoindentation studies. *Adv Mater* 2014, 26, 3893-3898.

224. Park, G. S.; Kim, Y. B.; Park, S. Y.; Li, X. S.; Heo, S.; Lee, M. J.; Chang, M.; Kwon, J. H.; Kim, M.; Chung, U. I.; Dittmann, R.; Waser, R.; Kim, K., In situ observation of filamentary conducting channels in an asymmetric ta2o5-x/tao2-x bilayer structure. *Nat Commun* 2013, 4.

225. Yang, Y.; Lee, K.; Zobel, M.; Mackovic, M.; Unruh, T.; Spiecker, E.; Schmuki, P., Formation of highly ordered vo2 nanotubular/nanoporous layers and their supercooling effect in phase transitions. *Adv Mater* 2012, 24, 1571-1575.

226. Sohn, J. I.; Joo, H. J.; Porter, A. E.; Choi, C. J.; Kim, K.; Kang, D. J.; Welland, M. E., Direct observation of the structural component of the metal-insulator phase transition and growth habits of epitaxially grown vo2 nanowires. *Nano Lett* 2007, 7, 1570-1574.

227. Sohn, J. I.; Joo, H. J.; Kim, K. S.; Yang, H. W.; Jang, A. R.; Ahn, D.; Lee, H. H.; Cha, S.; Kang, D. J.; Kim, J. M.; Welland, M. E., Stress-induced domain dynamics and

phase transitions in epitaxially grown vo2 nanowires. *Nanotechnology* 2012, 23.

228. Balakrishnan, V.; Ko, C.; Ramanathan, S., In situ studies on twinning and cracking proximal to insulator-metal transition in self-supported vo2/si3n4 membranes. *J Mater Res* 2012, 27, 1476-1481.

229. Viswanath, B.; Ramanathan, S., Direct in situ observation of structural transition driven actuation in vo2 utilizing electron transparent cantilevers. *Nanoscale* 2013, 5, 7484-7492.

230. Dijkkamp, D.; Venkatesan, T.; Wu, X. D.; Shaheen, S. A.; Jisrawi, N.; Minlee, Y. H.; Mclean, W. L.; Croft, M., Preparation of y-ba-cu oxide superconductor thin-films using pulsed laser evaporation from high-tc bulk material. *Appl Phys Lett* 1987, 51, 619-621.

231. Singh, R. K.; Narayan, J., Pulsed-laser evaporation technique for deposition of thin-films - physics and theoretical-model. *Phys Rev B* 1990, 41, 8843-8859.

232. Martin, L. W.; Chu, Y. H.; Ramesh, R., Advances in the growth and characterization of magnetic, ferroelectric, and multiferroic oxide thin films. *Mat Sci Eng R* 2010, 68, Iii-133.

233. Stokes, R. J.; Evans, D. F., *Fundamentals of interfacial engineering*. Wiley-VCH: New York, 1997; p xxviii, 701 p.

234. Cullity, B. D., *Elements of x-ray diffraction*. 2d ed.; Addison-Wesley Pub. Co.: Reading, Mass., 1978; p xii, 555 p.

235. Als-Nielsen, J.; McMorrow, D., *Elements of modern x-ray physics*. 2nd ed.; Wiley: Hoboken, 2011; p xii, 419 p.

236. Fultz, B.; Howe, J. M., *Transmission electron microscopy and diffractometry of materials*. 4th ed.; Springer: Heidelberg ; New York, 2013; p xx, 761 p.

237. Williams, D. B., *Practical analytical electron microscopy in materials science*. Verlag Chemie International ;

Electron Optics Pub. Co.: Weinheim, Basel

Deerfield Beach, Fla., 1984; p vii, 153 p.

238. Williams, D. B.; Carter, C. B., *Transmission electron microscopy : A textbook for materials science*. Plenum Press: New York, 1996; p xxvii, 729 p.

239. Williams, D. B.; Carter, C. B., *Transmission electron microscopy : A textbook for materials science*. 2nd ed.; Springer: New York, 2008.

240. Cui, Y. J.; Ramanathan, S., Substrate effects on metal-insulator transition characteristics of rf-sputtered epitaxial vo2 thin films. *J Vac Sci Technol A* 2011, 29.

241. Li, J.; Dho, J., Anomalous optical switching and thermal hysteresis behaviors of vo2 films on glass substrate. *Appl Phys Lett* 2011, 99.

242. Gupta, A.; Narayan, J.; Dutta, T., Near bulk semiconductor to metal transition in epitaxial vo2 thin films. *Appl Phys Lett* 2010, 97.

243. Molaei, R.; Bayati, M. R.; Narayan, J., Thin film epitaxy and near bulk semiconductor to metal transition in vo2/nio/ysz/si(001) heterostructures. *J Mater Res* 2012, 27, 3103-3109.

244. Mellan, T. A.; Grau-Crespo, R., Density functional theory study of rutile vo2 surfaces. *J Chem Phys* 2012, 137.

245. Stekolnikov, A. A.; Furthmuller, J.; Bechstedt, F., Absolute surface energies of group-iv semiconductors: Dependence on orientation and reconstruction. *Phys Rev B* 2002, 65.

246. Chen, A. P.; Bi, Z. X.; Zhang, W. R.; Jian, J.; Jia, Q. X.; Wang, H. Y., Textured metastable vo2 (b) thin films on srtio3 substrates with significantly enhanced conductivity. *Appl Phys Lett* 2014, 104.

247. Zhi, B.; Gao, G. Y.; Tan, X. L.; Chen, P. F.; Wang, L. F.; Jin, S. W.; Wu, W. B., Thickness-dependent metal-to-insulator transition in epitaxial vo2 films. *Mater Res Express* 2014, 1.

248. Yang, Z.; Ko, C.; Ramanathan, S., Metal-insulator transition characteristics of vo2 thin films grown on ge(100) single crystals. *J Appl Phys* 2010, 108.

249. Langford, J. I.; Wilson, A. J. C., Scherrer after 60 years - survey and some new results in determination of crystallite size. *J Appl Crystallogr* 1978, 11, 102-113.

250. van der Laan, D. C.; Haugan, T. J.; Barnes, P. N., Effect of a compressive uniaxial strain on the critical current density of grain boundaries in superconducting yba2cu3o7-delta films. *Phys Rev Lett* 2009, 103.

251. Ke, M.; Hackney, S. A.; Milligan, W. W.; Aifantis, E. C., Observation and measurement of grain rotation and plastic strain in nanostructured metal thin-films. *Nanostruct Mater* 1995, 5, 689-697.

252. Kim, B. J.; Lee, Y. W.; Chae, B. G.; Yun, S. J.; Oh, S. Y.; Kim, H. T.; Lim, Y. S., Temperature dependence of the first-order metal-insulator transition in vo2 and programmable critical temperature sensor. *Appl Phys Lett* 2007, 90.

253. Liu, X. X.; Wang, S. W.; Chen, F. L.; Yu, L. M.; Chen, X. S., Tuning phase transition temperature of vo2 thin films by annealing atmosphere. *J Phys D Appl Phys* 2015, 48.

254. Kats, M. A.; Sharma, D.; Lin, J.; Genevet, P.; Blanchard, R.; Yang, Z.; Qazilbash, M. M.; Basov, D. N.; Ramanathan, S.; Capasso, F., Ultra-thin perfect absorber employing a tunable phase change material. *Appl Phys Lett* 2012, 101.

255. Mai, L. Q.; Hu, B.; Hu, T.; Chen, W.; Gu, E. D., Electrical property of mo-doped vo2 nanowire array film by melting- quenching sol-gel method. *J Phys Chem B* 2006, 110, 19083-19086.

256. Soltani, M.; Chaker, M.; Haddad, E.; Kruzelecky, R. V.; Margot, J., Effects of ti-w codoping on the optical and electrical switching of vanadium dioxide thin films grown by a reactive pulsed laser deposition. *Appl Phys Lett* 2004, 85, 1958-1960.

257. Stoney, G. G., The tension of metallic films deposited by electrolysis. *P R Soc Lond a-Conta* 1909, 82, 172-175.

258. Lee, J. H.; Chou, C. Y.; Bi, Z. X.; Tsai, C. F.; Wang, H. Y., Growth-controlled surface roughness in al-doped zno as transparent conducting oxide. *Nanotechnology* 2009, 20.

259. Saha, R.; Nix, W. D., Effects of the substrate on the determination of thin film mechanical properties by nanoindentation. *Acta Mater* 2002, 50, 23-38.

260. Ivon, A. I.; Kolbunov, V. R.; Chernenko, I. M., Stability of electrical properties of vanadium dioxide based ceramics. *J Eur Ceram Soc* 1999, 19, 1883-1888.

261. Guzman, G.; Beteille, F.; Morineau, R.; Livage, J., Electrical switching in vo2 sol-gel films. *J Mater Chem* 1996, 6, 505-506.

262. Ko, C.; Ramanathan, S., Stability of electrical switching properties in vanadium dioxide thin films under multiple thermal cycles across the phase transition boundary. *J Appl Phys* 2008, 104.

263. Rao, K. V. K.; Naidu, S. V. N.; Iyengar, L., Thermal expansion of tetragonal phase of vo2. *J Phys Soc Jpn* 1967, 23, 1380-+.